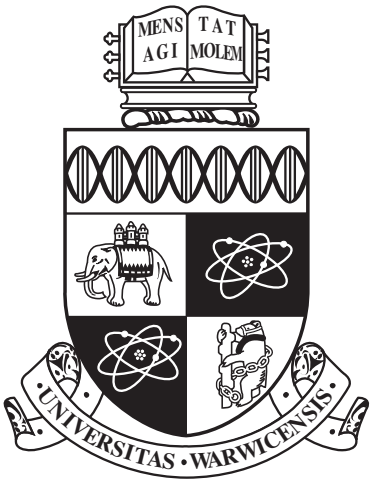

Development of Terahertz Signal Processing Methods for the Study of Human Skin

by

Xavier Emilio Ramirez Barker

Thesis

Submitted to the University of Warwick

for the degree of

Doctor of Philosophy in Physics

Department of Physics

March 2023

Contents

List of Figures

List of Tables

Acknowledgments

I would like to begin by expressing my gratitude to my supervisor, Professor Emma MacPherson, for her invaluable guidance and support throughout the course of this PhD. Furthermore, I would like to thank Dr Rayko Stantchev, Dr Arturo Hernandez and Dr Xuequan Chen for their research advice and aid with experimental equipment. The help provided by my supervisor and these post-docs from my research group were pivotal to my successful completion of this PhD.

I am deeply indebted to my family, friends, and members of my research group, who provided me with encouragement, support, and inspiration throughout the research process. Their willingness to listen and offer advice were instrumental in helping me to stay motivated and focused during the course of my PhD. A special appreciation goes towards Dr Qiushuo Sun and Dr Arturo Hernandez for their patient teaching when I first joined the research group. I thank Gonçalo Costa for his help with many of the measurements conducted for my studies. I also thank Peter Hepworth for the countless lunch breaks we shared together, sometimes being a much needed break from a long day. The many members of my badminton group have provided me with endless fun games and cherished moments, something I always look forward to. I appreciate my partner Tong Su for her company and the adventures we have together. I thank my parents for their unwavering support of me.

Finally, I would like to express my sincere appreciation to the study participants, without whom this research would not have been possible. Their willingness to share their time was essential for helping me to obtain the data necessary for the

studies I conducted. I would also like to thank Professor David Haddleton, Dr Gabit Nurumbetov and Medherant Ltd for providing the patches tested in Chapter 5. I thank Dr Rachel Hand for creating the hydrogels and Abbie Whittock for providing the crude extract, both used in Chapter 6.

Declarations

I hereby declare that this thesis is my original work and contains nothing that is the result of work done in collaboration with others, except as specified in the text and the acknowledgements. This work has not been submitted in full or in part to this or any other university for the award of another degree.

The material in some chapters has been published in the following papers and conference proceedings:

Chapter 3:

X. E. Ramirez Barker and E. Pickwell-MacPherson. *In vivo* THz Measurements of Human Skin: Investigating the Dependence on Ethnicity and Arm Dominance. *44th International Conference on Infrared, Millimeter and Terahertz Waves (IRMMW-THz).* IEEE, 2019.

X. E. Ramirez Barker, G. Costa, R. I. Stantchev *et al.* Monitoring the Terahertz Response of Skin Beneath Transdermal Drug Delivery Patches Using Sparse Deconvolution. *Transactions on Terahertz Science and Technology* (Accepted).

Chapter 4:

X. E. Ramirez Barker, R. I. Stanchev, A. I. Hernandez Serrano and E. Pickwell-

MacPherson. Simulated and Experimental Verification for a Terahertz Specific Finite Rate of Innovation Signal Processing Method. *Sensors*, 22(9):3387, 2022.

X. E. Ramirez Barker and E. Pickwell-MacPherson. Finite Rate of Innovation Theory Applied to Terahertz Signal Processing. *47th International Conference on Infrared, Millimeter and Terahertz Waves (IRMMW-THz)*. IEEE, 2022.

Chapter 5:

X. E. Ramirez Barker, G. Costa, R. I. Stantchev *et al.* Monitoring the Terahertz Response of Skin Beneath Transdermal Drug Delivery Patches Using Sparse Deconvolution. *Transactions on Terahertz Science and Technology* (Accepted).

Chapter 6:

A. L. Whittock, X. Ding, **X. E. Ramirez Barker** *et al.* Spectroscopic Insight on Impact of Environment on Natural Photoprotectants. *Chemical Science*, 24(14):6763-6769, 2023.

List of Publications

Peer Reviewed Journals:

1. T. Miao, **X. E. Ramirez Barker**, A. I. Hernandez Serrano *et al.* Evaluating the Ability of Hydrogel to Perform as Artificial Skin in the THz Range. (In preparation).

2. **X. E. Ramirez Barker**, G. Costa, R. I. Stantchev *et al.* Monitoring the Terahertz Response of Skin Beneath Transdermal Drug Delivery Patches Using Sparse Deconvolution. *Transactions on Terahertz Science and Technology* (Accepted).

3. A. L. Whittock, X. Ding, **X. E. Ramirez Barker** *et al.* Spectroscopic Insight on Impact of Environment on Natural Photoprotectants. *Chemical Science*, 24(14):6763-6769, 2023.

4. **X. E. Ramirez Barker**, R. I. Stanchev, A. I. Hernandez Serrano and E. Pickwell-MacPherson. Simulated and Experimental Verification for a Terahertz Specific Finite Rate of Innovation Signal Processing Method. *Sensors*, 22(9):3387, 2022.

Conference Presentations and Proceedings:

1. **X. E. Ramirez Barker** and E. Pickwell-MacPherson. Finite Rate of Innovation Theory Applied to Terahertz Signal Processing. *47th International Conference on Infrared, Millimeter and Terahertz Waves (IRMMW-THz)*. IEEE, 2022.

2. **X. E. Ramirez Barker** and E. Pickwell-MacPherson. Simple Experimental Verification for a Terahertz Finite Rate of Innovation Method. *9th International Conference on Optical Terahertz Science and Technology (OTST)*. 2022.

3. **X. E. Ramirez Barker** and E. Pickwell-MacPherson. Simulated Verification for a Finite Rate of Innovation Method Applied to Terahertz Signals. *46th International Conference on Infrared, Millimeter and Terahertz Waves (IRMMW-THz)*. IEEE, 2021.

4. **X. E. Ramirez Barker** and E. Pickwell-MacPherson. Sparse Deconvolution Applied to Terahertz Signals. *45th International Conference on Infrared, Millimeter and Terahertz Waves (IRMMW-THz)*. IEEE, 2020.

5. **X. E. Ramirez Barker** and E. Pickwell-MacPherson. Adapting Sparse Deconvolution for *in vivo* Skin Measurements. *TERANET UK-THz Symposium,* 2019.

6. **X. E. Ramirez Barker** and E. Pickwell-MacPherson. *In vivo* THz Measurements of Human Skin: Investigating the Dependence on Ethnicity and Arm Dominance. *44th International Conference on Infrared, Millimeter and Terahertz Waves (IRMMW-THz)*. IEEE, 2019.

Abstract

Terahertz (THz) light is an electromagnetic wave with frequencies between 0.1 and 10 THz, bounded by microwave and infrared light. There is increasing interest in THz for biomedical research, primarily due to its strong attenuation by water molecules and non-ionizing nature which enables the use of THz light for the study of *in vivo* human skin. Skin consists of a large proportion of water and the hydration level of skin can be linked to many diseases and injuries, thus THz measurements can extract useful information related to this.

In this thesis, different signal processing techniques are introduced and used for many *in vivo* skin studies. As the THz response of skin is easily impacted by many factors, an investigation into numerous such factors is conducted to aid in creating a measurement protocol. This measurement protocol will help to control variables which affect the skin during *in vivo* skin studies to ensure accurate results. Finite rate of innovation methods exploit signals with a finite number of degrees of freedom per unit time, such as THz pulsed signals. Such methods have not been applied to experimental THz measurements in published research before my work. The method is shown to produce accurate results at very low sampling rates for *in vivo* skin measurements and used to study an adhesive bandage applied to the volar forearm. This low sampling rate enables much quicker measurement times. In order to separate out overlapping reflections and extract more useful sample information, a sparse deconvolution method is introduced. I extend upon this method to include a reconstruction of individual sample reflections. This method is applied to investigate the effects of thin transdermal drug delivery patches on the skin. It is shown that this sparse method can accurately monitor the hydration level of the skin beneath these patches and links this to the type of patch applied. Studies on skin products applied to both real and artificial skin, in the form of hydrogel, are conducted in this thesis. This hydrogel is shown to effectively mimic real skin, and is used to investigate a promising product of crude algae extract which is currently in development and thus cannot be applied to real skin. Finally, a summary of the work performed in this thesis is given and areas of future work are identified.

Abbreviations

FFT Fast Fourier Transform

FRI Finite Rate of Innovation

IFFT Inverse Fast Fourier Transform

LTI Linear Time Invariant

MAA Mycosporine-like Amino Acids

NRC Normalised Relative Change

SNR Signal-to-Noise Ratio

SoS Sum-of-Sincs

TDD Transdermal Drug Delivery

THz Terahertz

THz-TDS Terahertz Time Domain Spectroscopy

UV Ultraviolet

Chapter 1

Introduction

1.1 THz Spectroscopy

1.1.1 THz Light

Terahertz (THz) light is a type of electromagnetic radiation, situated between the microwave and infrared portions as illustrated by Figure 1.1. The electromagnetic region corresponding to this THz band lies between the frequencies of 0.1 to 10 THz and wavelengths of 30 µm to 30 mm, and is often referred to as the "THz gap" due to the difficulty of generating and detecting radiation in this range. This difficulty is so pronounced that broadband THz generation and detection was not even possible until 1975, when David H. Auston developed the "Auston switch" [1]. As this gave accessibility to the "THz gap" the floodgates to THz research were opened, an area which has only seen increasing interest over time. As is typical with emerging technology, the required equipment is expensive but more affordable and compact THz systems have been developed and continue to be developed, allowing for more widespread applications for THz technology. Key features of THz radiation, such as its non-ionizing property and its penetration of many materials opaque to visible light and infrared, prove to be attractive for a wide range of applications. Examples of such applications include communication, security and defence, molecule struc-

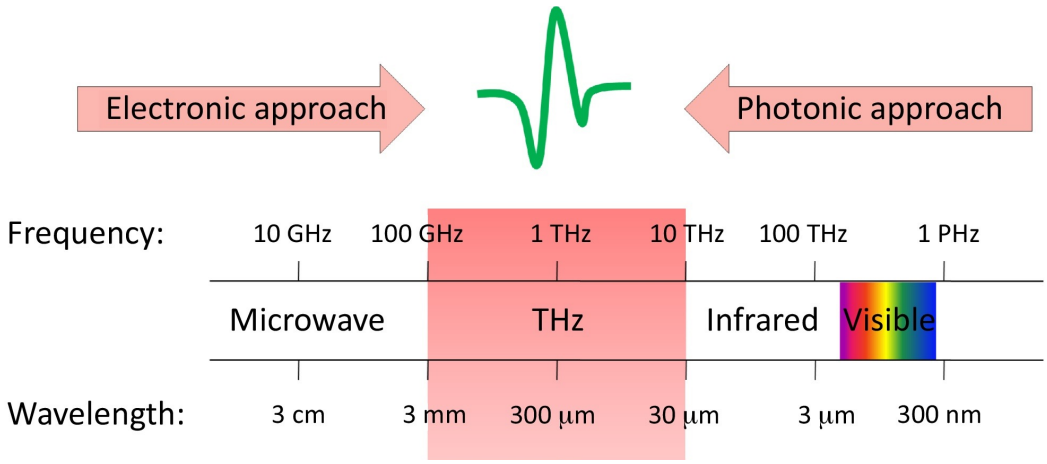

Figure 1.1: The location of the THz gap, situated between microwaves and infrared waves on the electromagnetic spectrum. Adapted from [3].

ture analysis, heritage assessment and metrology [2]. Furthermore, there is a great interest in THz biomedical applications by virtue of its sensitivity to water content in addition to its non-ionizing nature [3].

1.1.2 THz Time Domain Spectroscopy

Over the ten years following the development of the "Auston switch", David H. Auston went on to develop THz time domain spectroscopy (THz-TDS) where this work culminating with THz-TDS being employed to measure the dielectric response of a solid-state plasma in n-type germanium and a GaAs/GaAlAs superlattice [4]. This work demonstrated the great potential of THz-TDS by showing that it provides the capability of measuring precise shape changes of the THz pulse, which are associated with the dielectric properties of the material the laser was reflected from or transmitted through. Though this method measures the entire THz pulse in time domain, frequency information can be easily retrieved by performing a Fourier transform. One of the first significant applications for THz-TDS was to measure the nine strongest absorption cross sections of the water molecule over the frequency range of 0.2 to 1.45 THz at an accuracy level not previously achieved [5]. This high accuracy, along with the strong absorption of THz light by water in general, opened

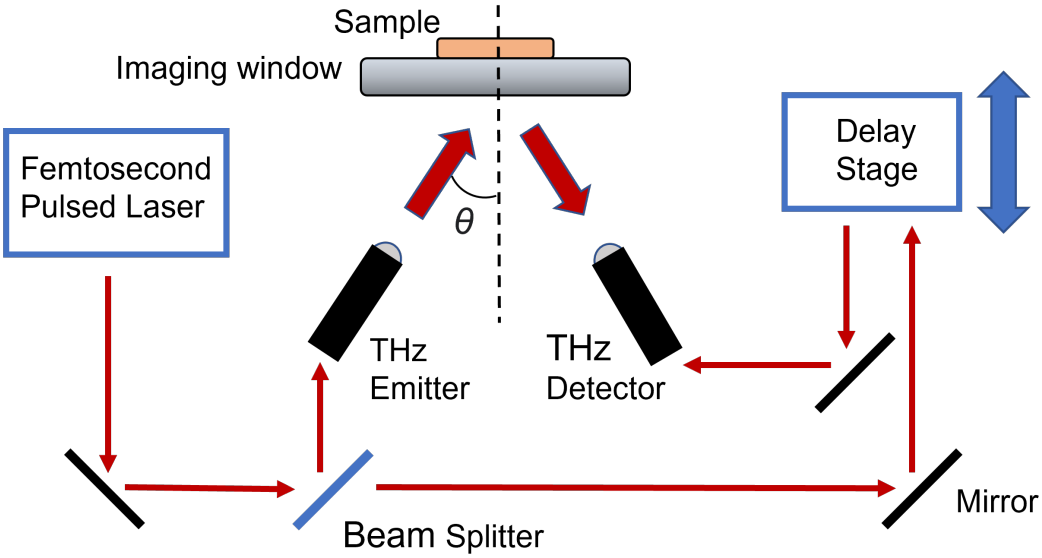

Figure 1.2: A schematic for THz-TDS in reflection geometry.

the doors to many avenues of research involving water molecules, including a wide spectrum of biomedical applications. Furthermore, since this research in 1989 THz-TDS systems have been refined and made commercially available, allowing for a less expensive and easier operating entry into interdisciplinary research using these systems.

Figure 1.2 contains the schematic of a typical THz-TDS system in reflection geometry. The key components for this setup consist of a femtosecond pulsed laser, a delay stage and both a photoconductive emitter and detector [6]. Details on the photoconductive antennas will be given in the following section, with the THz-TDS system explanation as a whole following here. The femtosecond pulsed laser is generated and then directed into a beam splitter, which sends one half of the laser to the photoconductive THz emitter and the other half is destined for the photoconductive THz detector. Crucially, before it reaches the detector, it is directed through a mechanical delay stage which consists of a series of mirrors designed to introduce and control a time delay between the arrival of the THz pulse which has been emitted and then reflected off the sample with the arrival of the femtosecond laser pulse at

the THz detector. By doing this, it is now possible to sample the received THz pulse across a chosen time domain window, which could consist of multiple THz reflections. For reflection geometry, an important challenge is to ensure alignment of the THz beam path and sample. To help with this an imaging window is positioned such that the sample placed atop of it will be in alignment for the chosen angle of incidence θ. Quartz is often chosen as the imaging window material as it has minimum absorption in the THz frequency range [7]. A further point to note is that the femtosecond section of THz-TDS is often in a closed system, helping with safety concerns as all laser safety issues are associated with the femtosecond laser, as THz beams are completely safe to humans. In addition to the free space system outline in Figure 1.2, optical fibers can be used for transmitting the optical laser beams in fiber based systems, such as those used for the work contained within this thesis.

1.1.3 THz Generation and Detection

A common approach for generating and detecting THz light, and the one used for measurements presented in this thesis, utilize photoconductive antennas [8]. The mechanism for using one of these antennas for generating THz light is shown in Figure 1.3. Here, a femtosecond laser pulse is targeted at the photoconductive antenna to excite short lifetime carriers within the semiconductor substrate. As a DC bias is applied across the antenna, the excited carriers are accelerated and produce an electric field proportional to the rate of acceleration of this photocurrent. With the resulting pulse of electromagnetic radiation having a temporal width of the order of 1 ps, a THz pulse is generated.

A remarkably similar mechanism for detecting THz light is shown in Figure 1.4. As opposed to a bias voltage being applied across the antenna to drive a current for THz generation, it is a received THz pulse inducing a current in the excited carriers for THz detection. In both cases, it is still the femtosecond laser

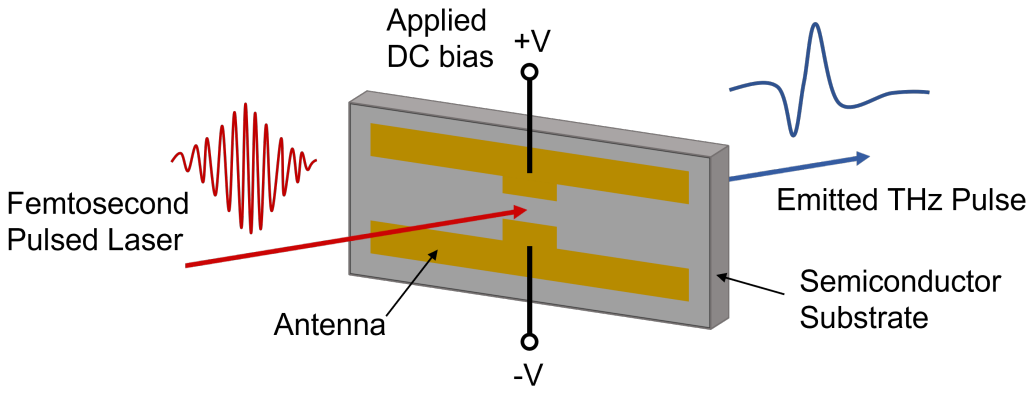

Figure 1.3: A photoconductive antenna being used to generate a THz pulse from a femtosecond laser.

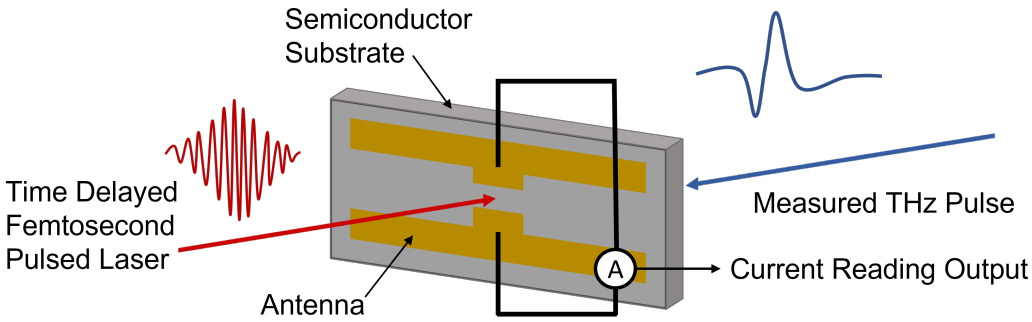

Figure 1.4: A photoconductive antenna being used to detect a THz pulse using a time delayed femtosecond pulsed laser as a probe.

producing the excited carriers. A stronger received THz pulse leads to a higher induced current, thus the current can be measured and processed to deduce the THz field strength. However, the femtosecond probing pulse can only detect the current induced by the instantaneous THz field, thus the optical delay stage, described in the previous section, is necessary to change the arrival time of the probing pulse in order to sample over the whole THz pulse being measured.

1.1.4 Applications of THz

A wide range of applications across various fields have been developed since the "THz gap" was bridged, with many of the most significant results being highlighted in this

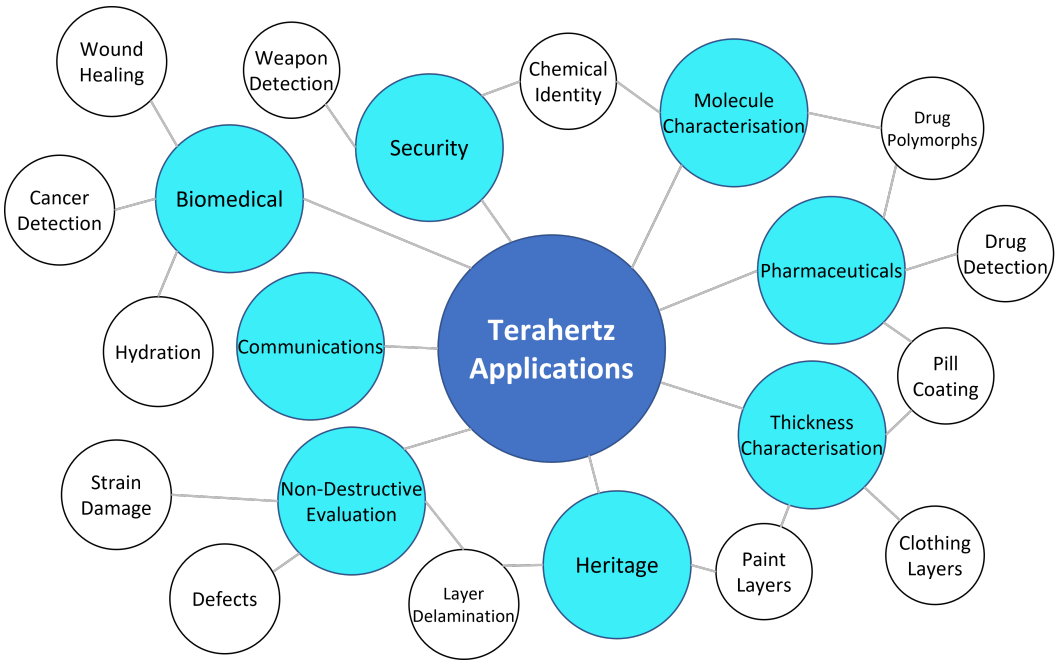

Figure 1.5: A summary of some THz applications currently being researched.

section and shown in Figure 1.5. As the key focus of this thesis is on biomedical applications for THz, these will be detailed in the following section along with the appropriate background information. There are a variety of properties which make THz such an attractive avenue of research:

- THz spectroscopy and imaging techniques are able to extract both time domain and frequency information from samples.
- The non-destructive nature of THz light by being non-ionizing, having low photon energies in general and effective use at very low power levels.
- The delicacy in which THz can be used with non-contact modalities avoiding any risk to fragile samples a contact method would result in.
- The penetrative capability in broad classes of nonmetallic materials and nonpolar molecules.
- The extremely short femtosecond pulses providing higher resolution compared

to many competing imaging methods.

- Many chemicals of interest have characteristic signatures in the THz range due to molecule-specific motions, key to some security applications.

- A strong attenuation by water molecules, resulting in a contrast between healthy and diseased or damaged tissues.

THz imaging has been explored as a technique for security scanning [9–11], as it is non-ionizing for the screening of people and able to detect hidden objects through clothes and common packing materials. These hidden objects detected include metal and non-metallic weapons, such as ceramic, plastic or composite guns and knifes. Furthermore, the characteristic THz spectra of certain hidden substances such as plastic explosives and other chemical and biological agents could be used to detect them using THz scanning.

A further use of characteristic THz spectra is found in pharmaceutical research, where THz spectroscopy can be employed to identify different drugs, differentiate between polymorphs [12] and distinguish between anhydrous and hydrated drug forms [13]. It is of great importance to distinguish between different forms of drugs, as they can have different physiochemical properties and thus can lead to unwanted side effects without appropriate measures of product quality control. Another aspect of quality control in pharmaceutics is monitoring the coating thickness of drug tablets, to ensure the intended dosage results and that no leakage of the drug contained within the coating occurs. THz imaging methods have met with success for this coating thickness quality control [14, 15].

Other areas can also benefit from THz techniques for thickness measurements. For example, they have been employed to inspect the thickness and quality of paint layers on cars whilst having the benefits of a non-contact modality and better spatial resolution for two-dimensional mapping as compared to conventional methods [16]. Furthermore, successful results have been found with composition

and thickness measurements of paper [17] and waterproof layer quality control of textiles [18].

Moreover, investigating the thicknesses of paint layers in historical artworks using THz can be enlightening, with the key benefit of being non-destructive. By observing the number, thicknesses and constituents of the layers the painting techniques used by the artist and previous conservation efforts were determined by Dong *et al.* [19]. On the topic of heritage, there has been much research into the use of THz for art conservation and tracking the chronological evolution of pieces [20–23].

Metamaterials are capable of enhancing the interaction of THz radiation with a sample, resulting in a higher sensitivity to the spectral features of the sample and allowing for a smaller quantity of material to be present and still identified. As such, progress in this field would aid all studies into spectral identification using THz spectroscopy. Fortunately, there is significant research into this area, covered in the literature review by Xu *et al.* [24].

THz measurements have been used in a wide range of non-destructive testing applications throughout industry, detecting surface defects such as localised burn damage and puncture holes in addition to hidden sub-surface defects such as matrix cracking and delamination [25–27]. These results are often verified by a comparison to standard industry techniques, but often come with additional benefits such as the non-ionizing nature being safer for the user and better spatial resolution as compared to X-ray techniques, for example.

Finally, communications is a lucrative research avenue as it would unlock faster rates of data transfer given its high frequency and large bandwidth. To promote the application of THz communication, the development of THz devices including modulators, waveguides and polarization converters [28,29] would need to be pushed forward.

1.2 THz in Biomedical Research

1.2.1 Advantages of THz for Biomedical Research

The key features of THz light which make it so attractive for biomedical research are its high sensitivity to water content and its non-ionizing nature. Water, a polar molecule, has a particularly high THz absorption coefficient of 220 cm^{-1} at 1 THz for room temperature, exceeding that of common biomolecules [30]. The dominant cause of this high absorption in water is the intermolecular interactions due to the permanent and induced dipole moments in the hydrogen bonds present in the network of water molecules [31]. This results in THz having a high sensitivity to water content, enabling THz technology to be employed for differentiating tissues or biological matter of varying hydration levels to an accurate degree. Water content levels are crucial to many processes and functions in organisms or biological systems, thus a tool to assess this accurately is highly desirable. For example, normal tissues and cancer tissues have different water content and the living state of bacteria can be distinguished by their different hydration levels.

There are other widely used methods for studying human skin hydration, such as corneometer measurements and transepidermal water loss evaluation. The capacitance of the skin surface can be measured using a corneometer, which can be used to infer the relative hydration due to its calibration using water [32]. Transepidermal water loss is estimated by measuring the rate of evaporation of water from the surface of the skin [33]. Compared to these methods, THz carries the additional benefits of more directly measuring water content, providing much more information in general and has been shown to perform better when different samples are applied to skin [34].

The low-energy photons of THz light (on the order of 1-10 meV) ensures that it is non-ionizing and thus safe to be used on living subjects, whilst providing a noninvasive imaging modality. This provides THz measurements with a significant

advantage over other ionizing methods, such as X-rays. However, the relatively new nature of the THz research field stipulates the need for investigation into the effects of THz light on biological tissues. Hough *et al.* investigated the biological effects of low to intense THz pulses on gene expressions, finding no significant modifications to the gene expression with low power THz light [35]. Angeluts *et al.* studied blood leukocytes irradiated by THz light and found no DNA damage using the comet assay [36]. A full review of the biological effects of tissues and cells at exposure to THz radiation has been compiled by Cherkasova *et al.* [37]. All research contained within this thesis used photoconductive antennas to produce the THz light, which ensures the use of low power THz far below the thresholds which have been identified for potential damage to biological tissues.

1.2.2 THz Imaging of Skin

Skin is the outer covering of the human body and its largest organ, constituting 15-20% of its total mass. One of the vital functions skin provides is as a semi-permeable barrier between the body and its external environment, protecting it from factors such as bacteria, harmful chemicals and adverse temperature. Furthermore, it manufactures vitamin D, helps to maintain the hydration level in the body and contains many nerves so it can act as a huge sensor. Due to the importance of skin, research into it and methods to monitor and diagnose issues with it are very significant. One of the largest and most variable constituents of skin is water, as such THz sensitivity to water content is a great strength here [38]. The structure of skin is divided into three primary layers, going from the outermost to innermost layers: epidermis, dermis and hypodermis [39]. The epidermis is split further into two sub-layers, the stratum corneum and the viable epidermis. The stratum corneum is the dead outermost layer of skin, the thickness of which varies greatly across the body.

As THz is so greatly attenuated by water molecules, reflection geometry is necessary for almost all measurements of skin, with thinly sliced excised skin

samples being an exception. Furthermore, even in reflection geometry THz light only has a small penetration depth into skin, resulting in just the epidermis being measured in most cases. Cole *et al.* have used THz imaging and spectroscopy *in vivo* (where a whole, living human is examined) to search for the interface between the stratum corneum and the viable epidermis within the epidermis layer [40]. Here, they were able to measure a second reflection associated with the stratum corneum-viable epidermis boundary in the palm but could not detect this second reflection in other locations of the body such as the wrist and forearm as the stratum corneum is too thin in these areas. In addition to time domain data, THz spectroscopy has been employed to measure the optical properties of *in vivo* skin at different locations, such as the refractive index and absorption coefficient information [41]. Further to extracting information for the outermost part of skin, various structural models can be employed to estimate information for deeper into the skin. For example, Raman spectroscopy has shown that the epidermis has a relatively constant water concentration value, whilst the stratum corneum has a depth-dependent water concentration gradient [42]. Using this result, many detailed models have been developed to estimate water concentration as a function of depth into the skin, using information gained from initial THz measurements of the skin's surface [43].

Ethical considerations are necessary for THz *in vivo* measurements. As explained previously, THz light is non-ionizing and, for the systems used in this thesis, of low power which is safely below any potential damage thresholds. This, along with all other relevant information pertaining to the study, must be fully explained to any potential subjects, so their written informed consent to take part in the study can be obtained. Additionally, efforts into the handling and anonymity of the data measured and subject information recorded should be made to ensure the privacy of the subjects. These efforts were made for all *in vivo* measurements conducted for this thesis. Specifically, ethical approval was obtained for the studies conducted in this thesis from the Biomedical Scientific Research Ethics Committee, BSREC,

(REGO-2018-2273 AM03).

1.2.3 Skin Phantoms and Artificial Skin for THz Frequencies

Imaging phantoms are specially designed objects which resemble human tissue for evaluating, analyzing and calibrating the medical device in question. These procedures need stable materials with accurately controlled properties, which real biological matter does not provide as their conditions change over time and can vary significantly between samples. Therefore, phantoms accurately substituting real biological objects are of great interest. For THz devices, phantoms mimicking breast tissue were designed and their potential application to quantifying breast tissue pathology was confirmed [44]. Additionally, gelatin phantoms were used for quantitative assessments of a THz hydration imagery method designed for early detection of corneal pathologies [45].

Furthermore, such phantoms can be used as artificial skin if designed appropriately for the THz response of skin. This carries the additional benefit of enabling research into skin whilst avoiding the need, and risk to, animal or human subjects. For example, hydrogel skin phantoms were used by Jayasankar *et al.* to investigate the fast and reliable testing of pharmaceutical and cosmetic products [46]. Such products require thorough safety testing before approval is given for their application to human subjects, therefore methods to research the effects of such products without applying them to human subjects is in high demand. Corridon *et al.* created complex skin samples of different and controllable hydration levels from collagen, silicone and other materials [47]. The THz optical properties of these samples were compared to the THz optical properties of freshly excised skin samples to ascertain their efficacy as artificial skin. A preliminary investigation by Zhang *et al.* uses artificial skin with and without metastatic melanomas to compare their refractive indices and absorption coefficients with the aim of helping techniques for diagnosing and preventing tumours at an early stage [48].

1.2.4 THz Imaging for Cancer Diagnosis

As cancer accounts for nearly one in six deaths, research into cancer diagnosis and treatment is one of the most important fields in medicine. As such, there has been much research into using THz light with the objective of detecting cancer by using it to distinguish between healthy and cancerous tissues. One approach to this is conducting *ex vivo* studies, where tissues are extracted from the body and examined. Advantages of this method include the ability to thinly slice samples, allowing for the use of THz transmission measurements in addition to reflection measurements, and to investigate the effects of inducing changes to the sample such as burning of the tissue, which obviously could not be done with a living subject. A significant drawback to *ex vivo* methods is the degradation of the sample, meaning that studies will have to use either fresh samples or make use of some preservation method which has minimal effect on the sample, such as by freezing or formalin fixing.

Though preservation methods can interfere with the THz response of the tissue, they usually work in part by dehydrating or freezing the liquid water in the sample which has the byproducts of improving the penetration depth of THz light into the tissue and increasing the contrast between structurally differing regions of the sample. Wahaia *et al.* studied dehydrated colon tissues using a THz imaging system to find a contrast between neoplastic and control tissues, which was corroborated by histological findings in the same tissues [49]. By investigating frozen oral tissue samples, Sim *et al.* were able to show that THz can be used to detect cancerous tumours hidden inside tissue and that freezing the sample improves the contrast between cancerous and healthy tissue [50]. Fitzgerald *et al.* demonstrated that THz imaging could be used to successfully map breast tumour regions in excised tissue, which had moderate correlation with the results obtained from routine histological tests [51].

Looking at fresh *ex vivo* studies, there is no longer the additional problem of how the preservation technique affects the samples, though the penetration depth

tends to be smaller due to a higher water content in the fresh tissue. Therefore, much of the research using fresh *ex vivo* samples focuses on reflection measurements. A blind study to identify basal cell carcinoma, the most common form of skin cancer, was conducted by Woodward *et al.* using fresh samples [52]. In this study, THz imaging was shown to be an effective tool for detecting this cancer, with the results being verified by histology. A further example of using fresh tissue *ex vivo* is a study by Sim *et al.* where oral malignant melanoma was imaged using 2-D and B-scan THz imaging techniques, the results of which were verified by histological findings as standard [53].

Another approach to using THz imaging for cancer diagnosis and treatment is conducting *in vivo* studies, which fully exploit the non-ionizing advantage of this imaging method. Moreover, *in vivo* measurements present the opportunity for non-invasive clinical investigations, without the need to excise a sample of tissue for *ex vivo* analysis and thus avoiding any risks associated with that surgery and potentially providing quicker results to patients. Studies using *in vivo* measurements also open the doors to research into the response of living tissue to treatments or the efficacy of treatments, such as checking for any remaining cancerous tissue after surgery to remove it. However, as previously discussed, THz light is strongly absorbed by water and therefore only reflection measurements of surface level tissues such as skin and the eye are available. Another factor for consideration is the extra difficulty measurements using live subjects brings, as they introduce many more variables which need to be controlled or accounted for. To introduce a number of them: maintaining constant and consistent contact between the region of the subject being measured and the imaging window, the recent skin treatments or washing of the subject's skin and the room's temperature and humidity which is being used for taking the measurements. These will be discussed in detail within Chapter 3.

Zaytsev *et al.* used *in vivo* THz spectroscopy to differentiate between dysplastic and non-dysplastic skin moles using the contrast in their THz dielectric per-

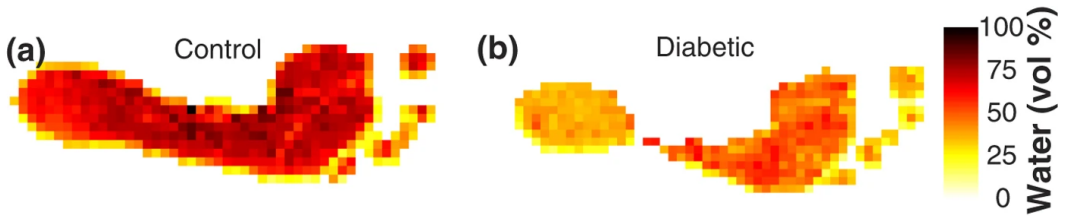

Figure 1.6: The volumetric fraction of water in the foot calculated from THz measurements for a) a typical member of the control group and b) a typical member of the diabetic group. Included with permission of the authors [50].

mittivity [54]. As dysplastic moles are a precursor of melanoma, a dangerous form of skin cancer, non-invasive early diagnosis is of great importance. With the goal of researching an *in vivo* THz method for helping facilitate delineation of tumour margins before basal cell carcinoma surgery, Wallace *et al.* demonstrated that through a broadening of the reflected THz pulse they could identify regions of disease which correlated well with histology [55].

1.2.5 Other THz Biomedical Applications

There are many other potential avenues for biomedical applications using THz light that are currently being researched, in addition to cancer diagnosis. Many of these take advantage of the benefits of using THz imaging to study skin and other tissues, such as changes to water content and structure leading to differences in the THz optical properties of the sample which was often exploited by the studies described in the previous section. For example, Hernandez-Cardoso *et al.* proposed a THz screening method for early detection of diabetic foot syndrome, for which there is no current objective method for doing so [56]. As presented in Figure 1.6, they were able to differentiate between healthy, control feet and feet from people inside their diabetic group by calculating the volumetric fraction of water from their *in vivo* THz measurements.

Taylor *et al.* used porcine (pig) skin samples to investigate if THz could be used to detect, and judge the extent of, second-degree burns [57]. They were

able to discern if the skin was burnt even through ten layers of dry medical gauze and found a "halo" effect surrounding the burnt areas which may correlate to the extent of the burn injury. Further to using THz to detect burn injuries, Wang *et al.* explored the effects of silicone gel sheeting to the skin *in vivo*, which is a common treatment for severe burns [58]. One of their key findings was that THz could be used to monitor how hydrated the treatment had made the skin, once the silicone sheeting was removed. Looking at injury healing in general, Fan *et al.* studied the healing process of scars and their contrast to healthy tissue [59]. They discovered that this contrast in the absorption coefficient becomes less prominent after a few months post-injury, but that it was still significant and easily detectable even when the scar was difficult to see with the naked eye.

THz has also been successfully applied to monitoring the effects of various drugs applied to the skin. Kim *et al.* used excised mouse skin to explore the real-time tracing of drugs within the skin using THz, finding that it could be used for monitoring the spatial distribution and penetration of the drug into the skin at the drug-applied sites [60]. Moreover, in a further study they found that their THz imaging technique could be used to track the distribution of topically applied drugs for *in vivo* mouse measurements [61]. In another example of drug related research for skin, Wang *et al.* used THz imaging to perform a study on fresh porcine skin samples to compare the efficacy of different drug penetration enhancement techniques [62]. In related research, Ramos-Soto *et al.* used excised porcine skin to test the occlusive, hyperosmotic and moisturising behaviour of common moisturiser ingredients [63].

In an additional THz application not centred on skin, Taylor *et al.* have been developing a system for *in vivo* measurements of the human cornea. They took the first ever THz images of *in vivo* cornea using rabbits, assessing the corneal water content and how this changed following dehydration by a gentle stream of air [64]. They then went on to develop their novel imaging system and introduced an image reconstruction method specifically for human cornea or other similarly

near spherical targets [65]. By using these methods on corneal phantoms and *ex vivo* human corneas they demonstrated the hydration sensitivity and reliability of their process. Furthermore, they present successful non-contact THz images for *in vivo* human cornea.

A further broad biomedical application of THz is the study of solutes in water. The dynamics of water surrounding a solute are vital in the behaviour of many biological systems, such as in the function of proteins and carbohydrates [66]. Due to the high sensitivity THz has to the hydrogen-bond dynamics in water-solute systems, THz spectroscopy can be used as an effective tool for providing direct insights into such systems. For example, Sun *et al.* used THz spectroscopy to investigate glycine in water to obtain a clear picture of the individual contributions of molecular motion in terms of distinct vibrational modes and specific couplings between water and glycine molecules [67].

1.3 Thesis Overview

In this thesis, a series of studies using THz imaging and various signal processing methods are presented, with a specific focus on biomedical applications relating to the skin. In Chapter 2, the fundamental electromagnetic wave theory used in this thesis is introduced. Furthermore, standard approaches for processing THz measurements are described, as are the THz-TDS systems used for collecting the data presented in this thesis. Many variables which affect the THz response of *in vivo* skin measurements are investigated in Chapter 3, such as pressure and occlusion. These results are used to help construct the measurement protocol presented, designed to control these variables to obtain more accurate and precise results for *in vivo* studies. Chapter 4 introduces a THz finite rate of innovation method, which successfully produces accurate results in various simulated and experimental studies, crucially all at very low sampling rates. A THz sparse deconvolution and reconstruc-

tion method is used to monitor the effect of transdermal drug deliver patches on skin in Chapter 5. The hydrating effect of patches with different backing materials and excipient levels is investigated in a 2-hour and 24-hour study, with the sparse method effectively monitoring the water level of skin beneath the patches. Chapter 6 contains an investigation of THz-TDS being used in skin product testing and the effectiveness of hydrogel as artificial skin. Finally, Chapter 7 is a summary of the work presented in this thesis and identifies potential areas for further research to be conducted upon.

Chapter 2

THz Theory and Experimental Setups

2.1 Introduction

Fundamental explanations of standard THz theory, processing methods and setups are necessary to appreciate how work contained within this thesis employs and builds upon them. Section 2.2 describes how waves propagate through materials and react to interfaces. Section 2.3 covers standard THz processing methods to extract optical parameters from both transmission and reflection geometries. These processing methods will be heavily built upon in Chapters 4 and 5. Lastly, Section 2.4 outlines the experimental setups used to perform the measurements taken for work within this thesis.

2.2 THz Wave Propagation

2.2.1 Wave Equations

As with all electromagnetic fields, the behaviour of THz radiation is described by Maxwell's equations. For a homogeneous, isotropic medium and in the absence of

charges or currents, these equations can be expressed by:

$$\nabla \cdot \boldsymbol{E} = 0 \tag{2.1}$$

$$\nabla \times \boldsymbol{E} = -\frac{\partial \boldsymbol{B}}{\partial t} \tag{2.2}$$

$$\nabla \cdot \boldsymbol{B} = 0 \tag{2.3}$$

$$\nabla \times \boldsymbol{B} = \mu\epsilon\frac{\partial \boldsymbol{E}}{\partial t}, \tag{2.4}$$

where $\boldsymbol{E}$ and $\boldsymbol{B}$ are the electric and magnetic fields respectively and μ and ϵ are the permeability and permittivity of the medium respectively. It is possible to derive the wave equation, which describes the propagation of waves in a medium, for electric fields by first taking the curl of Equation 2.2:

$$\nabla \times (\nabla \times \boldsymbol{E}) = -\frac{\partial}{\partial t}(\nabla \times B). \tag{2.5}$$

Substituting Equation 2.4 into Equation 2.5 and employing the vector identity: $\nabla \times (\nabla \times \boldsymbol{A}) = \nabla(\nabla \cdot \boldsymbol{A}) - \nabla^2 \boldsymbol{A}$ the wave equation for an electric field propagating in a medium results:

$$\nabla^2 \boldsymbol{E} = \mu\epsilon\frac{\partial^2 \boldsymbol{E}}{\partial t^2}. \tag{2.6}$$

From Equation 2.6 it is possible to deduce the propagation speed in a medium: $v = \frac{1}{\sqrt{\mu\epsilon}}$, which in the case of a vacuum gives the speed of light: $c = \frac{1}{\sqrt{\mu_0\epsilon_0}}$ where the constants μ_0 and ϵ_0 are the permeability and permittivity of free space respectively. The speed of light is the fastest propagation speed possible, with other mediums reducing this speed by different amounts. The ratio between the speed of light and the propagation speed in a given medium is introduced as the refractive index: $n = \frac{c}{v}$. For a wave travelling in the x direction, a solution to the wave equation is given by:

$$E(x,t) = E_0 e^{i(\omega t - kx)}, \tag{2.7}$$

where t is the time, E_0 is the amplitude of the wave, ω is the angular frequency and k is the wavenumber given by:

$$k = \frac{\tilde{n}\omega}{c}. \tag{2.8}$$

Here, the complex refractive index has been introduced, $\tilde{n}$, which is defined by:

$$\tilde{n} = n - i\kappa, \tag{2.9}$$

where κ is the extinction coefficient. The complex refractive index is a very useful parameter for characterising properties of media, with another being the absorption coefficient, α, defined by:

$$\alpha = \frac{2\omega\kappa}{c}. \tag{2.10}$$

The absorption coefficient describes how waves are attenuated with propagation distance and frequency, with the penetration depth given by: $\varrho = \frac{1}{\alpha}$. Bearing in mind these key definitions given by Equations 2.9 and 2.10, Equation 2.7 can be rewritten into the following:

$$E(x,t) = E_0 e^{-\frac{\alpha x}{2}} e^{i(\omega t - \frac{\omega n x}{c})}. \tag{2.11}$$

Key observations to note here are that n will change the phase of the wave and that the penetration depth informs us of the distance the wave would travel before the amplitude decreases to $e^{-0.5}$ or for the intensity to reduce to e^{-1}.

2.2.2 Waves at Interfaces

Systems where THz waves simply travel through one medium only are not of interest for the work contained in this thesis, so THz wave propagation at an interface will be introduced. Snell's law is an fundamental tool for describing how waves react to

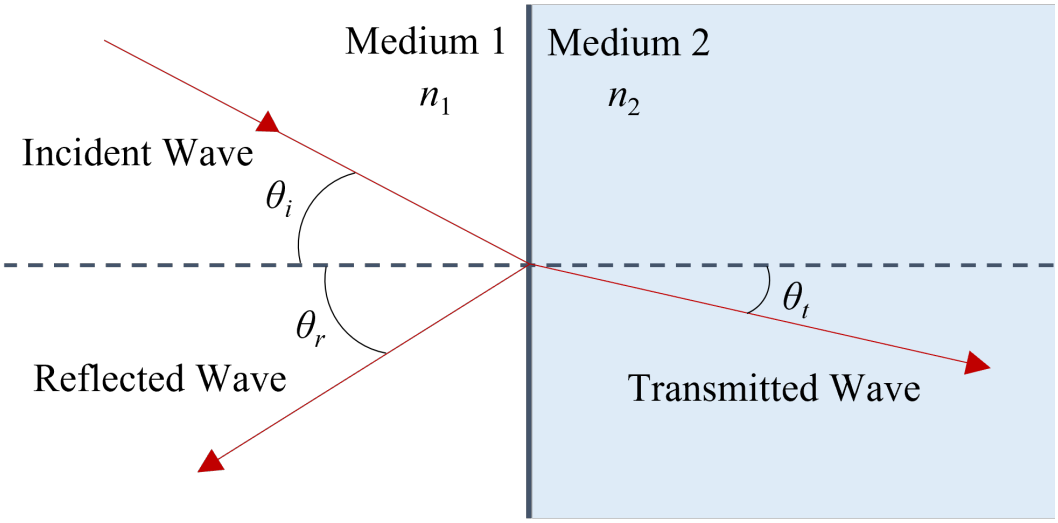

Figure 2.1: The behaviour of an incident wave travelling in a medium of refractive index n_1 at the interface of a different medium of refractive index n_2, resulting in a reflected and transmitted wave.

interfaces, and is defined by:

$$n_1 \sin\theta_i = n_2 \sin\theta_t, \tag{2.12}$$

where n_1 is the refractive index of the first medium the incident wave of angle θ_i is travelling through and n_2 is the refractive index of the second medium the transmitted wave of angle θ_t is travelling through. This relationship is demonstrated in Figure 2.1, with it also showing that an additional wave is reflected at the interface which abides by the constraint of:

$$\theta_r = \theta_i. \tag{2.13}$$

For THz-TDS, it is also of great importance to quantify how the different components of a light wave are transmitted and reflected at an interface in addition to any phase transitions that may occur, which are covered by the Fresnel equations. These equations come in two sets, depending on the polarization state of the incident wave, which is either s- or p-polarized as illustrated in Figure 2.2. P-polarized light

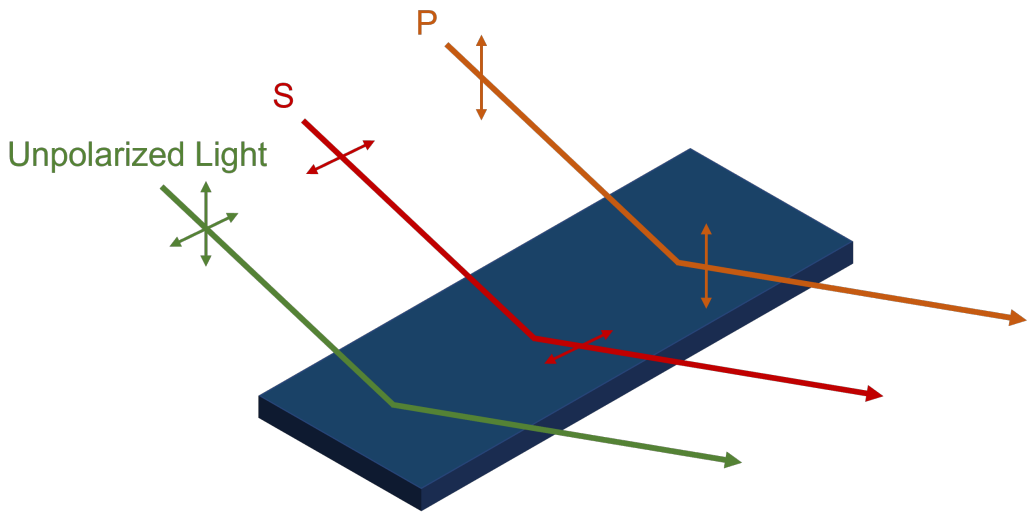

Figure 2.2: An illustration to demonstrate s-polarized light, which is perpendicular to the plane of incidence, and p-polarized light, which is parallel to the plane of incidence.

has polarization direction lying in the plane of incidence, that being the plane in which the light travels and that contains the surface normal. Whereas, s-polarized light has polarization direction lying perpendicular to the place of incidence. The Fresnel reflection coefficients for s-polarized light, r_s, and p-polarised light, r_p, are given by the ratio of the reflected electric field, E_r, to the incident electric field, E_i, as shown below:

$$\frac{E_{rs}}{E_{is}} = r_s = \frac{\tilde{n}_i \cos\theta_i - \tilde{n}_t \cos\theta_t}{\tilde{n}_i \cos\theta_i + \tilde{n}_t \cos\theta_t} \tag{2.14}$$

$$\frac{E_{rp}}{E_{ip}} = r_p = \frac{\tilde{n}_t \cos\theta_i - \tilde{n}_i \cos\theta_t}{\tilde{n}_t \cos\theta_i + \tilde{n}_i \cos\theta_t}. \tag{2.15}$$

The transmission coefficients for s-polarized light, t_s, and p-polarised light, t_p, are given by the ratio of the transmitted electric field, E_t, to the incident electric field, E_i, as seen here:

$$\frac{E_{ts}}{E_{is}} = t_s = \frac{2\tilde{n}_i \cos\theta_i}{\tilde{n}_i \cos\theta_i + \tilde{n}_t \cos\theta_t} \tag{2.16}$$

$$\frac{E_{tp}}{E_{ip}} = t_p = \frac{2\tilde{n}_i \cos\theta_i}{\tilde{n}_t \cos\theta_i + \tilde{n}_i \cos\theta_t}. \tag{2.17}$$

Experimentally, in THz-TDS it is simple to set up equipment to choose and measure

an incident angle. However, it is much more challenging to measure the transmission angle. Thus, it is beneficial to eliminate θ_t by using Snell's law as introduced in Equation 2.12. For example, Equation 2.14 can be rewritten in the form of:

$$r_s = \frac{\tilde{n}_i \cos\theta_i - \sqrt{\tilde{n}_t^2 - \tilde{n}_i^2 \sin\theta_i}}{\tilde{n}_i \cos\theta_i + \sqrt{\tilde{n}_t^2 - \tilde{n}_i^2 \sin\theta_i}}. \tag{2.18}$$

2.3 Processing THz Measurements

2.3.1 Transmission Geometry

THz-TDS measurements in transmission geometry excel at sample characterization as it is highly accurate and easy to implement with a simple reference procedure, especially in the case of a thick enough sample where multiple reflections can be separated whilst THz light can still penetrate through it sufficiently. As THz-TDS provides both the amplitude and phase data, frequency information for the sample can be obtained, such as the refractive index and absorption coefficient. This is done by taking the ratio of the measured sample signal, E_{sam}, and measured reference signal, E_{ref}, which for the case of using air as a reference is shown in Figure 2.3. Further details on the experimental setup for transmission measurements taken for work contained in this thesis are given in Section 2.4. The ratio, M, is given by:

$$M = \frac{E_{sam}}{E_{ref}} = t_{as} t_{sa} e^{-i(k_s - k_a)d}, \tag{2.19}$$

where t_{as} and t_{sa} are the transmission coefficients from air to sample and sample to air, respectively. They can be calculated from Equation 2.16 or Equation 2.17. The thickness, d, of the sample is measured separately using conventional means, therefore it is known for these calculations. By using Equations 2.8, 2.9 and 2.10 in

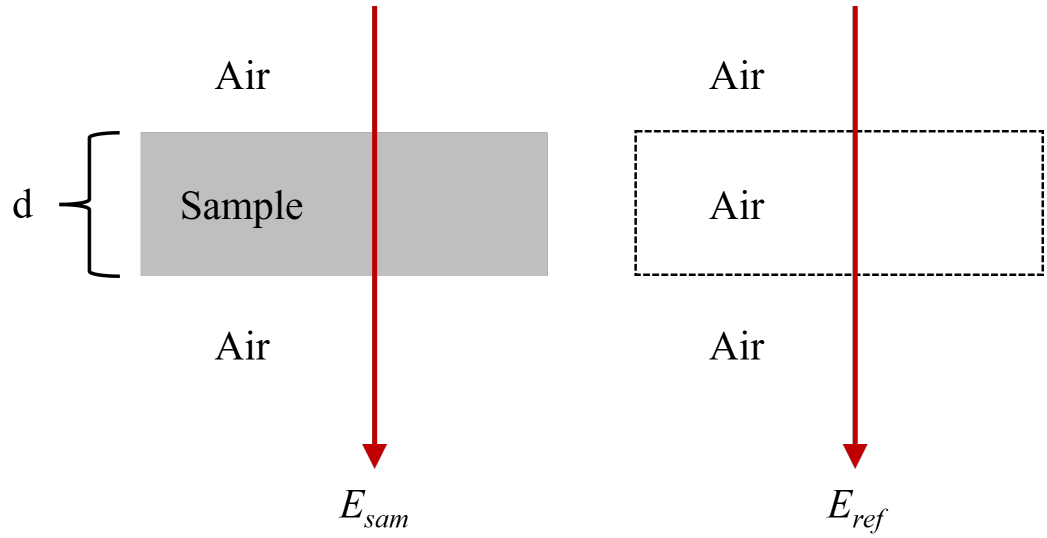

Figure 2.3: A diagram of the sample and reference signal paths in transmission geometry, for using air as the reference.

Equation 2.19, M can be rewritten as:

$$M = t_{as}t_{sa}e^{-i\frac{\omega}{c}(n_s-n_a)d}e^{-\frac{\alpha_s}{2}d}. \tag{2.20}$$

It can be observed that the amplitude of M depends upon the sample's absorption coefficient and the phase of M, φ_M, depends upon the sample's refractive index, specifically:

$$|M| = t_{as}t_{sa}e^{-\frac{\alpha_s}{2}d} \tag{2.21}$$

$$\varphi_M = -\frac{\omega}{c}(n_s - n_a)d. \tag{2.22}$$

Air has a refractive index of approximately 1 for THz frequencies. Therefore, in the common case of using air as a reference for material characterization, the following sample properties can be obtained:

$$n_s \approx 1 - \frac{c}{\omega d}\varphi_M \tag{2.23}$$

$$\alpha_s \approx -\frac{2}{d} \ln \left(\frac{|M|}{4n_s/(n_s+1)^2} \right). \tag{2.24}$$

2.3.2 Reflection Geometry

In addition to a normal angle to the sample, as for transmission measurements, the incident THz beam can be applied at other angles and a detector can be positioned to measure the THz reflection off the sample, to achieve reflection geometry. A common method for obtaining the reference signal for reflection geometry is to place a metal mirror precisely where the sample was located. However, this introduces a significant difficulty of extreme accuracy in the sample and mirror placement, as errors in this will result in inaccuracy for the phase delay and in the calculation of the sample's optical parameters. For the work contained in this thesis, a quartz imaging window method will be used for sample alignment and to obtain a reference, which is demonstrated in Figure 2.4. A key focus of this work are *in vivo* skin measurements, for which this imaging window method has additional benefits for. Many parts of the body are curved and thus very difficult to align a reflection from, but by using an imaging window the measured area can be flattened with the application of a low pressure making the alignment much more straightforward and repeatable.

However, to extract sample properties following this method, the effects of the imaging window itself must be measured and removed to isolate sample information. This is achieved by using a baseline subtraction technique, which will be explained here. Figure 2.4 schematically shows the measurement of the sample, E_{sam}, the reference, E_{ref}, and the baseline, E_{base}. The measurement of the sample contains two reflected pulses, one from the air-quartz interface on the bottom of the imaging window, indicated by the dashed red line, and the other reflection from the quartz-sample interface, represented by the solid red line. The sample must be in good contact with the top of the imaging window to ensure there is one clean reflection here, and not an air gap present resulting in further unwanted reflections. The reference measurement is taken when there is no sample present, so the reflec-

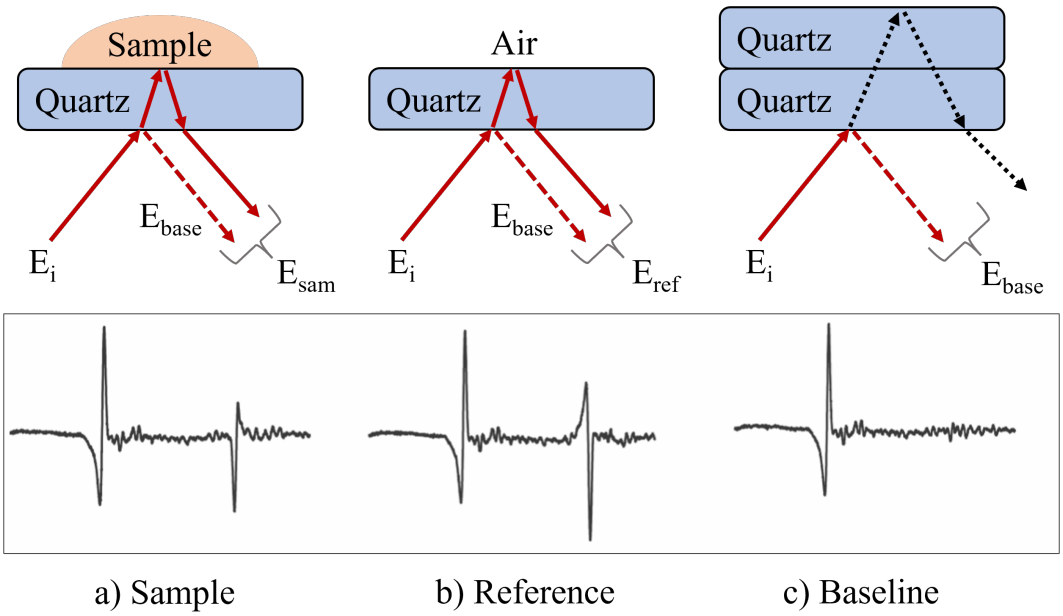

Figure 2.4: An illustration for the reflection geometry measurements using a quartz imaging window. For processing, a reference and baseline measurement are taken in addition to the sample measurement. The approximate time window is shown by the curved bracket. Examples of the measured THz pulse shapes are also given inside the box.

tion from the quartz-sample interface is replaced by a reflection from quartz-air, as compared to the sample measurement. The aim now is to remove the effect of this bottom air-quartz reflection from both the sample and reference measurements. Simply cutting the first reflection out of the data will not be sufficient, as this will not account for any multiple reflections that occur inside the quartz window, but more significantly, the notable ringing effect caused by the presence of water vapour in the air will not be accounted for, as this can persist into the sample reflection [68]. This ringing effect can be seen in the example baseline measurement, to the right of the pulse reflection. Therefore, a third measurement to isolate the first reflection, or the baseline measurement, is necessary to remove the effects that it causes on the other measurements. This is achieved by placing another piece of quartz atop the imaging window, with good contact being achieved by applying a small amount of ethanol between the two pieces of quartz and then leaving some time for it to

evaporate before the measurement is taken. The approximate time window of the measurements is shown by the grey brackets, so it can be seen that the reflection from the top of the new piece of quartz, shown by the dotted black line, will be far too delayed to be contained in the baseline measurement. It is vital that the optics remain in the same configuration relative to the imaging window throughout all the aforementioned measurements.

Now, this baseline measurement can be subtracted from the sample and reference measurements in frequency domain to eliminate any systematic artifacts or noise from using the imaging window or from the water vapour in the air. By taking the measured sample to reference ratio M is obtained:

$$M = \frac{\mathrm{FFT}(E_{sam}(t) - E_{base}(t))}{\mathrm{FFT}(E_{ref}(t) - E_{base}(t))}, \tag{2.25}$$

where FFT is the fast Fourier transform. This can be used with further frequency domain filtering to obtain a processed time domain signal:

$$\text{Processed Signal} = \mathrm{IFFT}(\mathrm{FFT}(\text{filter}) \times M, \tag{2.26}$$

where IFFT is the inverse fast Fourier transform. When the processed signal is used in this thesis, it refers to the use of a double Gaussian filter to remove low and high frequency noise.

To extract the optical properties of the sample, we begin by expressing M using the Fresnel reflection equation for s-polarised light given in Equation 2.14:

$$M = \frac{r_{qs}}{r_{qa}} = \frac{\tilde{n}_q \cos\theta_q - \tilde{n}_s \cos\theta_s}{\tilde{n}_q \cos\theta_q + \tilde{n}_s \cos\theta_s} \times \frac{\tilde{n}_q \cos\theta_q + \tilde{n}_a \cos\theta_a}{\tilde{n}_q \cos\theta_q - \tilde{n}_a \cos\theta_a}. \tag{2.27}$$

Here, r_{qs} and r_{qa} are the Fresnel coefficients for the quartz-sample and quartz-air reflections respectively, $\tilde{n}_q$, $\tilde{n}_a$ and $\tilde{n}_s$ are the complex refractive indices of quartz, air and the sample respectively. The incident angles for quartz, θ_q, air, θ_a, and the

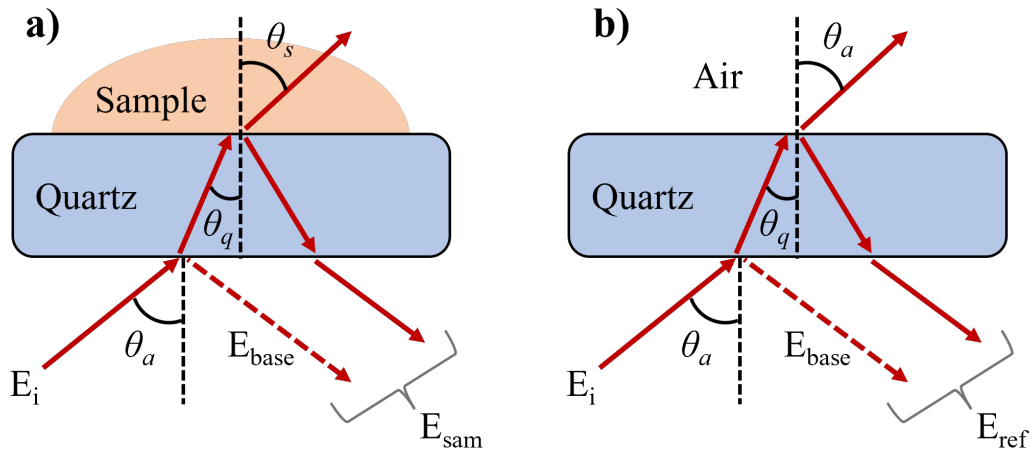

Figure 2.5: A schematic for reflection geometry measurements using a quartz imaging window and showing the incidence angles for a) acquiring the sample measurements and b) acquiring the reference measurement.

sample, θ_s, are also shown in Figure 2.5. These incident angles can be related by using Snell's law, introduced in Equation 2.12, in the complex form of:

$$\tilde{n}_q \sin\theta_q = \tilde{n}_a \sin\theta_a = \tilde{n}_s \sin\theta_s. \tag{2.28}$$

With $\tilde{n}_s$ being the only unknown variable, Equation 2.25 and Equation 2.27 can be equated with using the relations in Equation 2.28 to obtain [69]:

$$\tilde{n}_s = \sqrt{X^2 + \tilde{n}_q^2 \sin^2\theta_q}, \tag{2.29}$$

where

$$X = \tilde{n}_s \cos\theta_s = \frac{\tilde{n}_q^2 \cos^2\theta_q(1-M) + \tilde{n}_a\tilde{n}_q \cos\theta_a \cos\theta_q(1+M)}{\tilde{n}_q \cos\theta_q(1+M) + \tilde{n}_a \cos\theta_a(1-M)}. \tag{2.30}$$

It is $\tilde{n}_s$ which contains various optical properties of the sample, that were introduced in Section 2.2.1, which can be extracted by:

$$n_s = \mathrm{Re}(\tilde{n}_s) \tag{2.31}$$

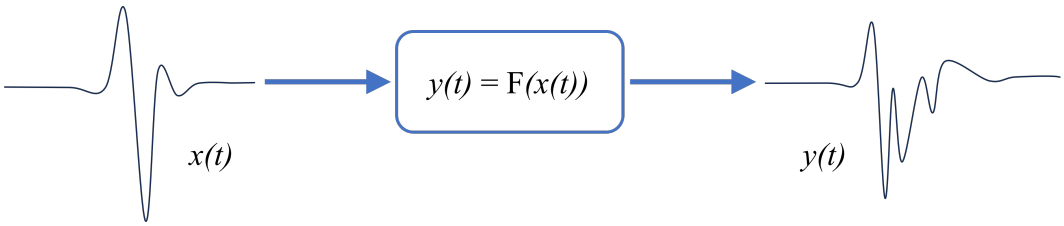

Figure 2.6: A LTI system which relates input *x(t)* and output *y(t)* via function F. For this diagram, a THz reference pulse is the input and a sample THz measurement is the output. The sample is the LTI system which transforms the initial THz pulse to the sample response.

$$\kappa_s = -\mathrm{Im}(\tilde{n}_s) \tag{2.32}$$

$$\alpha_s = \frac{4\pi f \kappa_s}{c}. \tag{2.33}$$

2.3.3 THz Spectroscopy as a Linear Time Invariant System

Alternatively, the THz measurement process can be viewed as a linear time invariant (LTI) system. A LTI system has a linear relationship between its input and output which does not change over time [70]. For this work, a sample within a spectroscopic system is considered the LTI system, which acts on the THz light. The input is considered as the reference THz measurement and the output is considered as the sample THz measurement, as depicted in Figure 2.6. The input consists of a continuous variable of time, *x(t)*, and the output consists of another variable of time, *y(t)*. The relationship between the two is the function F, which represents the system. A LTI system can always be represented as a convolution operation:

$$y(t) = \mathrm{F}(x(t)) = x(t) \otimes h(t) = \int_{-\infty}^{+\infty} x(\tau)h(t-\tau)d\tau, \tag{2.34}$$

where h is the impulse response of the system. A quantitative description of the spectroscopic sample's interaction with the THz light is the impulse response.

2.3.4 Sources of Noise and Error for THz Measurements

There are various physical sources of error which contribute towards the noise present during THz-TDS measurements, such as laser intensity fluctuations, optical and electronic noise, delay line stage jitter and mechanical drift [71]. Two major sources of thermal noise in a THz-TDS system are Johnson-Nyquist noise, which is generated when substrate charge carries fluctuate resulting in artificial voltage measurements, and background noise, which creates a random voltage across the receiving antenna. In addition to thermal noise, other specific sources of noise include quantum fluctuations and shot noise, both of which can be efficiently dealt with by signal processing techniques. As explained in Section 1.1.2, an optical delay line is used to mechanically induce a time delay on the probing THz pulse. Consequentially, the sampling time is characterised by uncertainty due to inaccurate knowledge on the delay mirrors exact location and movement. As fibers are very sensitive to small temperature changes and physical vibrations, such factors significantly contribute to error for fibre-based THz systems. This creates a pulse shift error which can be ignored for transmission measurements, however it is very impactful to reflection measurements as it limits the phase contrast. To account for this shift error, an algorithm which loops over different assumed pulse shift errors and minimises the difference between the E field found from this assumed error to the calculated E field can be implemented [72].

Furthermore, error can occur in the estimated optical properties of measured samples as this depends upon the accuracy of the physical setup and knowledge of the physical system. For example, uncertainty due to the sample alignment, the refractive index of air in the laboratory and the thickness measurement of the sample can contribute to inaccuracy in the extracted optical properties [73]. Unexpected inhomogeneities and reflections in the sample also potentially create error in extracted values, as the sample may be assumed to be homogeneous in calculations and overlapping reflections can constructively or destructively interfere with each

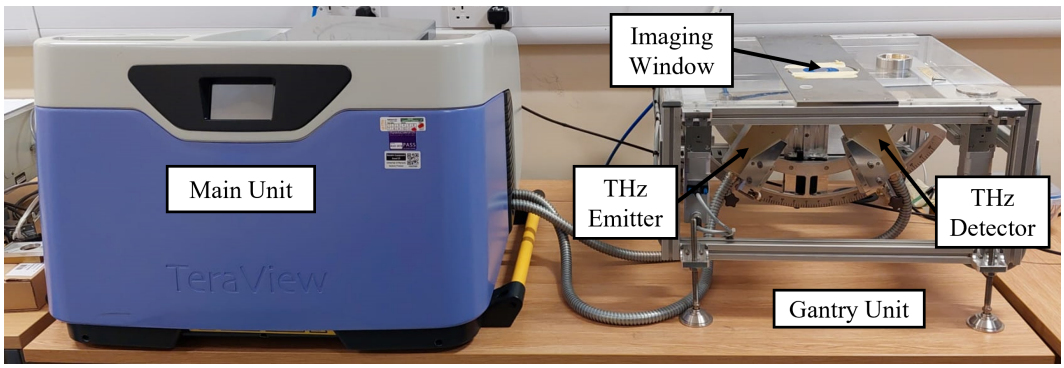

Figure 2.7: The TeraPulse 4000 spectrometer, with dimensions of 702 mm (w) x 645 mm (d) x 468 mm (h). The closed main unit generates the femtosecond pulsed laser and has a section for transmission measurements. The gantry unit is for reflection measurements and is mounted on mechanically movable rails for 2D images.

other. As an imaging window is used for reflection measurements, during image measurements inhomogeneities in the window can contribute to the error. This can be mitigated by taking area baseline and reference measurements before each set of sample images is taken, however this is time consuming. An algorithm has been developed to modify a point baseline and point reference measurement into respective area measurements [69], thus achieving suitable error mitigation much more quickly. The error from the approximated transfer function used should also be kept in mind. The work contained in this thesis takes careful measures to account for all sources of noise and error mentioned here, including the use of advanced signal processing techniques to separate overlapping reflections and minimise the effect of noise.

2.4 Experimental Setups

2.4.1 TeraView System

Two fiber coupled THz-TDS systems were used to measure data for work contained in this thesis, both of which follow the standard design outlined in Section 1.1.2. The first was the TeraPulse 4000 spectrometer produced by TeraView Ltd (Cambridge, UK), shown in Figure 2.7, which comes with a large gantry unit containing a THz

emitter and detector mounted on a system which allows quick and simple changes to the incidence angle of the THz beam to the top of the imaging window. For most of the work conducted using this system, the angle was selected to be 30 degrees. There was also a simple manual screw to change the verticality of the system to quickly adjust the alignment of the THz light to the sample. The system holding the emitter and detector was mounted on a mechanical rail, which was able to raster scan the area of the imaging window and digitally feed the positional data in with the THz measurements for the creation of 2D images. However, this 2D imaging process is too slow to obtain accurate *in vivo* skin data, due to the way skin changes throughout the measurement, which is explored in Section 3.2. Therefore, point measurements were taken for all *in vivo* skin measurements recorded. This system produced THz pulses in a usable bandwidth of 0.06 to 4 THz, but for skin measurements a range of 0.2 to 0.8 THz was used due to the scattering effects from the roughness of skin affecting higher frequency data. A rate of pulse acquisition of 30 Hz was used.

The main unit of the TeraView system seen in Figure 2.7 contained a compartment for transmission measurements, shown in Figure 2.8. The main unit also contained the femtosecond pulsed laser used for the generation of the THz light, however this was completely sealed away so use of the system in both reflection and transmission geometries was able to be conducted without any laser safety measures. For a transmission measurement, the sample would be placed into the sample holder which positioned the sample such that the THz beam would pass through the centre of the sample and be measured on the other side. Additionally, the compartment could be purged with nitrogen gas to remove the water vapour present in normal air, in order to remove the characteristic absorption peaks the presence of water can lead to.

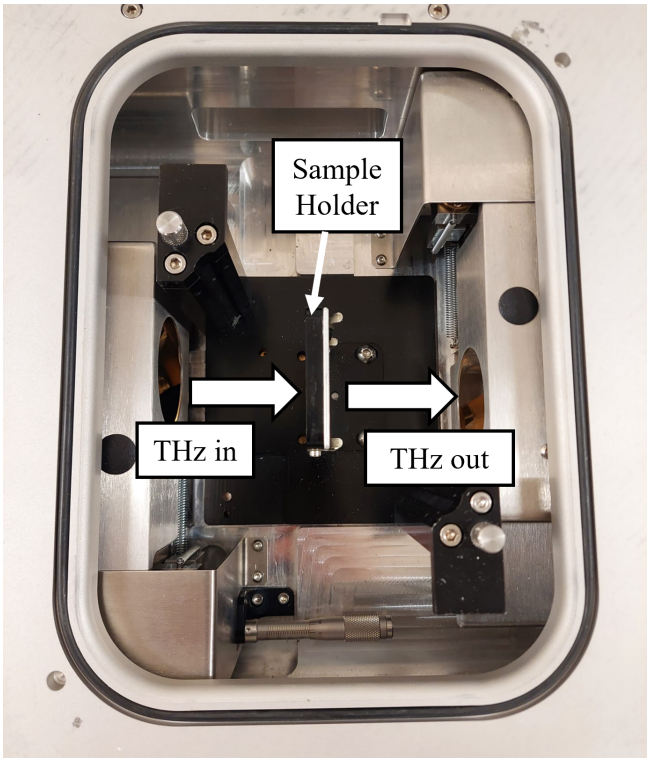

Figure 2.8: The TeraPulse 4000 spectrometer main unit transmission compartment. There is a 105 mm space between the parabolic mirrors where the THz enters and leaves the transmission compartment.

2.4.2 Menlo System

The second system used was a K15 THz spectrometer from Menlo Systems GmbH (Planegg, Germany), shown in Figure 2.9. In some ways, this system was less convenient to use as the emitter and detector were not attached to a stage like the TeraView system was, which allowed for easier adjustments to the angle of incidence and vertical changes to adjust the alignment in addition to a motorized 2D imaging system. However, the Menlo system was much more compact and allowed for more freedom in different setups, such as imaging a sample in reflection from above and attaching all components to a holder for a handheld mode of measurements. Furthermore, the smaller contact area containing the imaging window and pressure sensors meant that less skin was in contact with metal and other materials, leading

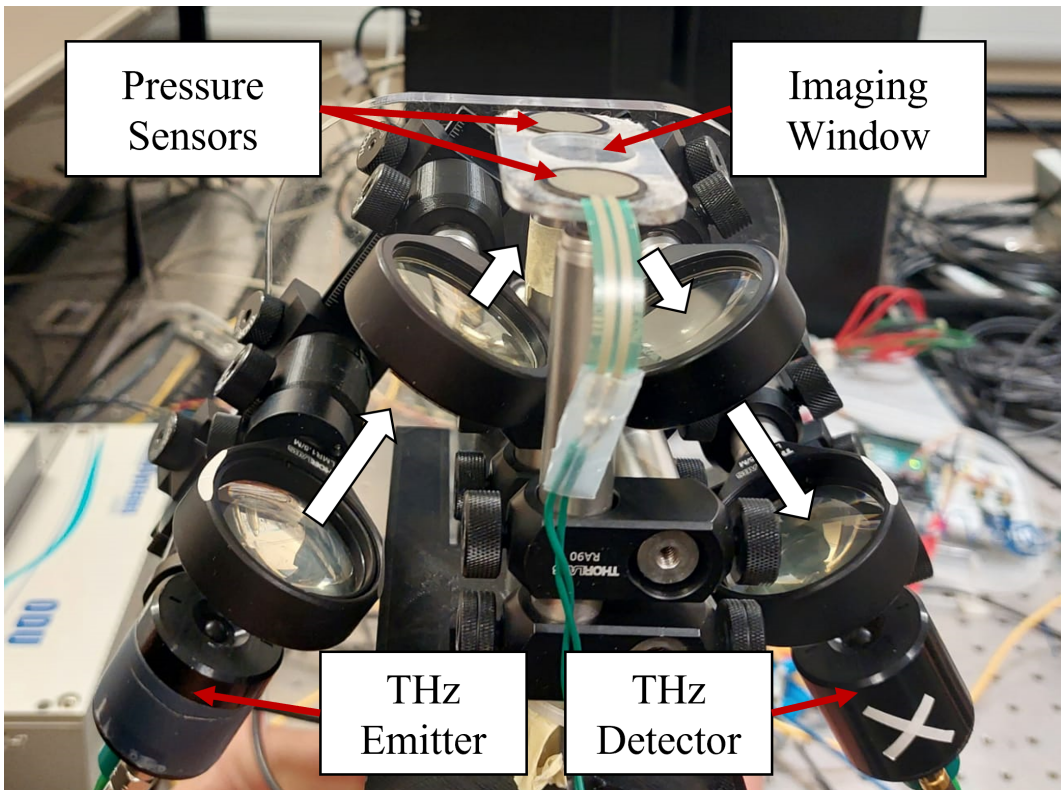

Figure 2.9: The K15 THz spectrometer set up for performing reflection measurements of skin. The white arrows indicate the THz light path. The quartz imaging window has a pressure sensor either side, to provide pressure readings during measurements. The emitter and detector are 60 mm in length.

to less unwanted changes to the skin during measurements. The pressure sensors were used to monitor and record the pressure between the imaging window and measured region of the patient, which was usually the arm, and is explained fully in Section 3.3. These pressure sensors were also applied either side of the imaging window in a similar manner for skin measurements using the TeraView system. This Menlo system is able to provide broadband THz pulses with a usable bandwidth ranging from 0.1 to 5 THz at a rate of 4 Hz. Transmission measurements made with this system were achieved by attaching the emitter, detector and sample holder to the optical bench, such that they were all in the same plane with the emitter and detector pointing at each other with the sample holder between them.

2.5 Summary

In this chapter, the fundamental theory for THz wave propagation was covered and key parameters for characterizing samples were introduced. THz wave interactions with medium interfaces were explained, using Snell's law and the Fresnel equations. For both transmission and reflection geometries, the methods to extract the optical properties of samples were described. The procedure to account for the use of an imaging window to hold the sample in reflection geometry was explained, with a key step being to account for the bottom window reflection. A simple signal processing technique was introduced, with further more complicated and effective techniques being introduced later in this thesis. Lastly, the specific THz-TDS systems used to perform the studies contained in this thesis were presented.

Chapter 3

Variables Affecting *in vivo* Skin Measurements

3.1 Introduction

In order to study skin, the variables which affect it must be controlled or accounted for so that the results can be properly interpreted. As reflection geometry and an imaging window is necessary for *in vivo* THz skin measurements, further variables which significantly impact the skin are introduced, such as occlusion of the skin. This chapter contains a summary of many variables which affect the skin, exploring the extent to which they influence THz measurements of the skin and the mechanisms which explain the cause of their effect. A robust measurement protocol is introduced, with the target of reducing the effect of the most significant variables in order to produce accurate and repeatable results for the *in vivo* studies conducted for this thesis. This protocol is suggested as a framework for the methodology of any future THz *in vivo* experiments.

3.2 Occlusion

3.2.1 The Requirement of an Imaging Window

Firstly, the reasons behind using an imaging window must be explained and justified. As detailed in Section 1.2.2, the high attenuation of THz by the substantial water content of skin leads to reflection geometry being required for *in vivo* measurements. Non-contact measurements, which are measurements without using an imaging window, are extremely difficult due to THz reflection measurements being so sensitive to misalignment and there being significant alignment issues with non-contact modalities for measurements of the skin. This is for two primary reasons; the curved, rough surface of skin leads to scattering of the THz light and the patient must remain still without direct support to the imaged area. By introducing an imaging window both of these issues are addressed, as the imaging window flattens out the skin in the area being measured and provides support to that region, making it easier for the patient to keep that part of their body stationary during the measurement. For example, if the patient's volar forearm is being measured they can lean slightly against the imaging window. Any slight movements they make will not result in misalignment, so long as some pressure is applied between their forearm and the imaging window. As opposed to this, for non-contact measurements any slight shift the patient makes can lead to misalignment.

3.2.2 Occlusion of the Skin

However, the use of an imaging window introduces further variables to account for during measurements. One of these is occlusion of the skin, where the imaging window prevents the usual breathability of the skin, shown in Figure 3.1 (a), leading to a build up of water in the stratum corneum, as demonstrated in Figure 3.1 (b). The usual breathability of skin is the evaporation of some water molecules in the stratum corneum to their environment. When this is air, the relatively low water

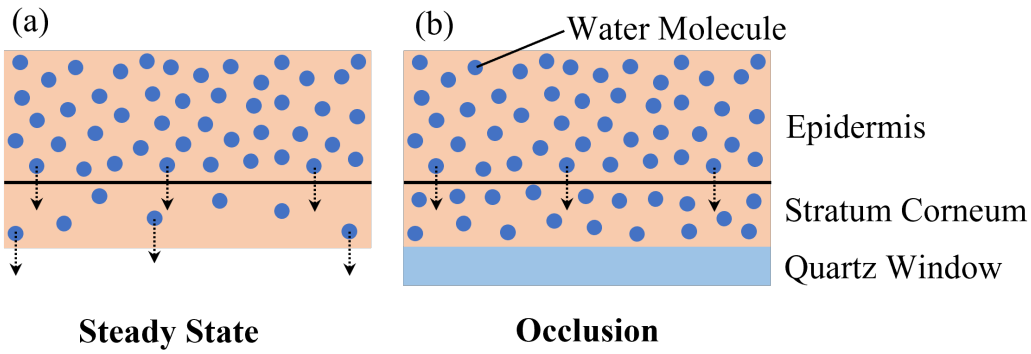

Figure 3.1: Schematic of (a) the usual steady state of skin and (b) the occlusive effect of the quartz imaging window causing a build up of water in the stratum corneum. Arrows indicate how the water molecules are travelling.

content and the flow of the air leads to fast evaporation of the water molecules. However, when the skin is covered by a non-permeable material such as quartz, this evaporation cannot take place, thus the build up of water in skin occurs. As THz light is so sensitive to water content, it is clear that this mechanic will have a significant impact on THz measurements of skin.

3.2.3 The Effect of Occlusion on THz Measurements

The effect of occlusion on THz measurements was first reported by Cole *et al.* where they identified the movement of water in the stratum corneum to be the cause [40]. However, this was not explored in depth. Sun *et al.* conducted a comprehensive study on how occlusion effects THz measurements and how to account for them [74]. They studied both rapid point measurements and area images on the volar forearm, discovering that even 5 seconds of occlusion can have a significant impact upon the THz response. Furthermore, they present the results that the first 3 minutes have the greatest occlusive effect and they propose a model to compensate for its influence.

To explore the effect of occlusion myself, I obtained the results presented in Figure 3.2. This was accomplished by placing the volar forearm against the quartz

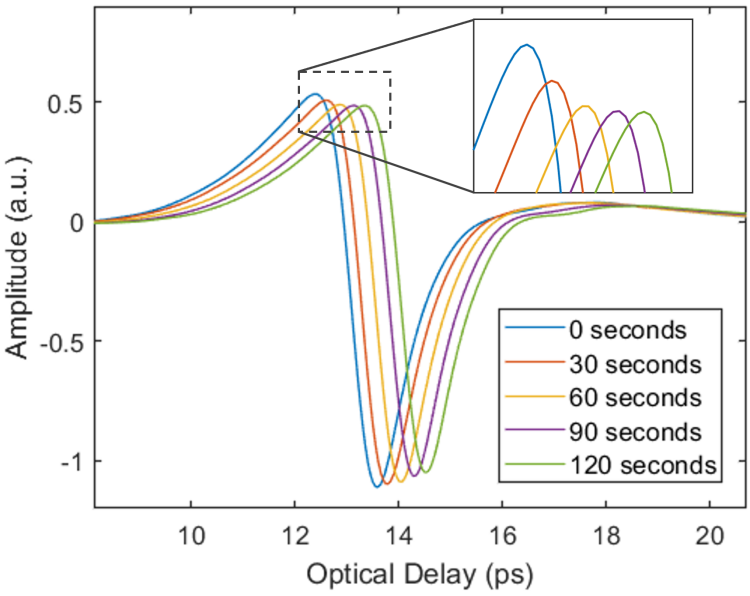

Figure 3.2: The processed reflected THz signals from *in vivo* volar forearm measurements, after an amount of time has passed since the arm was first placed onto the imaging window. The waveforms have been horizontally shifted for clarity. The inset is an enlargement of the marked region.

imaging window and taking measurements for 2 minutes, using the TeraPulse 4000 gantry stage shown in Figure 2.7. Pressure sensors were used to help maintain a constant pressure between the forearm and imaging window during this measurement. The effect of pressure on THz *in vivo* measurements will be discussed in the following section. These measurements were then processed, following the steps outlined in Equation 2.26. For clarity, only one pulse for every 30 seconds is plotted, and each pulse is shifted horizontally. The first pulse is taken immediately after good contact was made between the imaging window and forearm. The inset contains an enlargement of the marked area, so the peak decrease over time can more clearly be observed. Furthermore, it can be seen that there is a more significant decrease in amplitude during the first 60 seconds, with the decrease beginning to plateau over the following 60 seconds. The plateau is less significant for the negative amplitude decrease, meaning that there is still an increase in occlusiveness for at least the first 2 minutes of the skin being covered by the quartz window. This indicates that

water continues to be built up in the stratum corneum during this time. Occlusion introduces a significant problem for *in vivo* image scans, as the THz response of the skin will change as the system scans over the area being imaged.

3.3 Pressure

3.3.1 The Effect of Pressure on Skin

During *in vivo* skin measurements, it is necessary for a small amount of pressure to be exerted to ensure there is no significant air gap between the imaging window and the region being measured. For volar forearm measurements, this is often done by the patient pressing their arm down upon the imaging window themselves. In other situations the pressure can be applied by the person taking the measurement, such as by lightly pressing a portable THz measuring device against the patient's skin in the region being measured. However, this pressure also compresses the skin resulting in a higher concentration of water in addition to causing some mechanical deformation. Chan *et al.* investigated the *in vitro* optical properties of skin as a function of pressure by sandwiching the samples between microscope slides and using a spring-loaded apparatus to compress the sample [75]. They found that the tissue thickness and their optical properties significantly changed with the application of pressure. For example, absorption and scattering coefficients were found to increase among most of the compressed samples. Clarys *et al.* used a spring system to ensure a constant and changeable pressure of a capacitance measuring probe to measure hydration *in vivo* [76]. They showed that a higher probe pressure application on the skin surface lead to larger hydration measurements of the skin, which was more pronounced for dry skin.

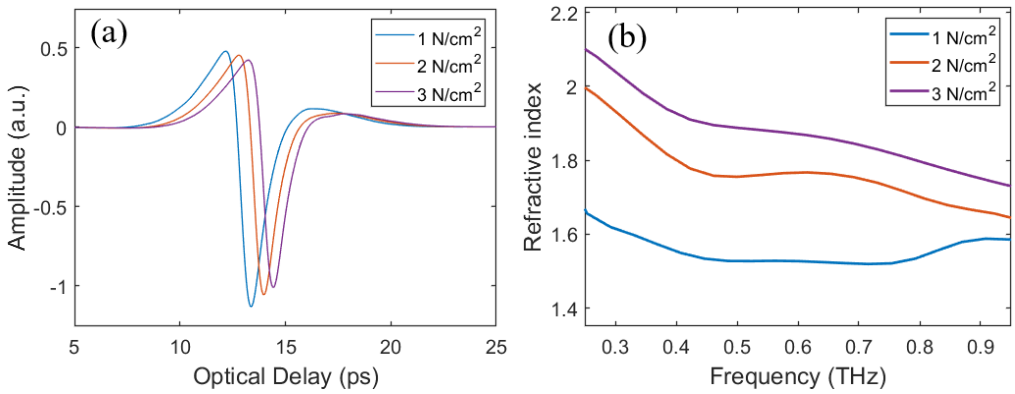

Figure 3.3: The (a) processed waveforms and the (b) refractive index of a volar forearm for varying applied pressure. The processed waveforms have been horizontally shifted for clarity.

3.3.2 How Pressure Effects THz Measurements of Skin

To explore the effect of pressure on *in vivo* THz skin measurements, I applied various light pressure during volar forearm measurements to obtain the data presented in Figure 3.3. The experimental setup was the same as for the previous section, but this time the pressure sensors were used to obtain different pressures per measurement as opposed to maintaining the same pressure throughout the experiment. Furthermore, the data was extracted for waveforms recorded after 20 seconds of contact between the arm and imaging window for all the results, to account for the effect of occlusion on the skin. Figure 3.3 (a) contains the processed waveforms for the labelled pressures, which have been horizontally shifted for clarity. It can be seen that there is a clear reduction in the amplitude of the waveform for larger applied pressures, due to the higher concentration of water in the compressed tissue. Figure 3.3 (b) shows the refractive index for the same measurements. An increase in refractive index can be observed as the pressure is increased, again associated with a higher concentration of water in the tissue. Furthermore, it can be seen that for an applied pressure of 1 N/cm^2 the refractive index could be slightly incorrect, as at this low pressure there may not be good contact between the skin being measured and the imaging window. With further investigation, it was found that 2 N/cm^2

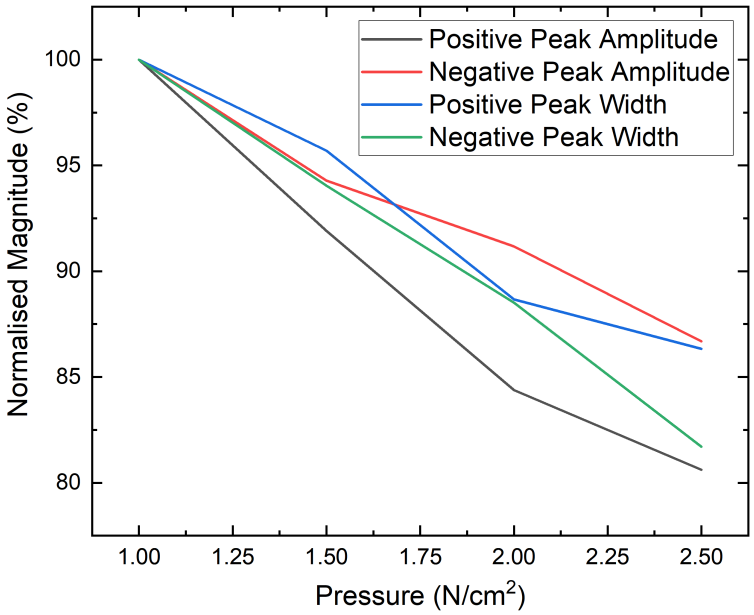

Figure 3.4: The change in THz processed waveform amplitude and width as a function of applied pressure, individually observing the positive and negative peaks which form the waveform.

was an ideal pressure to target for most skin measurements, as this ensured good contact between the skin and the imaging window whilst being a low and easily maintainable pressure to apply.

Figure 3.4 shows how the pulse amplitude and width changes as a function of applied pressure. The results are split between positive and negative peak results, which form the whole processed waveform such as those seen in Figure 3.3 (a). The results have all been normalised relative to the measurement at 1 N/cm^2. There are significant decreases for all of the peak amplitudes and widths, though there seems to be less of a decrease for the negative peak amplitude as compared to the positive peak amplitude. As such, for the most accurate comparison the peak-to-peak of processed waveforms can be compared, that is the summation of the positive and negative amplitudes. These results demonstrate the need for a consistent pressure between the measured region and the imaging window in order to compare different measurements to each other.

3.4 Patient Dependent Factors

3.4.1 Dominant Arm Difference

The vast majority of people prefer to use one hand for most purposes, called handedness in human biology. As such, their dominant hand tends to become stronger, faster and more dexterous than their non-dominant hand. This could lead to a different THz response of a person's dominant arm as compared to their non-dominant arm. For example, it has been reported that arm dominance can affect water content measurements in the volar forearm [77]. To investigate the THz response of the dominant arm compared to the non-dominant arm, I measured the left and right arms for 20 right arm dominant subjects. The pressure was kept the same over all measurements and the waveforms selected were for after the same amount of contact time between the arm and imaging window to account for occlusion. Other than this, the same experimental procedure was used as in the proceeding sections of this chapter with the addition of some extra measures fully explained in Section 3.6. The percentage variation in the processed waveform peak-to-peak between each subject's left and right arms is presented in Figure 3.5. From these measurements the average percentage variation, v, was calculated using:

$$v = \sum_{k=1}^{n} \frac{L_k - R_k}{n}, \tag{3.1}$$

where n is the number of subjects and $L_k - R_k$ is the percentage difference of the processed waveform peak-to-peak between the left and right volar forearms for the kth subject. It was found that the average percentage variation is -0.3%, with a standard deviation of 3.0%. This demonstrates that arm dominance does not significantly impact the THz response of the arm. With this knowledge, one arm could be used as a control for the other arm during *in vivo* THz studies. For example, the effect of a skin product could be studied by applying it to one arm and

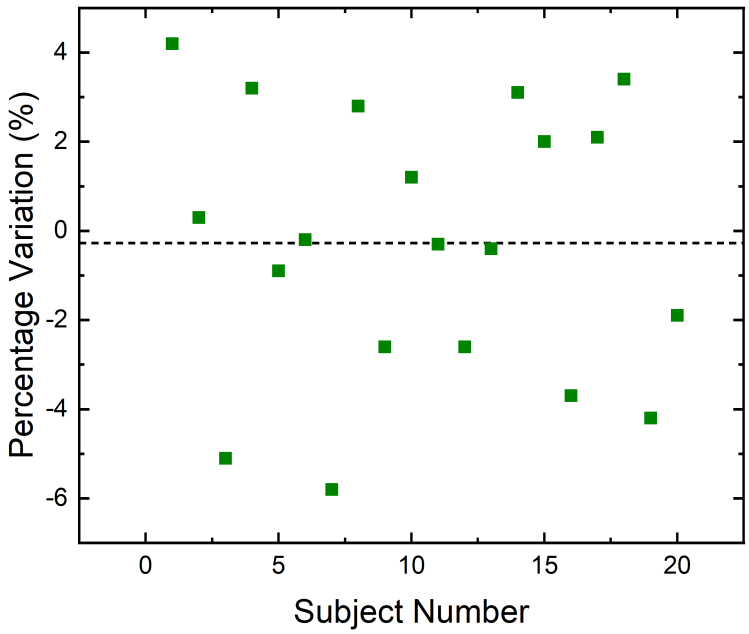

Figure 3.5: Percentage variation in the processed peak-to-peak between the left and right arms of 20 right arm dominant subjects. The dashed line represents the mean for this data.

comparing the THz response of that arm to the other untreated arm.

3.4.2 Ethnicity

It is visually clear that differing ethnicity can lead to significant changes of the skins properties from observing skin colour, which is dominated by the presence of melanin. Rawlings conducted a large review on how ethnicity affects skin structure and functions in general [78]. Key findings reported included darker skin having a stronger stratum corneum barrier function and Asian skin having a comparatively thinner stratum corneum whilst having higher water content and lipid levels when compared to skin from other ethnicities. Looking at THz imaging, Peralta *et al.* investigated the effect of skin melanin content on the optical properties of *in vitro* pigmented human skin samples from Asian, Black and Caucasian donors [79]. They concluded that the ethnicity of the donor contributed to the measured THz optical properties, such as the refractive index and absorption coefficient. Thus, for THz

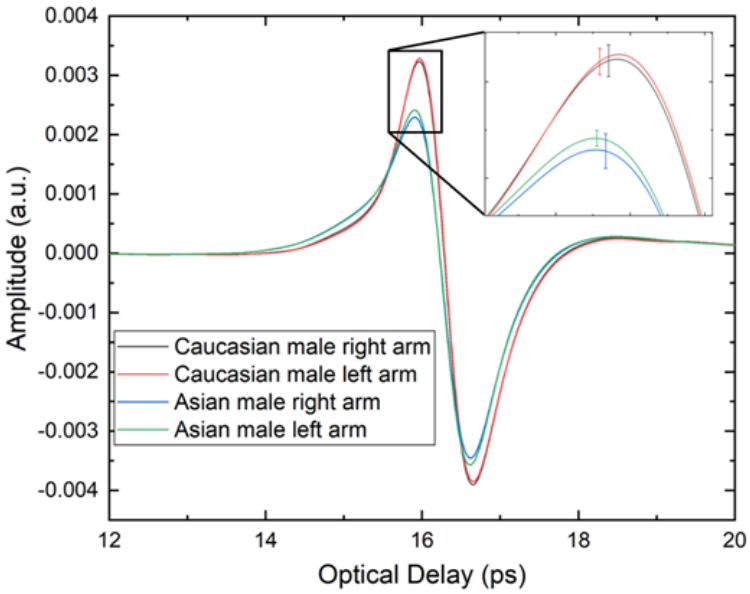

Figure 3.6: Processed reflected THz signal from *in vivo* volar forearm measurements for male Caucasians and male Asians, averaged over the 6 subjects of each ethnicity. Inset is an enlargement of the marked region, with error bars of the standard error in the mean marked.

in vivo skin measurements the ethnicity of the subject may need to be taken into account.

To explore the effect that ethnicity may have on THz skin measurements, I measured the volar forearms of 6 male Caucasian and 6 male Asian subjects. These measurements were conducted following the same procedure outlined in the previous section. The averaged processed waveforms for the left and right arms of each ethnicity measured are presented in Figure 3.6, with the inset showing an enlargement of the marker region. The errors shown are the standard error in the mean. A large difference in the peak-to-peak between Caucasian and Asian subjects can be observed, which may be due to the higher water content for Asian skin reported by Rawlings [78]. These results are clearly outside of error range, though this study is only for 6 subjects per group so a further study with a larger number of participants would be beneficial. As further evidence for the results reported in the previous section, it can be observed that for each group the averaged results for

the left and right arms are within error.

3.4.3 Gender

Firooz *et al.* conducted a study to help understand the role gender plays on the physiological, chemical and biophysical characteristics of the skin [80]. By measuring 25 males and 25 females, they discovered a significant difference in transepidermal water loss measurements in the male group indicating lower skin hydration levels. Furthermore, there were significant differences in the mean values of melanin index between the male and female groups. However, other studies have reported that no skin hydration difference between males and females could be detected when they used similar methods [81, 82]. In their review, Dao *et al.* concluded that there is a pressing need for further research into the difference between male and female skin to aid with individually tailored clinical management of disease processes, especially research in the form of randomized controlled clinical trials [82].

To compare the *in vivo* THz response of males and females a group of 24 Caucasian males and 11 Caucasian females were measured. These measurements were of the volar forearm, and conducted in the same manner as for the previous two sections. The average processed waveforms for these results are presented in Figure 3.7. As the resulting averages were within errors of each other, when using the standard error in the mean, it was concluded that gender does not have a significant effect on the THz response of skin. However, this could be investigated further by using a larger study group.

3.4.4 Tattoos

Tattoos have a clear visual effect on the skin, so it would be of interest to explore the THz response of tattooed skin. To achieve this I took 2D image scans of a tattoo on a subjects volar forearm using the raster scanning ability of the TeraPulse 4000 gantry stage shown in Section 2.4.1. For the most part, the same steps were taken

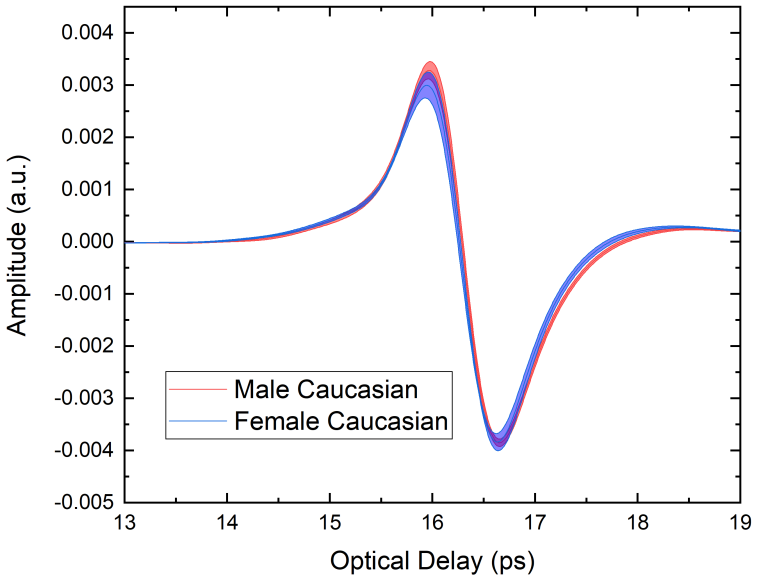

Figure 3.7: The average processed reflected THz signal from *in vivo* volar forearm measurements of 24 male and 11 female Caucasians. Solid error bars of the standard error in the mean are shown.

for the measurements as in the previous 3 sections, however as the measurements were image scans the effect of occlusion could not be accounted for. Furthermore, these measurements required a much longer time to complete than the point scans previously conducted. The results for the 10 mm by 10 mm images taken are shown in Figure 3.8 along with photographs of the area imaged. The image was taken with two different orientations by rotating the arm 90 degrees. For each image, the peak-to-peak of the processed waveforms, magnitude of M and refractive index for each point making up the measured image are presented. M is shown in Equation 2.25 and many frequency domain properties are calculated from it. M and the refractive index were calculated at 0.5 THz. For the top image it seems that the tattoo affects the THz response of the skin, as the peak-to-peak of the processed waveforms and the magnitude of M are higher in the tattooed region. However, for the bottom image these results are not replicated. It is concluded that the higher values in the tattoo region are due to an uneven pressure over the image, as this region is perpendicular to the pressure sensors. Further measurements were also taken on

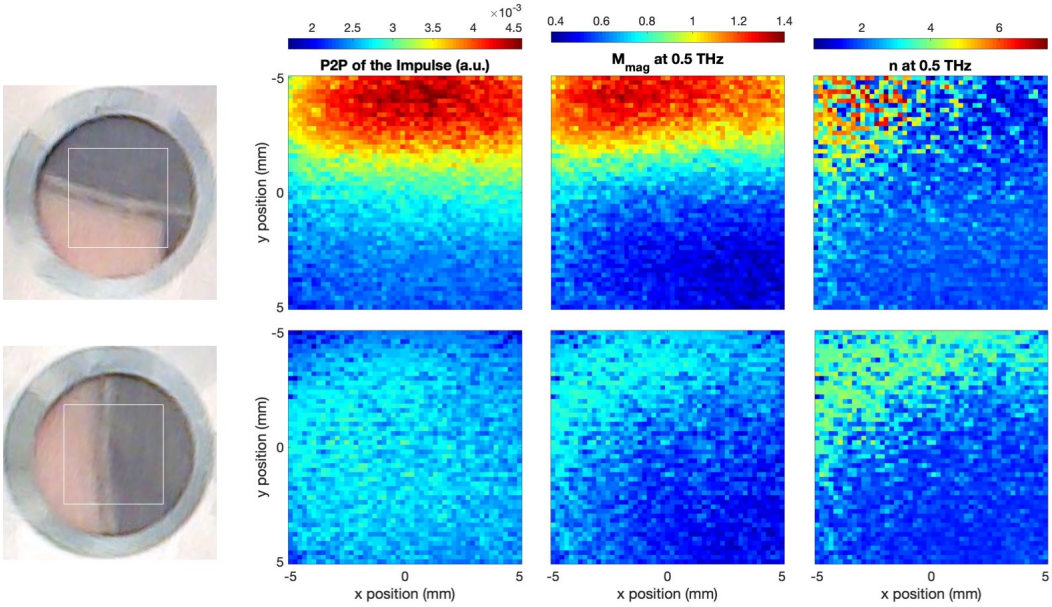

Figure 3.8: Results from image scans of a tattoo. Photographs of the imaged area through the quartz imaging window are shown on the left, the peak-to-peak of the processed waveforms are shown to the right of that, the magnitude of M as seen in Equation 2.25 is shown in the middle and the refractive index is shown on the far right. The measured region of size 10 mm x 10 mm is indicated by the white box.

tattooed skin for other subjects, however no significant change for the tattooed skin could be detected. As tattoo ink is injected deep into the skin, far beneath the stratum corneum, it is reasonable that the THz response of tattooed skin is not affected by the tattoo ink as THz light does not penetrate deep into the skin.

3.5 Other Variables

The environment a person is in can have a significant impact upon the state of their skin. For instance, it is well known that harsh weather during winter in equator far countries can cause dry and itchy skin. Engebretsen *et al.* composed a review of research behind this phenomenon, reporting that in general low humidity and low temperature lead to a decrease in the skin battier function and increased susceptibility towards mechanical stress, with the skin also becoming more reactive

towards irritants and allergens [83]. Furthermore, by comparing the skin of hundreds of women over summer and winter Qiu *et al.* discovered an increase in skin hydration and melanin content during summer, amongst other changes to the skin [84]. It has even been reported by Matsui *et al.* that skin follows circadian rhythms, where some properties of skin would change in 24 hour behaviour patterns [85].

There is far more than the environment which can affect the current state of the skin. For example, Voegeli investigated the effect of washing the skin and discovered that this resulted in a significant disrupting effect on the skin's barrier function [86]. Moreover, it has been shown by Akdeniz *et al.* that dietary fluid intake could have an impact on the hydration levels of the skin and stratum corneum thickness, however the evidence for this was not strong [87]. By comparing the dietary patterns and skin hydration of 84 healthy adults, Lim *et al.* found that specific dietary patterns could be associated with relatively higher or lower skin hydration [88].

3.6 Protocol

To address the effects of the aforementioned variables to the best of my abilities, an *in vivo* THz measurement protocol was introduced. This protocol allows for more accurate comparisons between measurements taken at different times, on different subjects and after deliberate changes to the skin have been made. Additionally, by controlling and removing effects from variables not being studied, the effects from variables of interest can better be isolated and thus more precisely examined.

The first step of the protocol was to have the subject arrive at the laboratory room, where the measurements will be made, 20 minutes before the first measurement is due to take place. This room had an air conditioning unit which could accurately control and maintain the temperature and humidity of the room, ensuring the same air conditions were kept between all *in vivo* measurements presented

in this thesis. Subjects were asked to arrive prior to their measurements as their skin would require some time to acclimatise to these conditions. The subjects were asked to ensure that the area of skin was left uncovered, for example if the volar forearm was being measured they could roll up their sleeves or remove their jumper. This was to ensure that the measured region of skin would be acclimatised to the controlled room conditions. During the acclimatisation time, signed informed consent was obtained from the subjects and all relevant information was shared with them. Additionally, information on the subject was voluntarily taken, including information such as their age, gender, ethnicity, if they had showered or swam recently or applied any skin products to the region being measured and so on. This information was compiled to be compared across large numbers of subjects to observe if any trends in the data became apparent. A brief amount of time was taken to train the subject with the use of the pressure sensors so that they could achieve the required pressure and maintain it throughout the measurement, with the pressure sensors being fully covered in the next paragraph. If multiple measurements were being taken or multiple regions were being measured, these were marked on the skin to ensure the correct area was measured.

Two flat pressure sensors (force sensitive resistors) were attached to either side of the imaging window, such as those shown in Figure 2.9. The pressure measurements were presented in real time on a monitor in clear view of the subject, such that the subject and the person taking the measurement could clearly see the measured pressure to initially adjust for the desired pressure and then to aid in maintaining that pressure throughout the measurement. The desired pressure was chosen to be 2 N/cm^2, as this was found in Section 3.3.2 to give good contact between the area being measured and the imaging window whilst being an easy and comfortable pressure to maintain. The pressure readings as a function of the THz measurement time were recorded and saved, so that the time when good contact was first achieved was recorded, i.e. the time from which occlusion of the skin would

begin, and any time when bad contact may have occurred would be recorded, e.g. from the subject significantly shifting.

The measurement time was usually 1 minute, chosen to ensure significant data would be measured with stable contact between the skin and imaging window and so that over the measurement occlusion would have a significant impact so that this could be investigated as well. The patient would place their arm onto the imaging window immediately after the measurement began, in order to determine exactly when contact was made relative to the measurement time by observing when the pressure sensors first read a pressure. If occlusion was not of interest, single waveforms measured at the same time relative to when contact was first made could be compared or the effect of occlusion could be accounted for across the whole measurement using the process detailed by Sun *et al.* [74]. Additionally, if repeated measurements of the same region of skin were taken, at least 5 minutes were left between these measurements to ensure the skin had fully recovered from the occluding effect of the imaging window from the previous measurement.

In order to account for variation between patients and over time for a specific patient, the use of a control measurement for comparison to is often necessary. Such variation could be caused by the recent diet of the patient, if they have showered recently and their ethnicity. As demonstrated in Section 3.4.1, there is no significant difference in the THz response of skin for the left and right volar forearms. As such, a THz measurement of one arm can and will be used as a control for an investigation conducted on the other, such as the application of a moisturiser or presence of a tattoo. An example of how this can be achieved is presented in the following section. The volar forearm is often used for *in vivo* THz studies as it can be easily placed onto the imaging window, has relatively few hairs which can interfere with the skin contact to the imaging window and has minimal environmental exposure, such as to UV radiation. When other regions of skin are being measured, they can be compared to the patient's volar forearm measurements to draw comparisons between patients.

Time (minutes)	Protocol Step
0	Subject arrives at the lab to acclimatise
2	Take informed consent
6	Train subject to use pressure sensors
10	Collect information from the subject
15	Mark the regions to be imaged
20	Take the first measurement
21	Take the measurement on the other arm
25	Leave 5 minutes between measurements on the same arm

Table 3.1: A summary of the proposed measurement protocol.

In the case of a study being conducted on both volar forearms simultaneously, a control region can be left on each arm to compare to. A summary of the proposed measurement protocol is presented in Table 3.1.

3.7 Normalising Results

By taking reference measurements, it enables the normalisation of our results to help account for the variation of a subject's skin over time and the variation of skin between different subjects whilst providing a value for easy comparison between these measurements. To do this, the normalised relative change (NRC) is introduced:

$$\text{NRC}(\%) = \frac{(X_{St} - X_{Sb}) - (X_{Ct} - X_{Cb})}{X_{Sb} + (X_{Ct} - X_{Cb})} \times 100\%, \tag{3.2}$$

where X_{St} is the measured parameter at time t following the change the study is observing, such as the application of moisturiser or a medical patch to the skin. X_{Sb} is the measured parameter at the same region of skin before the change was made. X_{Ct} and X_{Cb} are the same parameters for the control region of skin, measured at the same times but with the change never being made. This control region could be the subject's other arm or a designated control area near the region of skin being studied. $X_{Ct} - X_{Cb}$ represents the variation of the skin between the measurements, which accounts for the other aforementioned variation in the subject's skin, such as

if they had showered between the measurements. The other part of the denominator, X_{Sb}, helps to account for the variation between different subjects skin. An example of the measured parameter is the peak-to-peak of the processed waveform.

3.8 Summary

In this chapter, variables which affect *in vivo* THz skin measurements have been investigated. A significant change in the THz response of skin from occlusion by the imaging window was found, meaning that occlusion would have to be accounted for during such measurements. By varying the pressure applied by a subject between their arm and the imaging window, a clear change in the THz response of their skin as a function of the applied pressure was discovered. A significant difference in the processed waveform of volar forearm measurements between Caucasian males and Asian males was found. No significant difference between the dominant and non-dominant arms of the subjects, from the gender of the subject or the presence of tattoos on the measured skin were observed. This demonstrated that one arm could be used as a control for an experiment conducted on the other. Literature covering the effect of some other factors on skin was presented, such as the humidity and temperature of the air as well as the recent diet of the subject. A full measurement protocol was detailed, to account for the effects of the variables explored and discussed in the rest of the chapter. Finally, the NRC was introduced as a measure of normalising results to account for the variation of skin over time and the variation of skin between different subjects.

Chapter 4

Finite Rate of Innovation Applied to THz

4.1 Introduction

Continuous signals, such as THz light, must be reduced to a discrete form for experimental data acquisition and processing, a process called sampling the signal. Therefore, a sampling rate must be selected, balancing the ability to retain important features from the data set with the speed of data acquisition and size of the data set. A famous theorem on this aspect is the Shannon-Nyquist theorem, which states that for a perfect reconstruction of a bandlimited signal a minimum sampling rate of double the maximal frequency is required. Thus, for secure retention of important data features, a floor is placed on the minimum sampling rate allowed, resulting in a constraint for data acquisition speed.

Methods which employ finite rate of innovation (FRI) theory [89] have met with great success in minimizing the sampling rate whilst ensuring retention of important information. This theory utilizes signals with a finite number of degrees of freedom per unit time, which pulsed signals such as those used in ultrasound and THz-TDS consist of. Simple examples of suitable signals are presented in Figure

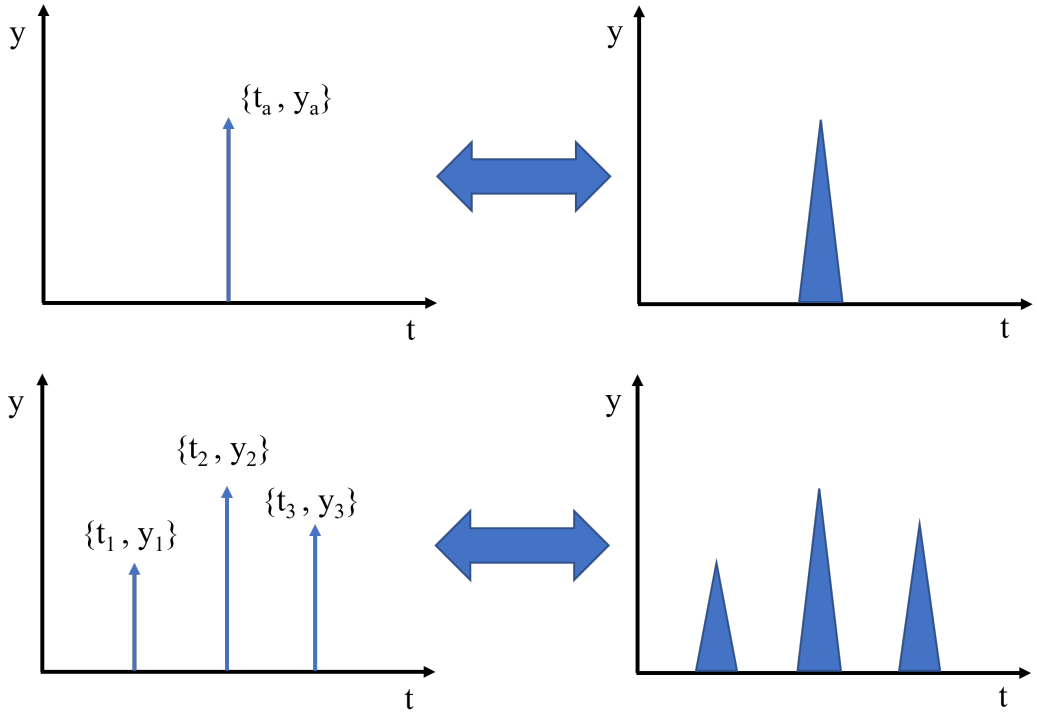

Figure 4.1: An illustration of the time positions and amplitudes shown on the left which define the peaks for the simple signals shown on the right.

4.1. Here, the time positions and amplitudes alone, shown on the left, are sufficient to fully define the simple signals on the right, given knowledge of the peak shape. The signal presented at the top of the figure has 2 degrees of freedom and the signal presented at the bottom has 6 degrees of freedom, when setting the unit of time to include the full signal. The FRI concept will be further explained and mathematically defined in the following section.

Recently, FRI theory has been employed to achieve low sampling rates, with respect to the relevant traditional sampling schemes, by Tur *et al.* in both ultrasound simulated and experimental data [90], as well as by Han *et al.* in a simulated terahertz context in communications application [91]. Han *et al.* demonstrated that, given knowledge of the pulse shape and number of reflections or pulses expected, a sampling rate even below the Shannon-Nyquist limit can be employed to achieve a full reconstruction of the sampled data. It has also been shown to handle the recon-

struction of sparse signals robustly, such as by Pan *et al.* with their application for source resolution in radioastronomy [92]. They were able to accurately reconstruct point sources from non-uniformly sampled and severely noisy Fourier measurements. Compared to current state of the art methods, their method demonstrated significant improvements. Furthermore, in a frequency-domain optical-coherence tomography context Seelamantula *et al.* used a FRI method to achieve improved resolution and signal-to-reconstruction noise compared to the standard approach, overcoming the limited resolution of this data acquisition method due to Heisenberg's uncertainty principle [93].

In this chapter a THz FRI signal processing method is explained, including the THz specific sampling kernel formation. To the best of my knowledge, such a method has not been tailored to THz light experimentally in publications, other than in my work. The aim of this method is to achieve lower sampling rates compared to current popular methods by utilizing FRI theory whilst maintaining similar experimental methodology and required foreknowledge of the sample. This method was verified with simulated THz data and simple experimental results. By applying this THz FRI method to measurements of skin underneath medical dressings, it was possible to find the thickness of different parts of the dressing and monitor the hydration level of the skin which is linked to the presence of antiseptic cream. This was all achieved at relatively low sampling rates, demonstrating the ability of this method to achieve much faster data acquisition whilst ensuring comparably accurate results.

4.2 Theory

4.2.1 Forming the Sampling Kernel

The first building block for creating this FRI method is to simulate the THz pulse shape we expect from our experiment in a form which is compatible with later

mathematical manipulations. In the frequency domain, sum of sincs (SoS) is the usual form utilized as the sampling kernel for these methods [94]. This is because the kernel approximates a reflection or transmission response, and therefore is able to solve both non-periodic and periodic cases whilst having a finite duration itself which is easily mathematically manipulated. It is defined in general terms by [90]:

$$H(\omega) = \sum_{p \in \Pi} d_p \text{sinc}\left(\frac{\omega}{2\pi/\tau} - p\right), \tag{4.1}$$

where p is an integer in the chosen set of integers Π, ω is the frequency and τ is the period containing an entire repetition of the SoS as this forms the repeating sampling kernel required for this method. The chosen integer number set Π and d_p are free parameters optimized for the specific application (explored later in this section). In the work contained in this chapter we apply this method mainly in the time domain, as the experimental data used in this work as well as all THz-TDS are acquired in that domain. Thus, we require the time domain version of Equation 4.1:

$$h(t) = \text{rect}\left(\frac{t}{\tau}\right) \sum_{p \in \Pi} d_p e^{i\frac{2\pi p t}{\tau}}, \tag{4.2}$$

where t is the time and $\text{rect}\left(\frac{t}{\tau}\right) = 1$ for $-\frac{\tau}{2} \leq t \leq \frac{\tau}{2}$ whilst being zero elsewhere, limiting the time range to only contain one repetition of the sampling kernel. The result of setting the free parameters $\{d_p\}$ to 1 and choosing $\Pi = \{-P, ..., P\}$ with $P = 25$ can be seen in Figure 4.2 (a). Here, the central peak is surrounded by side lobes being far from the real THz pulse representation, demonstrating the need for further work to mold our sampling kernel. This will come in the form of applying a length-N symmetric Hamming window for the free parameters:

$$d_p = 0.54 - 0.46\cos\left(2\pi\frac{p + \frac{N}{2}}{N}\right), \qquad p \in \Pi, \tag{4.3}$$

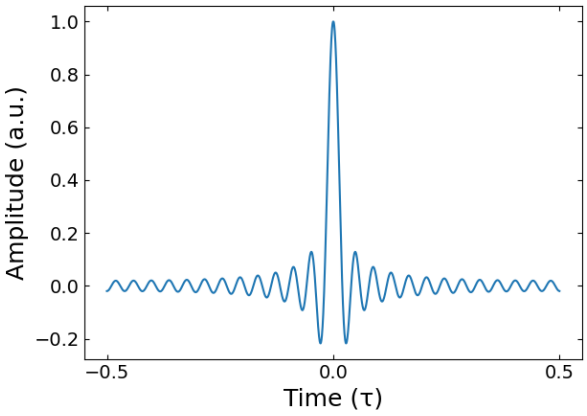

(a) Time domain response for the SoS sampling kernel. Described by $h(t)$ from Equation 4.2 for $P = 25$.

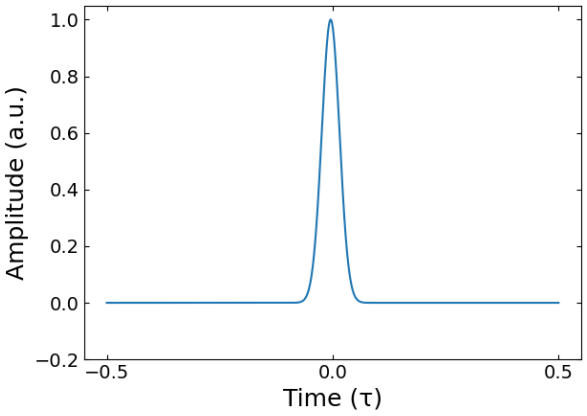

(b) The resulting kernel after a Hamming window is applied to the SoS sampling kernel shown in (a).

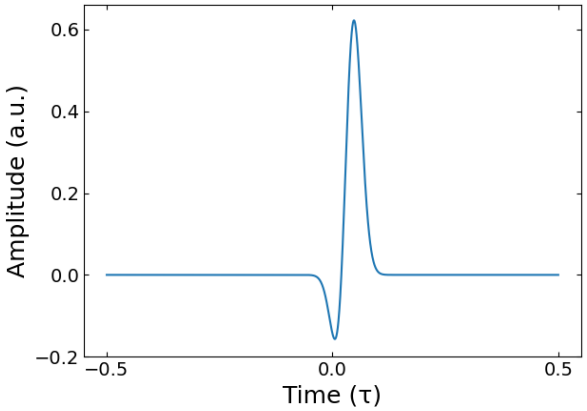

(c) Our THz-like sampling kernel. Created by combining two Hamming windowed SoS sampling kernels shown in (b).

Figure 4.2: The progression of the sampling kernel through our methodology.

where the cardinality $N = \mid \Pi \mid$. Figure 4.2 (b) shows the result of applying this Hamming window, with the side lobes being smoothed out to give a closer appearance of a single peak. To generate a sampling kernel which represents a single THz pulse two of these SoS peaks were combined, by offsetting and scaling one of the SoS pulses, as shown in Figure 4.2 (c). The offset between the pulses was equal to the width of the center peak at 0 amplitude and the relative scaling difference is a factor of -0.6. These were selected by comparing to a real THz reference and can be automatically tailored to a specific experimental reference as demonstrated later in this chapter.

4.2.2 Representation of Data Suitable for FRI

Finite streams of pulses can be used to represent THz-TDS data, finite by virtue of the data acquisition range used and the stream of pulses representing the THz waveforms constituting the data, i.e. reflections off boundaries between materials of different refractive indices. So, let us consider a τ-periodic stream of L pulses with amplitudes a_l located at distinct times t_l:

$$x(t) = \sum_{m \in \mathbb{R}} \sum_{l=1}^{L} a_l h(t - t_1 - m\tau). \tag{4.4}$$

Here, $h(t)$ is a known pulse shape, which in our case had been constructed and defined in the previous section and is in the form shown in Equation 4.2. For this consideration, we also have the constraints of $t_l \in [0, \tau)$, $a_l \in \mathbb{C}$, $l = 1...L$, $\{t_l, a_l\}_{l=1}^{L}$ and an additional constraint on $N \geq \mid \Pi \mid \geq 2L$. Given that we have L pulses which are each fully described by two parameters, the amplitude and time location, we have $2L$ degrees of freedom per unit time and so a finite rate of innovation, ρ, of:

$$\rho = \frac{2L}{\tau}. \tag{4.5}$$

With the aim of achieving the minimum sampling rate whilst being able to adequately reconstruct the sample we can target $2L$ samples per τ. This is the ideal minimal number of samples required using this method, which can result in sub-Nyquist rates. However, this ideal sampling rate does not account for issues such as sampling points not containing useful information, i.e. not lying on the pulse, or the presence of noise and other aberrations. By defining the periodic extension of our pulse shape $h(t)$ as:

$$g(t) = \sum_{m \in \mathbb{Z}} h(t - m\tau) \tag{4.6}$$

we can apply Poisson's summation formula [95] to rewrite Equation 4.6 above as:

$$g(t) = \frac{1}{\tau} \sum_{k \in \mathbb{Z}} H\left(\frac{2\pi k}{\tau}\right) e^{i\frac{2\pi k t}{\tau}}, \tag{4.7}$$

where $H(\omega)$ represents the Fourier transform of $h(t)$. By substituting this result into Equation 4.4:

$$\begin{aligned} x(t) &= \sum_{l=1}^{L} a_l g(t - t_l) \\ &= \sum_{k \in \mathbb{Z}} \left(\frac{1}{\tau} H\left(\frac{2\pi k}{\tau}\right) \sum_{l=1}^{L} a_l e^{-i\frac{2\pi k t_l}{\tau}} \right) e^{i\frac{2\pi k t}{\tau}} \\ &= \sum_{k \in \mathbb{Z}} X[k] e^{i\frac{2\pi k t}{\tau}}, \end{aligned} \tag{4.8}$$

where we have used $X[k]$ to denote the bracketed terms in the preceding line, which are the Fourier coefficients of that line. It can be shown [89] that once at least $2L$ Fourier coefficients are known, the amplitudes and time locations of the stream of pulses representing our data can be found. This enables the reconstruction, or estimation, of our data, given a suitable sampling kernel.

4.2.3 Extracting the Fourier Coefficients

We now require a way to calculate what these Fourier coefficients are. We begin by considering the uniform sampling of signal $x(t)$ of the form seen in Equation 4.4 with a sampling kernel of the form shown in Eqution 4.2, which gives a sufficient characterization of $x(t)$ with uniform samples N at locations $t = nT$:

$$y_n = \langle h(t - nT), x(t) \rangle = \int_{-\infty}^{\infty} h(t - nT)x(t)dt, \qquad n = 0, ..., N - 1. \tag{4.9}$$

By substituting Equation 4.8 into Equation 4.9:

$$\begin{aligned} y_n &= \sum_{k \in \mathbb{Z}} X[k] \langle h(t - nT), e^{i\frac{2\pi kt}{\tau}} \rangle \\ &= \sum_{k \in \mathbb{Z}} X[k] H\left(\frac{2\pi k}{\tau}\right) e^{i\frac{2\pi knT}{\tau}} \\ &= \sum_{k=-L}^{L} X[k] e^{i\frac{2\pi knT}{\tau}}. \end{aligned} \tag{4.10}$$

Here, when T is a divisor of τ, as it is in our case, this reduces line 2 in the above equation to the inverse discrete-time Fourier transform of $X[k]$ resulting in line 3 [89]. Utilizing Prony's method [96], we now introduce the annihilation filter, $A[k]$, stage of the method, with it by definition being required to satisfy the convolution:

$$A[k] \otimes X[k] = 0. \tag{4.11}$$

By satisfying this constraint, and in the case of our chosen sampling kernel with $X[k]$ reducing to:

$$X[k] = \frac{1}{\tau} \sum_{l=1}^{L} a_l e^{-i\frac{2\pi kt_l}{\tau}}, \qquad k \in \mathbb{Z}, \tag{4.12}$$

we can present $A[k]$ in the form of its z-transform:

$$A[z] = \sum_{k=0}^{L} A[k] z^{-k}. \tag{4.13}$$

This is as $A[z]$ has L zero valued null terms at $c_l = e^{-i\frac{2\pi t_l}{\tau}}$, allowing $A[k]$ to be represented by the convolution of L elementary filters [97], each of which zero out one of the sum of L exponentials in $X[k]$ for the convolution in Equation 4.11. Now, we can construct a rectangular Toeplitz matrix $\mathbf{X}$, from $X[k]$:

$$\mathbf{X} = \begin{bmatrix} X[-M+K] & X[-M+K-1] & \dots & \dots & X[-M] \\ X[-M+K+1] & X[-M+K] & \dots & \dots & X[-M+1] \\ \vdots & \ddots & \ddots & \ddots & \vdots \\ \vdots & \ddots & \ddots & \ddots & \vdots \\ X[M] & X[M-1] & \dots & \dots & X[M-K] \end{bmatrix}, \tag{4.14}$$

where $M, K \geq L$. Note that the matrix has a number of columns equal to $K+1$ and number of rows equal to $2M-K+1$. Along with the matrix form of $\mathbf{A} = [A[0], A[1], ..., A[L]]$ we can solve Equation 4.11, with the additional constraint for our sampling number of $N \geq 2M+1$, by performing the singular value decomposition [98] of $\mathbf{X}$ and selecting the eigenvalues corresponding to the smallest eigenvector, giving the annihilation filter coefficients for $\mathbf{A}$. This allows us to find the roots c_l of $A[z]$, with obtaining the time locations t_1 clearly following. With the time locations found, the last piece of information needed is the amplitudes a_l which can be calculated using the Vandermonde system [99]:

$$\begin{bmatrix} X[0] \\ X[1] \\ \vdots \\ X[L-1] \end{bmatrix} = \frac{1}{\tau} \begin{bmatrix} c_0^0 & c_1^0 & \dots & c_{L-1}^0 \\ c_0^1 & c_1^1 & \dots & c_{L-1}^1 \\ \vdots & \vdots & \dots & \vdots \\ c_0^{L-1} & c_1^{L-1} & \dots & c_{L-1}^{L-1} \end{bmatrix} \cdot \begin{bmatrix} a_0 \\ a_1 \\ \vdots \\ a_{L-1} \end{bmatrix}, \tag{4.15}$$

where the exponent denotes the power to which the term is taken to. As we have distinct t_l this system always has a solution, providing our amplitudes.

4.3 Simulated Results

4.3.1 Noiseless Model

To verify this FRI method for THz signals a simulated signal was generated using the same method as the previously described THz appropriate sampling kernel creation. Five Dirac peaks were randomly generated, each representing the amplitudes, a_l, and time positions, t_l, of simulated THz pulses, so $L = 5$. τ was arbitrarily chosen to be 1, resulting in an FRI of 10. M and P were both taken to be $5L$ and K taken as L; these values were selected according to the limitations outlined for them in the previous section and by balancing the code runtime with the quality of our results. Larger values for M,P and K resulted in longer runtimes but provided better-quality results. These Diracs representing the amplitudes and time locations are shown by the blue peaks in Figure 4.3 (a), with the resulting simulated THz data shown in Figure 4.3 (b) in green. This was then uniformly sampled as seen in the 25 red data points in Figure 4.3 (b). By following the methodology outlined in the previous section we obtain the orange Dirac peaks in Figure 4.3 (a), which represent the estimated amplitude and time location of the THz pulses that constitute our simulated signal. As we know the sampling kernel, we can recreate the original simulated THz data which is shown by the dashed blue line in Figure 4.3 (b).

In both representations of the output data, it can be seen that there is close agreement between the estimated output and the simulated input; in Figure 4.3 (a) the amplitudes and time locations of the Dirac peaks closely match, and this is further demonstrated by comparing the reconstructed signal with the original in Figure 4.3 (b). As the pulse shape used to create the simulated data is exactly known, this difference in reconstructed and original signal is an effective measure

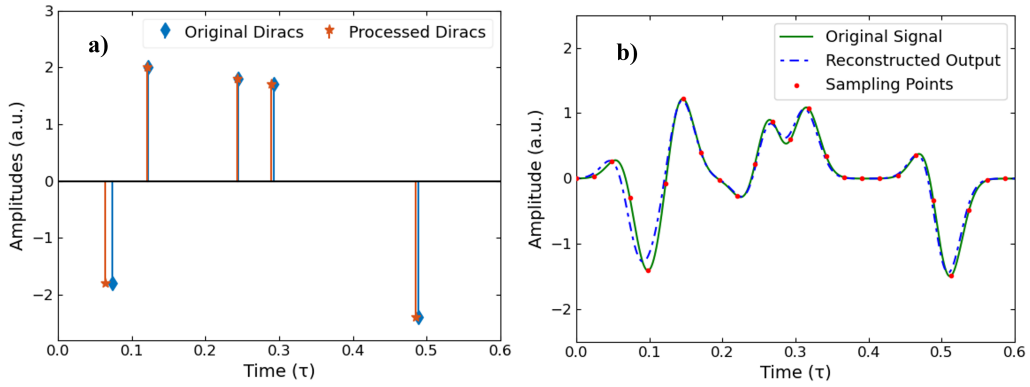

Figure 4.3: Noiseless simulated results. (a) The blue peaks represent the simulated THz pulses' time locations and amplitudes with the orange Diracs being the FRI method processed results. (b) The simulated signal (green line) was sampled (red points) to input into the FRI code. The reconstructed signal (dashed blue line) was calculated using the calculated time locations and amplitudes shown in (a) along with the known sampling kernel.

of the performance of our method. By contrasting the last pulse in Figure 4.3 (b), which is completely isolated, with the two pairs of closely neighboring pulses the rest of the data consists of, it is demonstrated that even when the pulses are overlapping and not distinguishable by eye the amplitudes and time locations can still be found with great accuracy. Crucially, this has all been achieved whilst using a relatively low sampling rate of a total of 25 points, with it being further seen that there are only a few sampling points describing each of the pulses. In particular, there are only 3 or 4 sampling points that fall within the simulated pulses however we are still able to extract the pulses' exact amplitude and time location. This exemplifies a key benefit of this method, low sampling rates which allow for faster data acquisition without losing information about our signal.

4.3.2 Noise Model

No experimental data is completely free of noise, so to simulate this effect Gaussian white noise was added to result in a signal-to-noise ratio (SNR) of 6 dB, the result of which can be observed on the sampling points in Figure 4.4 (b). Although this is

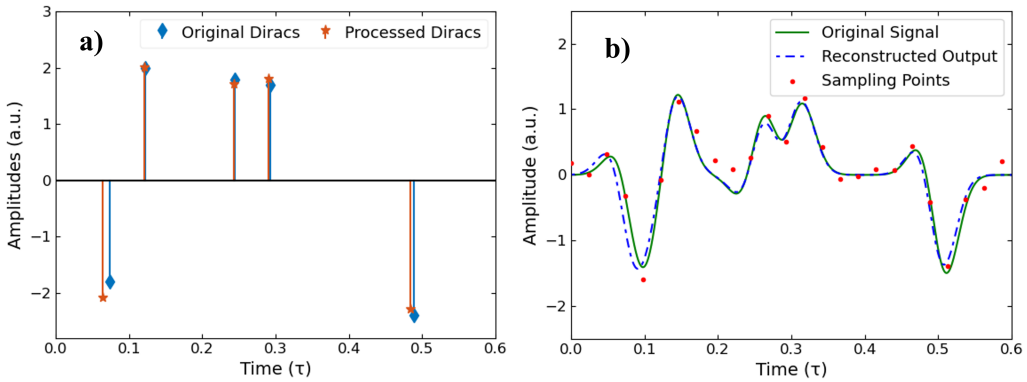

Figure 4.4: Simulated results with a Gaussian white noise model to give a SNR of 6 dB. (a) Simulated results in the presence of noise (orange), with the original (blue) for comparison. (b) Reconstruction of the simulated signal with the presence of noise (dashed blue line), compared to the original noiseless signal (green line) and the sampling points (red points).

a significant amount of noise, more so than would usually accompany experimental THz measurements such as those shown later in this chapter, the reconstruction is shown to almost completely negate the effect of the noise. This is demonstrated by comparing the processed Dirac results shown in Figure 4.4 (a) to those in the noiseless model seen in Figure 4.3 (a). We can see that in both models the processed Diracs are close to the original Dirac peaks whilst also being very similar to each other. Additionally, by observing how closely the reconstructed and the original signal match in Figure 4.4 (b), further evidence for the effectiveness of removing the effect of noise is given.

4.4 Experimental Results

4.4.1 Experimental Verification of the FRI Method

We have shown the great potential of our FRI model in the previous sections, by achieving an accurate reconstruction of the simulated signal both without and with the presence of white Gaussian noise whilst using a relatively low sampling rate. However, there are further challenges to applying this method to experimental re-

sults. Primarily, this challenge is in the accuracy of our sampling kernel in representing the THz pulse and accounting for how this pulse would change shape during transmission and reflection through different materials.

The THz-TDS system described in Section 2.4.1 was used in reflection geometry to measure the air-plastic reflection off a thick piece of plastic. By using this as an experimental reference, the method described in Section 3.2.1 was employed to create a SoS which closely resembled the shape of this reference. Ideally, the SoS sampling kernel created in this way would closely resemble the pulse in our simple experimental data obtained from a thick plastic sheet. This was measured using the same experimental procedure as for the reference acquisition and with the interface causing both reflections being between air and plastic. The SoS form of our reference is required in most of the FRI method, however it is not for the final stage of calculating the amplitudes. Instead of using the Vandermonde system, a standard least-squares minimization technique between the original measured signal and measured reference repeated at the time locations found in the previous step was used. For the recreation of the signal, we used the time location and amplitude estimates along with the measured reference. This achieved a signal shape more similar to the original, as the measured reference more closely resembled the correct shape as compared to the SoS reconstruction of it. Additionally, as we are expecting two reflections from our data, one from each surface of the plastic block, we used $L = 2$. All other variables were selected to be the same as for the simulated results in Section 4.3.

Figure 4.5 (a) contains this simple experimental data. The raw measurement is shown by the green line with the reduced sampling points used as the input for our method shown by the red points and the reconstructed output of the FRI method shown by the blue dashed line. It can be seen that there are relatively few data points describing each of the two reflection pulses, but despite this the reconstruction is a close match to the original experimental data. This indicates that the time

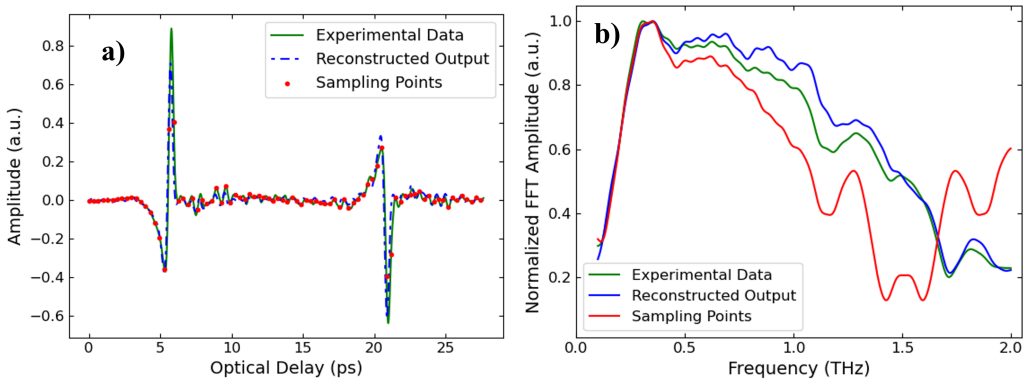

Figure 4.5: Experimental verification of our THz FRI method. (a) The raw data, shown by the green line, are reflections off the sides of a thick plastic sheet. The sampling points are shown by the red dots, which were used as the input for the method. The resulting reconstruction is shown by the dashed blue line. (b) The normalized FFT for these data.

locations and amplitudes of the reflections found by our method are accurate, as by using these in combination with our measured reference as the basis for the reconstruction we obtain a similar result to the original data. However, it can be noticed that there is a mismatch in the amplitudes of the second halves of the pulses, between the raw experimental data and the reconstructed result from our method. As the amplitudes for the first halves of the pulses are a close match, this is likely the result of an imperfect estimation of the pulse shape. Compared to the standard amount of data points the THz system we were using measures we downsampled by a factor of over 45 to obtain the sampling points shown, which resulted in a time sampling interval of 0.33 ps. This indicates that by using this method, fewer data points could be measured and thus a much shorter data acquisition time can be achieved.

Figure 4.5 (b) shows the frequency domain version of the data presented in Figure 4.5 (a), after it has undergone a FFT and has been normalized. The low sampling rate FFT, shown by the red line, begins to diverge from the fully sampled experimental data FFT, shown in green, from around 0.7 THz. For frequencies larger than 1.3 THz there is mostly a very significant difference in the normalized

FFT amplitudes, showing the frequency domain inaccuracy of the low sampling rate data at these frequencies. Crucially, the FFT of the reconstruction from the low sampling points using our FRI method, shown by the blue line, does not share this divergence and inaccuracy. This demonstrates that our method accurately reconstructs the frequency domain data of THz-TDS measurements taken at low sampling rates, providing the benefit of quicker measurements whilst ensuring the retention of frequency domain information.

4.4.2 Low Sampling Rate for Skin Measurements

In the previous section we have demonstrated that our THz FRI method produces excellent results at low sampling rates for simple experimental data taken on plastic sheets and blocks. However, the focus of this thesis is on *in vivo* skin measurements using THz, so in this section we will investigate the effectiveness of this method at processing skin measurements at a low sampling rate. To obtain this data the Menlo system in reflection geometry was used, which was described in Section 2.4.2. The THz pulse produced from this system is significantly different to the one produced by the TeraView system used in the previous section, thus the sampling kernel used to process this data in the FRI method will have to be redesigned. It was found that instead of the length-N symmetric Hamming window previously used for the sampling kernel, as shown in Equation 4.3, an adjusted window in the form of:

$$d_p = 0.54 - 0.26\cos\left(2\pi\frac{p+\frac{N}{2}}{N}\right), \qquad p \in \Pi, \tag{4.16}$$

performed best. As previously shown in Figure 4.2, two of these sampling kernels are combing for a THz-like kernel. Figure 4.6 shows the sampling kernel we created for this skin data in blue, as compared to the experimentally measured reference shown in green. The measured reference was taken from the bottom reflection off a quartz imaging window, as this imaging window will be used to acquire the skin

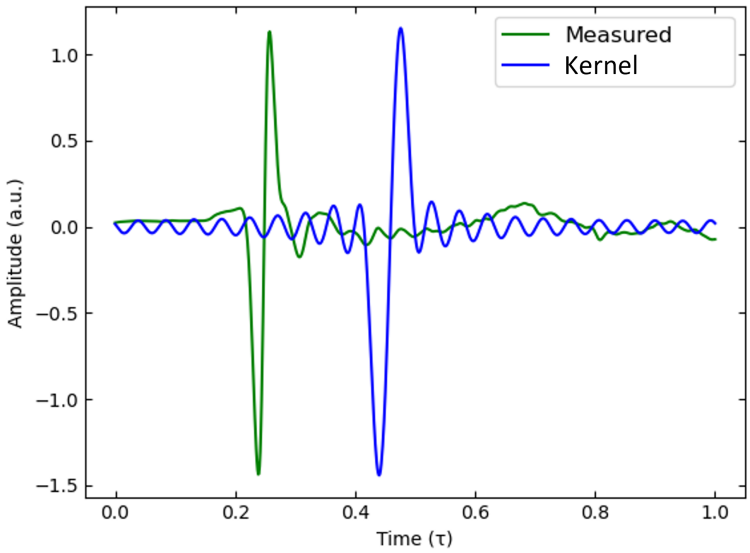

Figure 4.6: In green is the measured reflection off the bottom of the quartz window using our Menlo system in reflection geometry, which was used as our measured reference. In blue is the FRI sampling kernel created to match this reference.

data and thus is the closest representation of a single reflection from the sample data we can obtain. We can compare the difference in the sampling kernels used for the two THz-TDS systems by comparing Figure 4.2 and 4.6. Two key observations are the difference in the amplitudes of the kernel and the presence of side lobes for the Menlo kernel. Fortunately, the presence of these side lobes do not significantly impact the FRI results, whilst still enabling the use of the more suited window presented in Equation 4.16.

By following the procedure outline in Section 3.6, a point measurement of the volar forearm was obtained using the Menlo system in reflection geometry. Expecting a reflection from the bottom of the quartz window and one from the quartz-skin interface, we selected $L = 2$. All other variables were selected to be the same as those stated at the beginning of Section 4.3. Furthermore, as in the previous section the experimentally measured reference was used in a standard least-squares minimization technique as opposed to the Vandermonde system to estimate the amplitudes for the reflections. The experimentally measured reference was also used

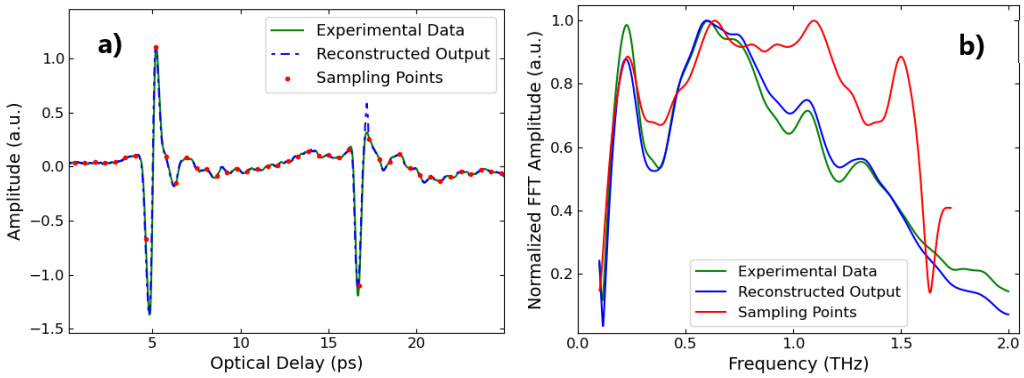

Figure 4.7: Our THz FRI method applied to simple skin data. (a) The measured data is shown by the green line. The sampling points are shown by the red dots. The resulting reconstruction is shown by the dashed blue line. (b) The normalized FFT for the second reflection.

for the signal reconstruction stage.

Figure 4.7 (a) contains the measured THz data in green, acquired by following the above information. The red points indicate the low sampling of this measurement, which was used as the input into our FRI code. Compared to the standard number of data points measured by this Menlo system and as used here in green, a downsampling factor of 25 was used to obtain the low sampling shown in red. This resulted in a time sampling interval of 0.575 ps for the low sampling, increased from the time sampling interval of 0.023 ps in the measured data. By using the time locations and amplitudes for the reflections given by the FRI method, the reconstruction shown by the dashed blue line was obtained. As this reconstruction closely matches the the measured data, the amplitudes and time locations calculated by the FRI method and used in the reconstruction are shown to be accurate. Furthermore, this was all achieved at a very low sampling rate, demonstrating the possibility of low sampling rates for skin measurements. However, there is some difference between the reconstruction and original data for the second reflection. By noting that the match for the first reflection is extremely close, we can deduce that the reference used is largely responsible for the quality of the match. This is as the reference used was an air-quartz reflection, which is the same interface as

for this first reflection in the data presented here. The important reflection is the second one, as it contains the skin information. Therefore, the focus should be on obtaining the best possible match for this reflection. This would be improved by using a reference which more closely resembles the quartz-skin reflection, possibly by using a homogeneous skin phantom to obtain a clean single reflection resembling skin, or by using a model to edit a reference from a metal sheet reflection to be more skin-like.

Figure 4.7 (b) shows the normalized FFT for the second reflection data presented in Figure 4.7 (a). It can be seen that there is a close match between the experimentally measured data and the reconstructed sparse output for the second reflection, which contains the skin information. The sampling points alone have retained very little of the frequency information from the experimental data it was sampled from. This demonstrates that the FRI method can recapture the frequency information despite the sampling points the FRI method used having lost much of this information. As explained in Section 2.3.2, a large amount of important sample information is obtained from the frequency domain, thus these results provide evidence for this method providing accurate sample characterization for skin even at very low sampling rates. As discussed in the previous paragraph, a reference which more closely represents a skin reflection would provide improved results, which would carry over to a closer match in the frequency domain and thus more accurate characterization for the measured skin.

To give an example of important sample information in the frequency domain, the refractive index calculated from the original data and from the FRI reconstruction result is shown in Figure 4.8. This was calculated by using the steps outlined in Section 2.3.2 with the data presented in Figure 4.7. The close agreement between the refractive index calculated from the original data and the reconstruction is further evidence for this THz FRI method providing accurate sample characterization at low sampling rates.

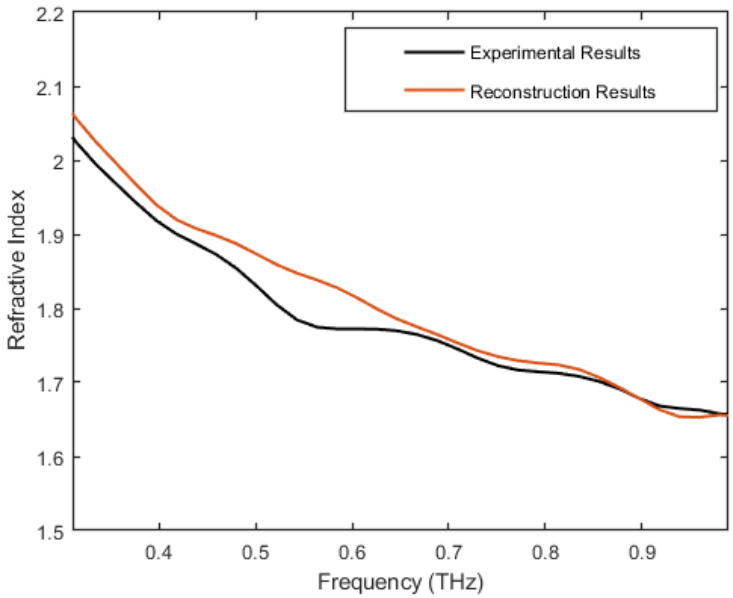

Figure 4.8: The refractive index (a) calculated using the experimental measurement and (b) calculated from the FRI reconstruction.

4.4.3 Adhesive Dressing on Skin

Now that we have established the effectiveness of our THz FRI method for processing skin measurements at a low sampling rate, we will investigate a more interesting case. In this section, we will use measurements from a large sterile adhesive dressing applied to the volar forearm, as shown in Figure 4.9. This dressing consisted of two parts; a central section where the dressing was located and an adhesive section surrounding it for the application to skin. For the measurements and signal processing discussed in this section, the Menlo system and the same sampling kernel described in the previous section were used. A significant difference, however, is that the first reflection from the bottom of the quartz window was cut out of the measurement before it was processed through the FRI code. This was done in order to focus on the region which contained the sample data, which consisted of the quartz-dressing-skin interfaces.

Figure 4.10 contains the point scan data and FRI Dirac results for the dressing section and the adhesive section outlined in Figure 4.9. The measurements were

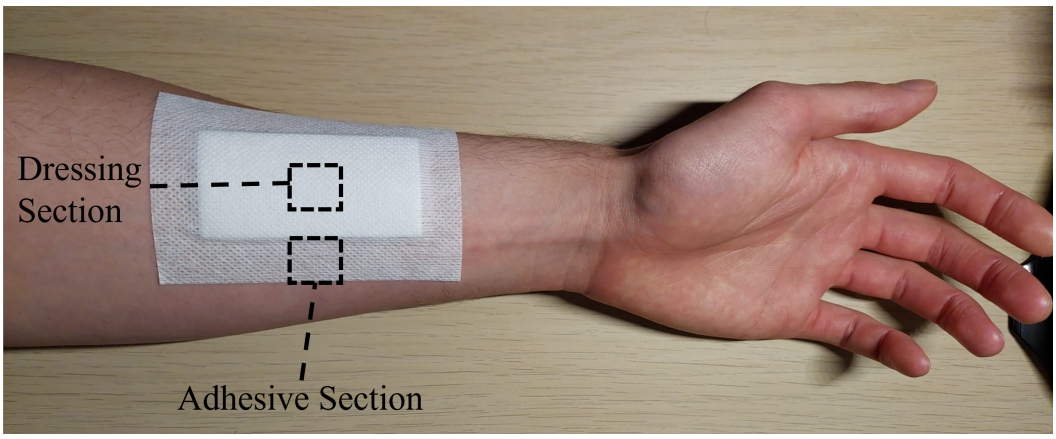

Figure 4.9: A large sterile adhesive dressing applied to the volar forearm.

downsampled by a factor of 20, to give a time sampling interval of 0.46 ps, before it was fed into the FRI code. This data was processed with $L = 2$ and all other variables the same as those previously stated. Note the different optical delay ranges between the figures, with a smaller range used for clarity in (b). The time location of the FRI Dirac shows the time location of the reflection in the measured data. The amplitude of the FRI Dirac informs us of the amplitude of the reflection in the data, relative to the amplitude of the reference reflection. To better present this data, the amplitude of the Diracs have been normalised relative to the first Dirac in (a). The results in Dirac form are being presented here as the work in this section will use the optical delay difference between reflections and the relative amplitudes of the reflections.

By comparing the optical delay difference between the two Diracs in Figure 4.10 (a) and (b) the thickness of the dressing section and the adhesive section can be judged. As the optical delay difference is much larger for the dressing area, at 3.59 ps, compared to the adhesive part, at 0.67 ps, it is indicated that the adhesive section is much thinner, as expected. To obtain a more accurate comparison, the refractive index of both sections were calculated by using the Menlo system in transmission geometry to measure both sections. Having also measured the refractive index of the quartz imaging window, and knowing the beam had a incident angle of 30 degrees

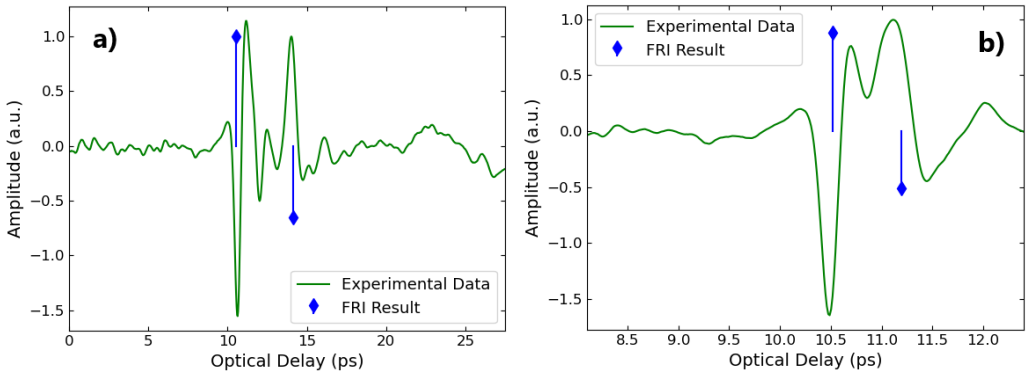

Figure 4.10: The blue Dirac FRI results for the low sampled input, which is shown fully sampled in green. (a) Shows the measurement from the dressing section and (b) shows the enlarged measurement from the adhesive section, both shown in Figure 4.9.

on the bottom of the quartz window, the incident angle to the dressing could be found by using Equation 2.28, which is also illustrated in Figure 2.5. Using this information, the thickness of both sections were calculated to be 0.22 mm and 1.13 mm for the adhesive and dressing sections respectively. This was in agreement with physical measurements made with a micrometer, demonstrating the accuracy of the FRI results for the time location of the reflections even at low sampling.

To evaluate the accuracy of the amplitudes calculated by the FRI method, a more interesting comparison of the dressing-skin reflection from skin with an antiseptic cream applied and without it applied is presented in Figure 4.11. As explained in Section 1.2.1, THz is very sensitive to water levels and can be used to monitor hydration levels in skin. As the antiseptic cream increases the skins hydration level, THz could be used to monitor the presence and quantity of the cream remaining beneath the dressing or bandage without needing to remove it. In terms of the results presented here, the amplitude of the FRI result for the dressing-skin reflection can be used as a measure for how much antiseptic cream is present, as compared to a measurement without cream present. For example, the second reflection in Figure 4.11 (a), where the cream and dressing were applied then immediately measured, is 33% lower than in Figure 4.11 (b) where the dressing

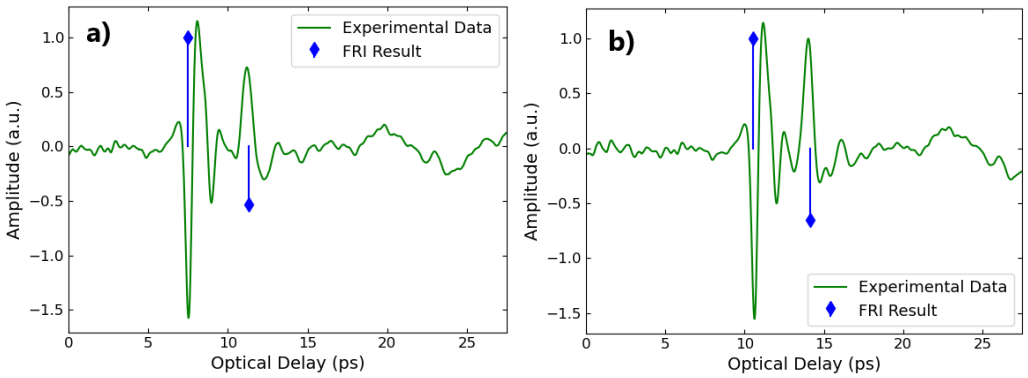

Figure 4.11: The blue Dirac FRI results for the low sampled input, which is shown fully sampled in green. The measurements are for the dressing section with (a) antiseptic cream applied and (b) without the cream applied.

was applied and then measured without any cream being present. This decrease in amplitude indicates an increase in hydration of the skin. For verification of these results, we can compare them to the peak-to-peak change in the fully sampled data, found to be a 31% decrease for the same reflections. Furthermore, a slight increase in the optical delay difference between the peaks was observed for when the cream was applied. This was most likely due to the dressing absorbing some of the cream and increasing in thickness slightly. These results demonstrate that this method could be applied to other cases to monitor a factor which changes the hydration of skin, even beneath layers such as dressings and using a low sampling rate for data acquisition.

The key significance of these results is that they were obtained from a low sampling rate, where the sampling rate may be too low to accurately extract reflection locations and amplitudes without further processing, such as using the FRI method. The sampling points used in the FRI code for processing the data shown in Figure 4.11 (b) is presented in Figure 4.12, along with the original fully sampled measurement. By comparing the low sampling to the original full sampling, we can see that the amplitude and time locations will not be extracted accurately by using the low sampling data alone. For example, using the undersampled data to extract

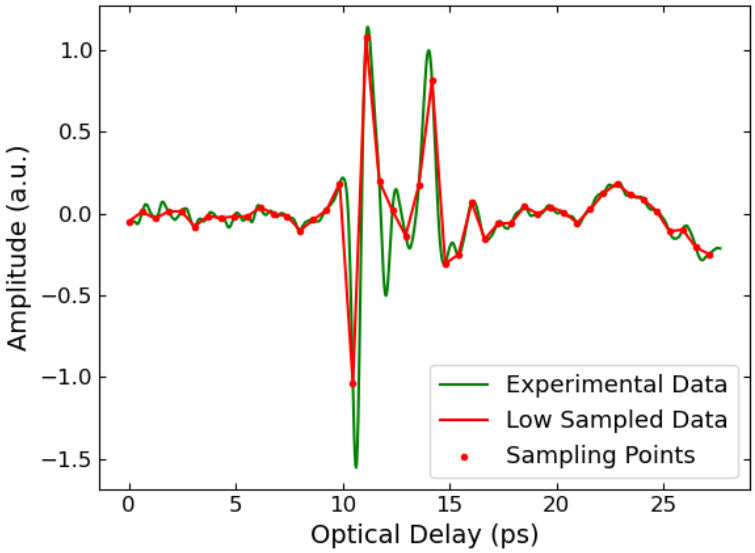

Figure 4.12: An example of the sampling points used for the experimental data presented in this section, using an undersampling factor of 20. This experimental data is the same as shown in Figure 4.11 (b).

the percentage difference discussed in the previous paragraph results in a decrease of only 19%, as compared to the 31% decrease found from the fully sampled data. However, as shown in the previous paragraph, the FRI results were able to extract a percentage difference in agreement with that found in the fully sampled data. Therefore, the THz FRI method enables the fast acquisition of data by measuring at lower sampling rates whilst providing accurate results.

4.5 Discussion

In this chapter it was found that the THz FRI method introduced produces accurate results at relatively low sampling rates, whilst retaining both time domain and frequency domain information. The unlocking of this low sampling is the primary benefit of this method, which is especially attractive in applications where the sample has a time dependency or other applications where quicker data acquisition would be of large benefit. For instance, during *in vivo* experiments with human skin, such as those contained within this thesis, patients are required to remain very still

during the data acquisition. The shorter this period, the less likely a patient is to accidentally shift, causing an effect on the measured data. It also makes the measurements quicker and easier for the patients, which could be especially relevant for application to injured or sick patients. Furthermore, a shorter time period would help to minimise the effect of occlusion to the skin by the imaging window which would, for example, enable averaging over a greater number of consecutive pulses.

As described in Section 1.1.2, typical THz-TDS systems use an optical delay line to excite the detector at different THz signal time steps. Thus, the steps along the time delay line constitute the sampling points and are which the FRI method seeks to minimize. This opens up the possibility of an optical delay stage with less precision and accuracy, which could be designed to be less expensive and more compact. In addition to the standard measurement systems, this method could see use in THz single-pixel spectroscopic imaging methods [100] by allowing for lower sampling on the temporal waveform measured per pixel. These methods can achieve high quality hyperspectral imaging much faster than current commercial systems, which could be amplified by combination with FRI methods.

The aim of this chapter was to introduce a method enabling low sampling rates whilst maintaining similar experimental methodology and required foreknowledge of the sample. This has mostly been achieved, however this method does require an input of the number of reflections it will search for. This requires either some foreknowledge of the structure of the sample, or trial and error with trying a sensible range of reflections. The other challenging aspect of this method is creating a suitable sampling kernel. As this is based from the reference measurement, which is standard procedure in most THz measurements, this has not added to experimental methodology. However, it does add a small amount of work to tailor the sampling kernel to the THz pulse shape used. So long as this pulse shape does not change significantly, it was found that the sampling kernel could remain the same.

The performance of the FRI method could be enhanced significantly by fur-

ther work on obtaining sampling kernels which more closely resemble the sample reflections. This could be achieved by measuring an isolated single reflection, to use as a reference, from a material which has a refractive index closer to that of the sample or by using a model to adjust a metal mirror reference to a pulse shape expected from the sample. Furthermore, a more versatile sampling kernel which accounts for the THz pulse shape changing during propagation through dispersive samples and reflection off different material boundaries could be developed. Additionally, it is possible that more information than just the amplitude and time locations of the reflections can be extracted using the SoS information. As this method has performed very strongly for extracting correct information at low sampling rates in both simulation and experimentation, we believe that further research into creating a better sampling kernel and extracting more information from the SoS form is of great interest.

4.6 Summary

A THz specific FRI method to achieve low sampling rates was introduced and mathematically described, including the construction of a THz like sampling kernel and the extraction of the time locations and amplitudes for reflections. This method was verified with simulated data, by comparing the results with the known values used to simulate the data, and with simple experimental data, by comparing the time domain and frequency domain reconstructions using the FRI results to the fully sampled measured data. By applying this method to measurements of skin with a dressing applied, it was found that the hydrating effect of antiseptic cream on the skin could be detected accurately at low sampling rates. It was proposed that this FRI method could be used to monitor how much cream is present, or other factors which hydrate the skin, beneath a layer such as a dressing, all at fast measurement speeds.

Chapter 5

THz Sparse Deconvolution to Monitor the Effect of Transdermal Drug Delivery Patches on Skin

5.1 Introduction

In this chapter a THz sparse deconvolution and reconstruction method is explained, with the aim of applying this method to samples containing overlapping reflections in order to separate them out and extract useful information. Though the FRI method introduced in the previous chapter enabled the use of fast measurements with the low sampling rate it provided, it struggled to separate overlapping reflections. Therefore, this sparse method is introduced as a tool to extract more sample information for such situations. As an example of the efficacy of this method, it will be applied to study the skin beneath transdermal drug delivery (TDD) patches in both a 2-hour and 24-hour study. It was found that the patches lead to an increase in hydration

of the skin, the extent of which heavily depended on the backing material of the patch. The sparse reconstruction result was verified by a comparison to similar results obtained through standard methods using data taken from the same study. Furthermore, an image of a patch applied to the arm was taken, with the sparse method effectively imaging the skin beneath the patch. Herein it is shown that the THz sparse reconstruction method has great potential for monitoring skin beneath layers such as TDD patches or medical bandages.

5.1.1 Sparse Deconvolution

The reflected signals off different layers or "echoes" for THz-TDS in reflection geometry can partially or totally overlap, especially in the case of samples with thin thickness or layers, requiring deconvolution to accurately resolve these overlapping reflections and extract relevant sample information. Crucially, these signals have a sparse representation due to the limited number of echoes containing all the significant information, and so only a limited number of data points have non-zero values when ignoring noise. The sparse constraint can be applied to such signals, allowing sparse deconvolution to be utilized to retrieve the impulse-response function via an inverse problem where detection and estimation of the signal are performed jointly.

Sparse deconvolution has been shown to perform extremely well in many areas. Gholami *et al.* used a fast and automatic sparse deconvolution method to retrieve reflectivity series from seismic data with the presence of additive noise [101]. Their results demonstrated significant stability against outliers in the data and in numerical experiments they were able to automatically generate solutions with only a few iterations needless of any prior knowledge on the noise. To improve the resolution of live-cell super-resolution fluorescence microscopy, Zhao *et al.* took advantage of prior knowledge on the biological structures being studied to use in a sparse deconvolution method [102]. They were able to achieve an almost twofold increase in resolution and also applied their method to increase the resolution in three-dimensional

structured illumination microscopy. In THz-TDS, a research group lead by Citrin has met much success with their sparse deconvolution method [103]. They were able to extract a detailed three-dimensional mapping of the layer structure for a historical easel painting in a nondestructive manner, discovering a previously unidentified restoration of the varnish [19]. Additionally, they characterised subsurface damage in woven carbon fiber-reinforced composites, extracting and visualising many fine details of different subsurface damage types and confirmed their results with a comparison to X-ray tomography [104].

5.1.2 Transdermal Drug Delivery

Since most polymers and other packaging materials have a low water content, THz light is able to see through them and has demonstrated potential in security applications [105]. Similarly, TDD patches are typically made from lightweight fabric/polymer and THz light is able to pass through them with minimal attenuation. In this study, we exploit the sensitivity of THz light to water along with its ability to see through TDD patch materials to probe skin hydration whilst the patch is still being worn. The high attenuation by the skin requires reflection geometry to be used for such measurements as the penetration depth into living tissues is limited and thus we need to use sparse deconvolution to separate out the reflections from the patch and the skin.

The benefit of high sensitivity to water content that THz light has is especially relevant to TDD through medical patches, as skin hydration can be closely linked to the efficacy of drug delivery [106]. TDD is being used for an increasing number of applications, varying from localized pain relief [107] to controlling the symptoms of Parkinson's disease [108]. This approach to drug delivery is being used as it can avoid issues with other delivery methods, such as potential side effects from the liver or gastrointestinal tract metabolizing the drug or the use of needle injections. Additionally, this simple delivery method is easy for care workers

to follow, in the case of patients lacking the ability to take treatments themselves. A further benefit is a greater degree of control over the drug release for the whole time period of drug treatment maintaining the requited therapeutic dose [109]. The functionality of TDD patches can be greatly affected by the design of the patch. By changing the backing material of the patch, the occlusive property of the patch can be controlled to some extent. In cases where the drug is potentially toxic to the wrong person which can occur via transfer, for example, a fully occlusive backing material can be used to ensure no leakage of the drug. Furthermore, by preventing any drug leakage the dosage can lead to better control giving a more effective treatment. However, it has been found that highly occlusive backing materials can lead to skin irritation due to the buildup of water [110]. Thus, less occlusive backing materials can be preferable when the drug treatment allows for it. The adhesive material used for the TDD patch can affect how securely the patch will remain in place, the drug load possible and ease of patch removal [111].

5.2 Theory

For THz-TDS in reflection geometry, the incident THz pulse *i(t)* is convoluted with the impulse-response function *h(t)* to give the measured THz reflected signal *y(t)*:

$$y(t) = i(t) \otimes h(t) = \int_{-\infty}^{+\infty} i(\tau)h(t-\tau)d\tau. \tag{5.1}$$

This is in the same form as the one obtained by treating THz-TDS as a LTI system, as demonstrated in Section 2.3.3. Sample information, such as the structure and properties, are contained within the impulse-response function. In practice, the discrete version of Equation 5.1 is experimentally obtained, given by:

$$y_n = \sum_{m=0}^{M-1} i_m h_{n-m} + e_n. \tag{5.2}$$

Here, $y_n = y(nT_s)$, $i_m = i(mT_s)$, T_s is the sampling period, n and m are the indices of data points, M is the length of the data set and e_n accounts for the noise in the measurement due to the measurement system and materials. By letting column vectors $\mathbf{y}$, $\mathbf{i}$, $\mathbf{h}$ and $\mathbf{e}$ collect y_n, i_n, h_n and e_n respectively then Equation 5.2 becomes:

$$\mathbf{y} = \mathbf{A}\mathbf{h} + \mathbf{e}, \tag{5.3}$$

where $\mathbf{A}$ is the square Toeplitz matrix where delayed versions of $\mathbf{i}$ make up its columns [112]. Each consecutive column has $\mathbf{i}$ delayed by a further one element, until the whole of $\mathbf{i}$ has been cycled through and a square matrix has resulted. By presenting $\mathbf{A}$ in matrix form, this can be more intuitively understood:

$$\mathbf{A} = \begin{bmatrix} i_0 & i_{M-1} & i_{M-2} & i_{M-3} & \dots & i_1 \\ i_1 & i_0 & i_{M-1} & i_{M-2} & \dots & i_2 \\ i_2 & i_1 & i_0 & i_{M-1} & \dots & i_3 \\ i_3 & i_2 & i_1 & i_0 & \dots & i_4 \\ \vdots & \vdots & \vdots & \vdots & \ddots & \vdots \\ i_{M-1} & i_{M-2} & i_{M-3} & i_{M-4} & \dots & i_0 \end{bmatrix}. \tag{5.4}$$

The key focus of sparse deconvolution is obtaining the solution for the following l_0 regularized optimization problem, which exploits the sparse constraint by approximating $\mathbf{y}$ with $\mathbf{A}\mathbf{h}$, where $\mathbf{h}$ crucially is a sparse sequence. Being a sparse sequence demands that $\mathbf{h}$ only has few non-zero elements. The l_0 regularized optimization problem is defined by:

$$\min_{\mathbf{h}} \frac{1}{2} \parallel \mathbf{A}\mathbf{h} - \mathbf{y} \parallel_2^2 + \lambda \parallel \mathbf{h} \parallel_0, \tag{5.5}$$

where $\parallel \ \parallel_2$ and $\parallel \ \parallel_0$ represents the l_2-norm and l_0-norm respectively. Here, λ is the sparsity factor chosen to select the trade off between the sparsity of $\mathbf{h}$ and the residue norm. The higher this sparsity factor is set, the more sparse the resulting

h will be, and so the smaller the second term will be. The first term represents the distance between the approximation **Ah** and actual measured reflected THz signal **y**. However, the solution to this problem is known to be non-deterministic polynomial-time hard in general [113] and it has been shown that an approximation using the l_1-norm in place of the l_0-norm performs well whilst guaranteeing a global optimum, unlike when using the l_0-norm [114]. Now, by using the l_1-norm for **h** instead, $\| \mathbf{h} \|_1$, Equation 5.5 becomes:

$$\min_{\mathbf{h}} \frac{1}{2} \| \mathbf{Ah} - \mathbf{y} \|_2^2 + \lambda \| \mathbf{h} \|_1 . \tag{5.6}$$

To solve the problem presented in Equation 5.6 an iterative shrinkage algorithm will be employed, where soft-thresholding is applied to the result of a vector multiplication for each iteration:

$$\mathbf{h}_{i+1} = S_{\lambda\tau}(\mathbf{h}_i - \tau \mathbf{A}^{\mathrm{T}}(\mathbf{Ah}_i - \mathbf{y})), \tag{5.7}$$

where τ is a suitable step size, constrained by:

$$\tau < \frac{2}{\| \mathbf{A}^{\mathrm{T}}\mathbf{A} \|_2}, \tag{5.8}$$

in order to ensure convergence. The soft-thresholding component is contained within the operator $S_{\lambda\tau}$:

$$S_{\lambda\tau}(h[n]) = \begin{cases} h[n] + \lambda\tau & h[n] \leq -\lambda\tau \\ 0 & | h[n] | < \lambda\tau \\ h[n] - \lambda\tau & h[n] \geq \lambda\tau \end{cases} . \tag{5.9}$$

The result of the iterative shrinkage algorithm gives the output for sparse deconvolution, that being **h**.

Now that the sparse result contained in $\mathbf{h}$ has been obtained, this can be used to reconstruct the individual reflections within the reflected signal $\mathbf{y}$. Typically, this sparse result consists of separate small clusters of points to represent each reflection contained within the reflected signal. The points corresponding to the reflection of interest can easily be isolated. By aligning and scaling multiple incident THz pulses with the chosen reflection points' temporal locations and amplitudes respectively, a recreation of the reflection of interest can be created. The peak-to-peak of this reflection can then be measured by combining the magnitude of the most positive and most negative points in the reflection.

For the results contained within this chapter, the incident THz pulse was obtained via measuring the reflection off an optically thick piece of quartz and multiplying by -1 for phase correction. A sparsity factor $\lambda = 3.5$ was chosen, as this gave the best results whilst not over-aggressively soft-thresholding for the data sets we were using. A step size $\tau = 1.2/ \parallel \mathbf{A}^{\mathrm{T}}\mathbf{A} \parallel_2$ was selected as a trade-off between run-time and accuracy whilst abiding by the constraint stated in Equation 5.8. The iteration outlined in Equation 5.9 was repeated 2000 times for each result, chosen for the same reasons as the step size.

5.3 Samples and Experiment

The protocol described in Section 3.6 was adhered to for the *in vivo* measurements taken for this chapter. Ethical approval was obtained for this study from the Biomedical Scientific Research Ethics Committee, BSREC, (REGO-2018-2273 AM03). Written informed consent was obtained from each volunteer prior to their involvement in the study. The Menlo system, detailed in Section 2.4.2, was used for the acquisition of the measurements. A demonstration of this system taking an *in vivo* skin measurement is shown in Figure 5.1, with an annotated photograph of the system mid measurement on the left and a schematic of the THz reflections

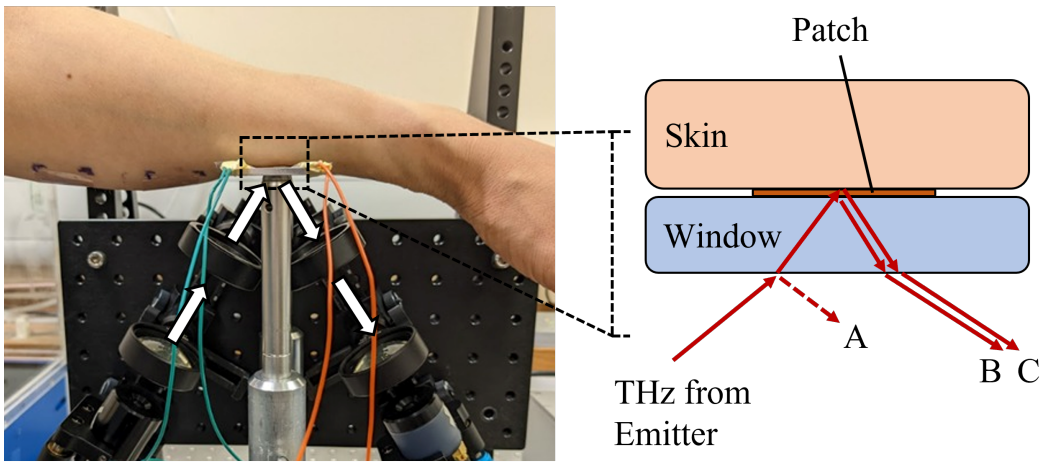

Figure 5.1: A Menlo Systems Tera K15 fibre-coupled THz-TDS set up in reflection geometry to measure an arm with TDD patches applied with a schematic of the highlighted region.

through the window-patch-skin system on the right. Before volunteer measurements began, a reference measurement was taken by setting a thick piece of quartz at the sample recording position. This was measured each day to account for any daily variations in the THz signal produced by the system. An example of a reference pulse used in this chapter is shown in Figure 5.2. A quartz reflection was used as the reference since a quartz imaging window was used for the measurements taken on volunteers. Further, sparse deconvolution performs best when the reference used closely resembles the shape of sample reflections, thus a quartz reference is the closest reference obtainable. For the sample measurements, the volunteers placed their volar forearm atop of the quartz window for 1 minute to acquire approximately 280 reflected THz pulses from a single point on their skin for each region of interest. To ensure a consistent contact of skin with the quartz imaging window, as to avoid the occurrence of air gaps between the two for example, pressure sensors were used as described in Section 3.6.

TDD patches with two types of backing materials and with different excipient percentages were placed on both volar forearms of the volunteers, as demonstrated in Figure 5.3. The patches placed on the left volar forearm were the oc-

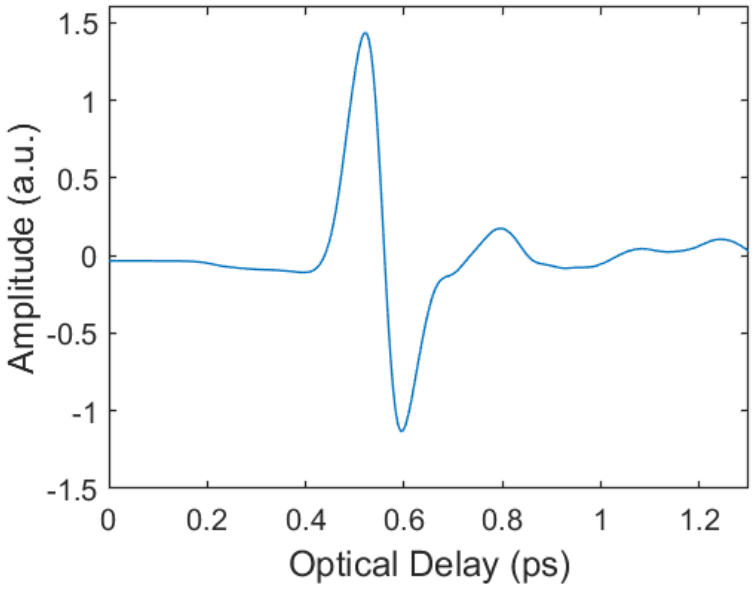

Figure 5.2: An example of a THz reference signal used in the sparse deconvolution of measured THz reflected signals. This reference was obtained by measuring the reflection off a thick piece of quartz placed at the sample measuring location.

clusive poly(ethylene terephthalate) film backed ones, whilst the partially occlusive polyester fiber woven backed patches were placed on the right volar forearm. The excipients in TDD patches, serving as vehicles for drugs which could be contained in the patches, boost the drug delivery rate. To analyze if different percentages of these excipients have an effect on the skin's hydration levels, three patches, each with a different excipient concentration (0%, 3% and 6%), were placed on each arm. In addition to the patches, a region of skin on both volar forearms was designated as a control region to be measured and left untreated to account for a person's natural temporal variation of their skin hydration. These 4 regions on each arm constituted the regions of interest to be measured. In this experiment the excipient in use was propylene glycol (CH3CH(OH)CH2OH) [115] and the aforementioned excipient concentrations were chosen as these are commonly found in commercial TDD patches. The adhesive material used for the patches was a proprietary polyurea cross-linked thermoset, with 10% Transcutol present [111]. These non-active patches were manufactured by Medherant Ltd. No other drugs were present in the patches to isolate

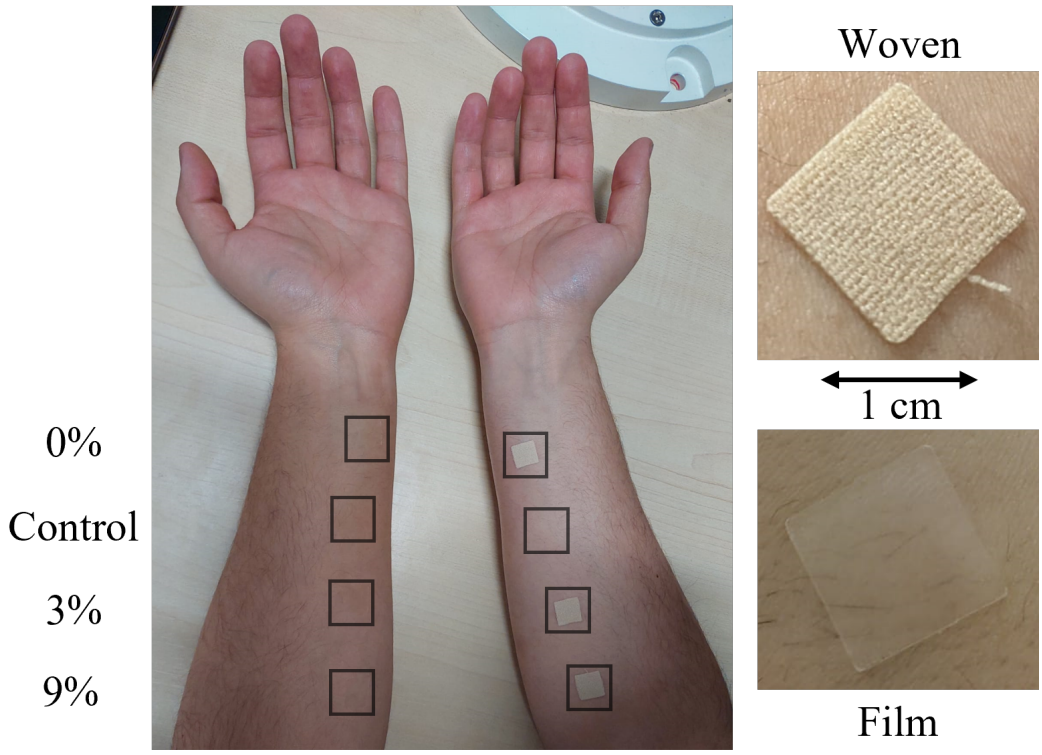

Figure 5.3: A photo with boxes to highlight skin locations for where the patches and control areas typically were. Film patches are applied to the left arm and woven patches to the right arm. Close-up photos of each patch type shown to the right.

any changes on the skin as a consequence of the patches backing material and excipient.

The skin on the volunteer's volar forearm was measured before applying the TDD patches. Once the patches were applied, the area of interest was placed onto the imaging window and the skin was measured through the patches. During each set of measurements, the untreated control region was also measured for both arms. For the 2-hour experiment the measurements were taken with the patches on the volar forearm, i.e. through the patches, at 0 minutes, 30 minutes and 2 hours after the patches were applied for 8 volunteers. For the 24-hour experiment measurements on 14 volunteers were taken immediately following patch application and then 24 hours later with both the patches still applied and then shortly after removing them. By conducting these two experiments with measurements at various time

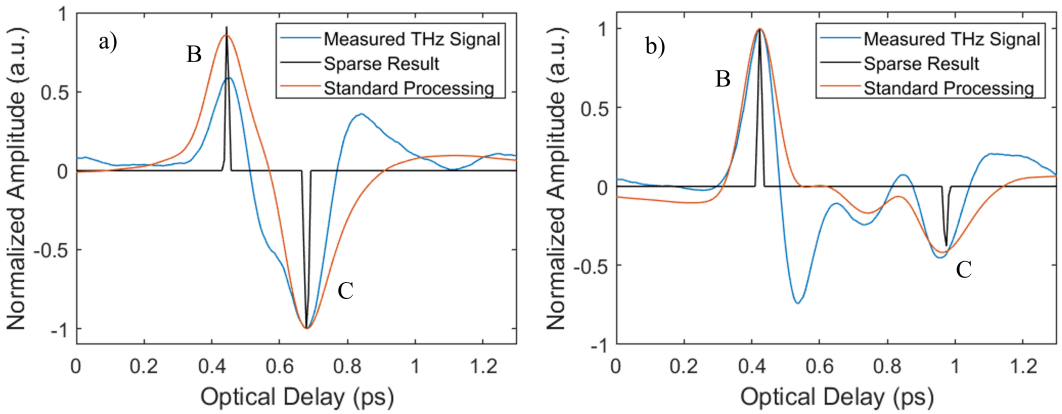

Figure 5.4: The measured reflected THz signals, the deconvolution results from sparse deconvolution and a standard THz processing method result for a) the film backed patch and b) the woven backed patch, both with 0% propylene glycol. The peak labels correspond with those schematically shown in Figure 5.1.

intervals both the short- and long-term effects on skin of the TDD patches and the excipients contained within them can be examined. As the 24-hour experiment has measurements shortly before patch application and shortly following patch removal, these patchless measurements can be used to verify our sparse reconstruction method applied to the paired patch measurements. Before the start of each measurement the subjects acclimatized for a period of 20 minutes, as detailed in Section 3.6.

5.4 Results

5.4.1 Patch Characterization

Firstly, THz reflection data for the patches alone will be presented, as to characterize their THz response and demonstrate the sparse deconvolution results. Both a film and woven patch of 0% excipient were placed directly onto the quartz imaging window and measured using the same system as described in the previous section. Figure 5.4 a) contains the measured THz data, $\mathbf{y}$, for a single point scan through the center of the film patch, in reflection geometry. This means that the first reflection corresponds to the quartz-patch interface and the second reflection corresponds to

the patch-skin interface, as schematically represented in Figure 5.1. The sparse deconvolution result, **h**, is also shown. Lastly, the results from using a standard THz processing method described in Section 2.3.2 are also presented. Figure 5.4 b) shows the same measurements but for the woven patch. The sparse result tracks the center of the first peak of the THz reflection. A clear difference between the optical thickness of the two patches can be observed, due to the optical delay being much larger between the two surface reflections for the woven patch. For the film patch, there is a clear overlap between its bottom and top surface reflections. This overlap results in interference, destructive for the first reflection but constructive for the second reflection, due to the incident THz pulse shape (as shown in Figure 5.2) and the resulting phase shift. The sparse deconvolution result is able to account for this overlap and interference, recovering the temporal location and relative amplitude associated with the overlapping reflections. For the purposes of this chapter, the sparse reconstruction method presented can recover useful sample information in such overlaps. It can also be noticed that the second reflection from the woven backed patch is significantly smaller than the second reflection from the film patch. As the woven patch is thicker, the reflection has become more attenuated during this increased travel time. Additionally, the woven patches have a refractive index closer to that of skin than the film patches did, thus a relatively smaller reflection from the patch-skin boundary for the woven patches resulted.

5.4.2 24-Hour Study and Sparse Reconstruction Verification

Figure 5.5 a) shows the average NRC, introduced in Section 3.7 and defined in Equation 3.2, for the peak-to-peak of the reconstructed skin reflection for 14 volunteers. This reconstruction was made using the sparse result of *in vivo* skin measurements with a TDD patch applied, with these measurements containing the reflections highlighted in the schematic shown in Figure 5.1. Then, following the steps outlined in Section 5.2, the reconstruction and the peak-to-peak measurement for the patch-

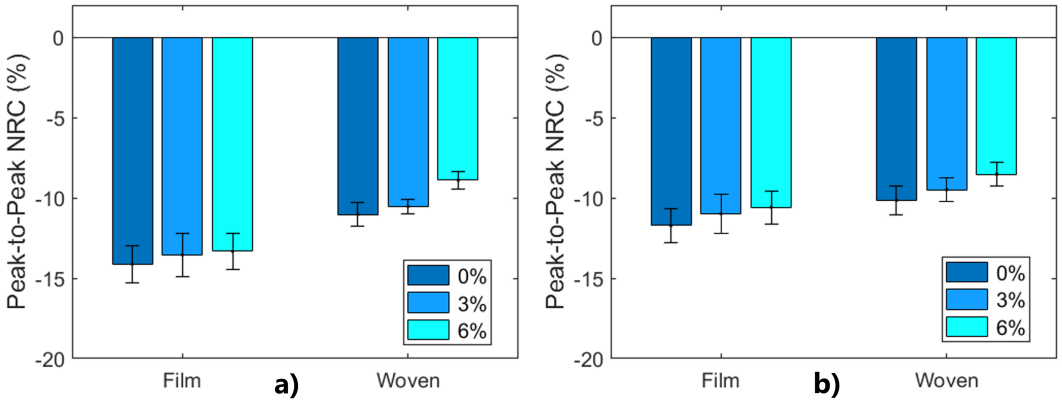

Figure 5.5: The average peak-to-peak normalized relative change in skin over a 24-hour period for 14 volunteers with a) transdermal drug delivery patches applied and b) the same location but with patches removed. The color indicates differing excipient levels of 0%, 3% and 6% propylene glycol. Data for film backed patches is located on the left side of the figures, with woven backed data on the right. Error bars are the standard error on the mean.

skin reflection were obtained. The first data set was taken shortly following patch application and the second 24 hours after application. For both patch types and each excipient percentage, the NRC can be obtained by using the reconstruction from these patch measurements together with the control measurements taken at the same times, following the procedure outlined in Section 5.3. Measurements taken with the film and woven backed patches are shown on the left and right sections of the figure respectively, with the color indicating excipient level. The error bars indicate the standard error of the mean.

All results presented in Figure 5.5 a) demonstrate a significant decrease in peak-to-peak NRC, which is linked to an increase in hydration level [34]. This signifies that the patches have led to water collecting in the skin beneath them due to the aforementioned occlusion effect. As the decrease in the woven patch data is less severe, it can be determined that these patches are more breathable. This demonstrates the ability of this method to discern the occlusive characteristics of various medical patches and bandages. Furthermore, a slight trend in decreasing magnitude of the peak-to-peak NRC as excipient level increases can be observed,

indicating a decrease in skin hydration with higher excipient level. However, this trend is mostly within the errors of each individual result, demonstrating the need for further measurements to ascertain this relationship. Regardless, this highlights the potential of this method for monitoring the effects of transdermal drugs on skin hydration beneath patches or bandages. The errors for the woven patches are smaller than those for the film patches. As shown earlier in this section, the woven patches were thicker which resulted in a larger optical separation between the quartz-patch and patch-skin reflection. Thus, the sparse deconvolution could perform more accurately and consistently, resulting in a smaller error.

Figure 5.5 b) contains data taken as a verification for our sparse reconstruction method. The procedure is very similar to that used above, however the measurements were taken shortly before patch application and immediately after the patches were removed after 24 hours of them being applied. This meant that the skin could be directly measured, without the need of any sparse deconvolution and reconstruction to obtain and separate the skin data from under the patch. Therefore, these similar direct skin measurements can be compared to those obtained via our sparse reconstruction method in order to judge this methods performance.

By comparing Figure 5.5 a) and b) it can be seen that a significant reduction in the NRC for the peak-to-peaks are obtained in both data sets, but the measurements taken with the patches remaining applied show a noticeably larger reduction. Furthermore, in the skin only measurements shown in Figure 5.5 b) there is no longer a clear significant difference between the patch types. An explanation for both of these differences is the nature of removing the patches before the 24-hour measurements allows some time for the skin to breath and become less hydrated, resulting in a smaller peak-to-peak NRC. Additionally, as the skin under the film patches was initially more hydrated it would dehydrate to a normal state at a faster rate than the skin under the woven patches, proceeding to a less obvious difference between them. This distinction between the types of patches reveals the benefit of

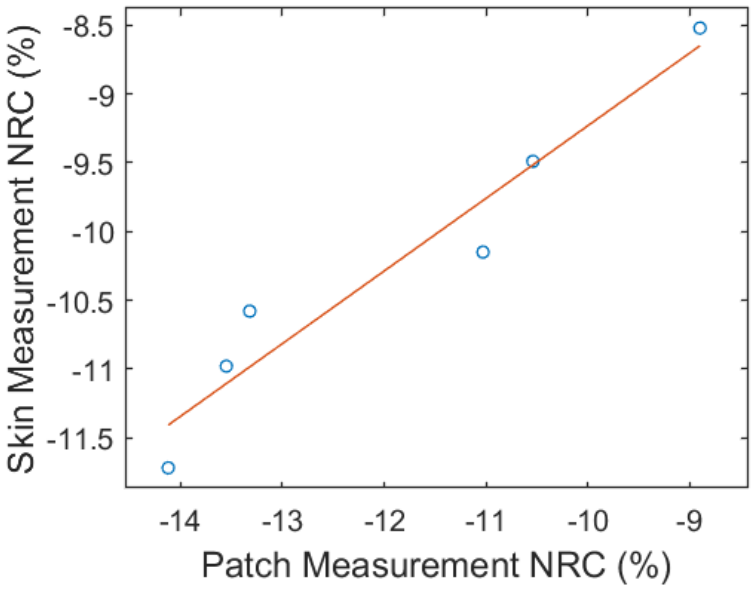

Figure 5.6: A demonstration of the correlation between the NRC in measurements through the patch and of the bare skin presented in Figure 5.5. The orange line shows the line of best fit, with a correlation coefficient of $r = 0.97$

monitoring the skin whilst the patch is still applied, which our sparse reconstruction method allows. Furthermore, we expect that the NRC in the peak-to-peak to be more accurate following the sparse method, as the skin hydration can be monitored without patch removal, and consequently without time for the skin to dehydrate.

To demonstrate the correlation between the NRC for the peak-to-peaks contained in Figure 5.5 a) and b) we have plotted them against each other as shown in Figure 5.6 and calculated the Pearson correlation coefficient from the line of best fit for these results. With the coefficient being 0.97, it demonstrates the strong correlation between the results with the patch on and with only skin, providing evidence to the accuracy of our sparse reconstruction method used for the data with the patch applied.

5.4.3 2-Hour Study

A further experiment was conducted for investigating the shorter-term response of skin to the patches, collecting data from 8 volunteers. This time, measurements

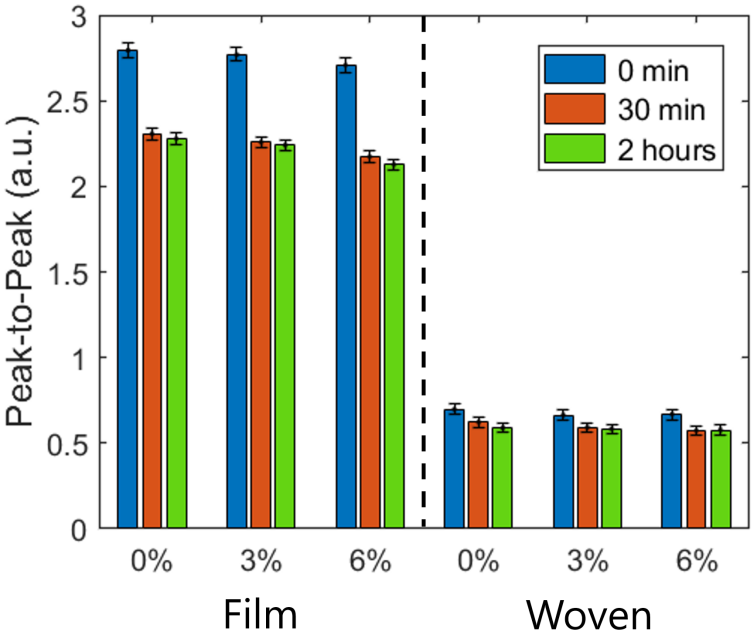

Figure 5.7: The average peak-to-peak observed in 8 volunteers at 0 minutes, 30 minutes and 2 hours following the application of transdermal drug delivery patches. The patches consisted of film backed and woven backed types, with different excipient levels of 0%, 3% and 6% propylene glycol. The error bars are the standard error on the mean.

were taken immediately following patch application, 30 minutes after and finally 2 hours after application. All measurements were taken through the patch and reconstructed using our sparse method. Results from these measurements can be seen in Figure 5.7, where the left section contains the film results and the right contains woven ones. This time, the color of the bars signifies the measurement time following patch application with the excipient level changing for each cluster of bars and is denoted on the x-axis. Unlike in the previous data presented, here we do not use the average NRC in the peak-to-peak, but the average raw peak-to-peak itself. This is as the experiment was conducted over a shorter time period, only 2 hours, and volunteers remained in consistent laboratory room conditions during which other factors that affect the skin were controlled. The error bars indicate the standard error of the mean.

A clear trend of the measurements taken immediately after patch application

being higher than for the same patch type and excipient level can be observed in Figure 5.7. As explained previously, a higher peak-to-peak indicates less hydrated skin comparatively. Thus, in all cases there is a significant increase in hydration after the patch has been applied for 30 minutes. This hydrating effect drops off between the 30 minute and 2-hour measurements, as there is only a small decrease in peak-to-peak which is generally within the error of these results. Therefore, by considering the 24-hour results too, we can conclude that the majority of the hydrating effect of the patches occurs within the first 30 minutes of their application and lasts for at least 24 hours, if the patch remains on the skin. A very big difference between the average peak-to-peak results for the film backed patches and the woven backed patches can be seen. As explored in Section 5.4.1, the THz measurements for these patches look very different. Specifically, a larger optical delay and smaller amplitude for the woven patch reflection as compared to the film patch. This smaller reflection amplitude causes the sparse reconstruction for this reflection to also have a lower peak-to-peak. However, this does not signify that the skin under the woven patch is less hydrated than the skin beneath the film patch but highlights that the hydration information is contained within how this amplitude changes over time. By observing how the average peak-to-peak decreases for the woven data sets compared to the film sets, we can see that there is a greater relative decrease in the film data. Thus, these results agree with the film patches being more occlusive and so having a greater hydrating effect, as found in the 24-hour data.

5.4.4 Patch Imaging

Though much information can be obtained from point measurements, as shown throughout this thesis, some important features can only be extracted via imaging measurements. For example, this would be necessary to map an area of diseased tissue or to monitor a wound healing beneath a medical dressing. To explore the potential for this sparse method to be used in such situations, a film backed TDD

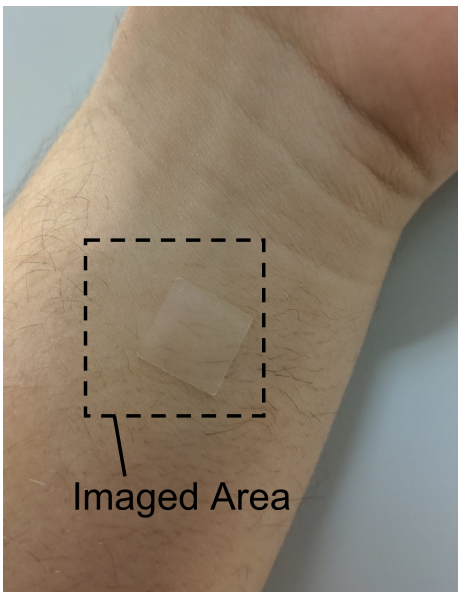

Figure 5.8: The marked region highlights the area of the arm imaged, which includes a film backed patch applied to the skin. This region is 21 mm by 21 mm in size.

patch and the surrounding skin was imaged, with Figure 5.8 highlighting the imaged region. The image was taken 2 minutes after the patch was applied to the arm, and the measurement took around 5 minutes to complete. Other than the much longer measurement time, the same measurement procedure was followed as for the point measurements taken for this chapter. A total of 441 point measurements were taken to form the 21 by 21 measured image, using a step size of 1 mm.

The measured image was processed in two different ways, one to obtain the processed waveform peak-to-peaks, as shown in Figure 5.9 a), and the other to extract the peak-to-peaks of the reconstruction from the sparse deconvolution method, as shown in Figure 5.9 b). In both figures the patch region can clearly be distinguished from the surrounding skin due to the relatively higher peak-to-peak in the patch area. However, there is a key difference in the information being presented. In Figure 5.9 a) the patch area contains the peak-to-peak of both the quartz-patch and patch-skin reflections, as these reflections are overlapping, and the rest of the image contains the quartz-skin reflection where the patch is not present. Contrary

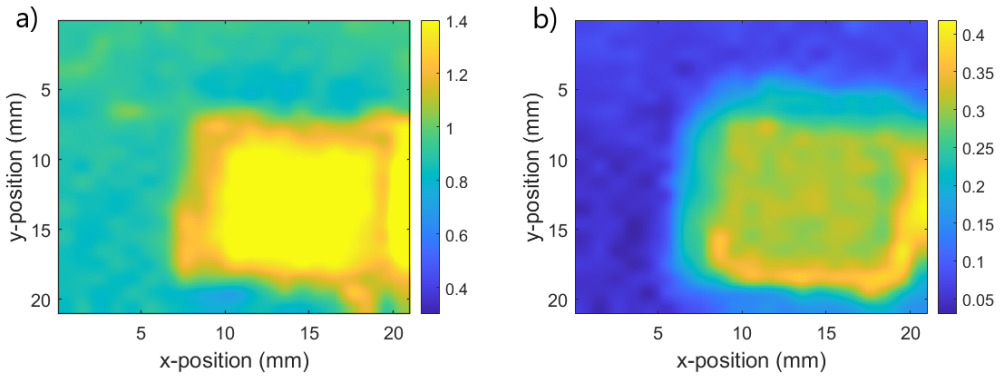

Figure 5.9: THz peak-to-peak images of a film patch applied to the skin, the imaged region is shown in Figure 5.8. a) The processed waveform results for the patch and surrounding skin. b) The sparse reconstruction results for the second reflection, corresponding to the skin underneath the patch.

to this, Figure 5.9 b) contains only the peak-to-peak for the sparse reconstruction of the second reflection. As there is only one reflection where the patch is not present, the quartz-skin reflection, the peak-to-peak is near zero here. As for where the patch is present, the peak-to-peak corresponds to the patch-skin reflection only, thus gives a more accurate picture of the state of the skin beneath the patch. The edges of the patch appears blurred for two reasons, one being the mechanism of diffraction and the other being that the beam width (approximately 3 mm) was larger than the temporal spacing for the image (1 mm). It can be observed that there is significant variation in the skin beneath the patch, which is only apparent in the sparse reconstruction results and not in the processed waveform results. This variation could be due to the occlusion process not being uniform across the skin, with areas becoming more hydrated faster than others, as the patch was only applied 2 minutes before the measurement began.

5.5 Discussion

In this chapter it was found that the THz sparse deconvolution and reconstruction method introduced was able to monitor skin hydration levels through TDD patches

and these results were verified by a comparison to a standard method. Two studies were conducted, one to observe the short-term response of the skin to TDD patches over 2 hours and one to observe the long-term response over 24 hours. It was discovered that the majority of the hydrating effect occurs within the first 30 minutes of patch application and persists for at least 24 hours given that the patch remains applied. As a comparison between patch backing materials, occlusive film backing resulted in greater skin hydration than the permeable woven backed patches. Differing percentages of propylene glycerol had a slight effect on the hydration, with higher percentages resulting in less hydration, however further investigation into this is required as the results were generally within or close to the error. The design of TDD patches includes the appropriate choice of backing materials and both the choice and percentage of excipient used as a vehicle for the drug delivery. Furthermore, the hydration level of skin can be closely related to the efficacy of drug delivery, as the rate of drug absorption is strongly linked to the hydration level [106]. As such, it has been demonstrated that this THz sparse method has great potential in aiding the development of TDD patches.

In the case of this study there was only slight variation in skin hydration for the different excipient levels, but in situations such as a burn wound healing under a bandage there are significant hydration level changes [116]. A further application of this sparse reconstruction method could be for other situations where monitoring how the hydration level of skin underneath patches or bandages changes over time, without having to remove them, would be helpful. For example, observation of skin hydration in general has been exploited in the research and development of moist wound healing methods. Dry, moist and wet healing methods were compared and contrasted by Junker *et al.* [117]. It was shown that, compared to standard dry healing methods, a controlled wet environment promoted healing and reduced scar formation. Emerging moist healing methods using various commonly available dressings have been shown to effectively utilize the benefits of this healing method

[118]. Silicone gel sheeting is used to occlude severely burned skin as a treatment method, due to the increased water content helping with the burn healing process. Wang *et al.* studied the occlusive effects of silicone gel sheets applied to skin using THz measurements [58]. For many of these applications it would be necessary to take image measurements for the region of interest. To demonstrate the ability of this sparse deconvolution method to achieve this imaging through a layer, the skin beneath a film backed patch was successfully imaged. It is proposed that the method detailed in this chapter could be applied to aid in such research, especially in the case of there being a layer over the skin as this method has been shown to accurately extract skin hydration levels from underneath a TDD patch.

5.6 Summary

In this chapter, a sparse deconvolution method has been introduced and I have extended the method to include recreating individual sample reflections. This method was successfully employed to *in vivo* THz measurements of various TDD patches applied to skin. A verification via a comparison of sparse reconstruction results with the patch applied to standard measurements in the same locations immediately before or after the patch was applied or removed, respectively, was conducted. A significant difference in occlusion properties of patches with different backing materials was found, with a film backing proving to be much more occlusive than a woven backing. It was discovered that the majority of the occlusion effects occurred within the first 30 minutes of patch application and persisted for at least 24 hours if the patch remained applied. A slight difference between excipient levels was observed, with hydration decreasing with higher excipient concentration. However, this was generally within error bars and thus further research into this effect is required. Moreover, by processing an image of a film backed patch applied to skin, it was demonstrated that this method could monitor the whole area of skin beneath

the patch. Further work could include using this method to observe wound healing beneath casts or bandages, as the healing process is closely linked to skin hydration levels. Additionally, moist and wet healing methods are gaining traction, as it has been shown that wounds can heal better in moist conditions. This sparse reconstruction method of THz-TDS data could be applied to help with THz research into these healing methods by monitoring hydration levels noninvasively.

Chapter 6

Skin Product Testing using Real and Artificial Skin

6.1 Introduction

Skin products are used for a wide range of reasons, ranging from the treatment of various medical skin conditions to aesthetic improvements. However, before these products can be made commercially available they must undergo vigorous testing to ensure their efficacy and safety. With the interest of providing a new avenue of research for such purposes, the use of THz-TDS on *in vivo* skin and hydrogel artificial skin will be explored in this chapter. Skin phantoms and artificial skin in general were introduced in section 1.2.3, where the uses and benefits of using them were highlighted. In this case, hydrogel has been chosen to be used as the artificial skin due to the high and controllable water content contained within them. Furthermore, the other key ingredient is collagen which is a protein found in skin, thus it could make an accurate phantom for skin.

A key aspect in many skin products is their photoprotective ability. There are many naturally occurring photoprotective compounds; examples span melanin, flavonoids, polyphenols and mycosporine-like amino acids (MAAs) [119]. The latter

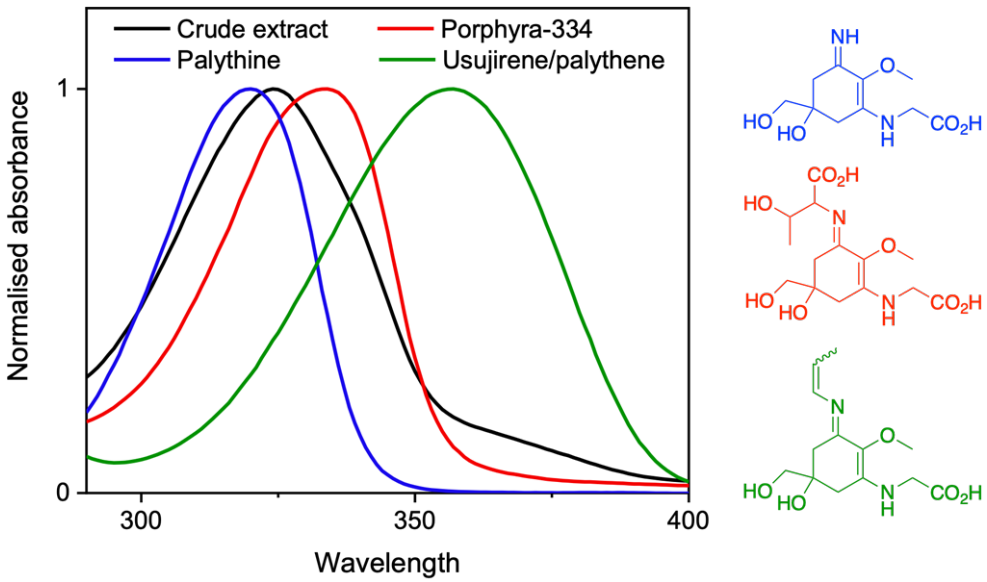

Figure 6.1: Normalised UV-visible spectra, over the UVA and UVB regions, of the crude extract (black) and common MAAs found in *Palmaria palmata*; palythine (blue), porphyra-334 (red), usujirene and palythene (green) along with their structures.

are a family of molecules synthesized by many micro- and macroorganisms that have the basic core structure of a cyclohexenone or cyclohexenimine [120]. MAAs are differentiated by the various substituents at the imino position, with a recent database reporting over 70 different structures [121]. The various substituents result in a shift in the peak absorption spanning 310-362 nm; a broad range within both the UVA (400-315 nm) and UVB (315-280 nm) regions [121]. This is significant given that UVA and UVB is the highest energy radiation that reaches the Earth's surface and has damaging implications to nature and humans [122]. Figure 6.1 demonstrates this broad band spectral coverage of a number of common MAAs found in *Palmaria palmata*, in addition to a crude extract obtained from *Palmaria palmata* which will be used in this study.

In this chapter an interesting sample of crude algae extract is introduced

and a THz experimental procedure for *in vivo* skin measurements, hydrogel measurements and liquid transmission measurements for investigating skin products is described. The THz response of skin and hydrogel were investigated, for before and 10 minutes after glycerol and commercial moisturiser application. It was shown that hydrogel has a strong potential to be used as artificial skin for THz-TDS. The hydrating effect of the crude extract was investigated on hydrogel, finding that it could provide a higher hydrating effect after 10 minutes when compared to commercial moisturiser. Furthermore, the photostability of the crude extract was investigated by comparing transmission measurements in frequency domain for before and after irradiation with a solar simulator. This result was compared to the frequency domain results of glycerol being applied to skin, with the potential of THz being used to assess the stability of products like this crude extract when applied to skin being suggested.

6.2 Samples and Experiment

6.2.1 Samples

The first sample used in this study is pure glycerol, which is a well known component of moisturisers and other skin products. The second sample is a commercial moisturiser purchased for this study and produced by Liz Earle Beauty Co. Limited. Both of these samples are completely safe to be applied to human skin. The last two samples are a crude extract of different concentrations in glycerol, one of 0.05 g/L and the other of 0.84 g/L. The hydrogels used in this study composed of 60% water, with the rest being a collagen mix.

This crude extract was obtained from a simple extraction process on dried *Palmaria palmata*, which was commercially sourced from The Cornish Seaweed Company. Details on the extraction process can be found in the supporting information of the paper declared for this chapter. Seven MAAs were identified in the sample; pa-

lythine, asterina-330, palythinol, shinorine, porphyra-334, usujirene and palythene. This group of MAAs are in line with previous literature that has investigated MAA content in *Palmaria palmata* [123, 124].

6.2.2 Skin Measurements

The Menlo system was used for measurements taken for this chapter, which was introduced in Section 2.4.2. For the *in vivo* skin measurements the protocol outline in Chapter 3.6 was followed, as to control external factors such as the pressure between the skin and imaging window, occlusion of skin and the temperature of the laboratory. Subjects remained in the laboratory for the duration of the experiment. Written informed consent was obtained from each subject prior to their involvement in the study. The study was approved by the Biomedical Scientific Research Ethics Committee, BSREC, (REGO-2018-2273 AM03).

For each subject, the left arm was used as a control and the right arm had the product applied to it. Initially, both arms were measured before any product was applied. Immediately after the right arm was measured, 0.1 ml of the product was applied using a micropipette. This was gently rubbed into the skin using a finger covered by a glove to ensure the sample was not transmitted to the other hand. After 10 minutes had passed, both arms were measured again.

6.2.3 Hydrogel Measurements

The experimental procedure began by taking a THz point measurement of the top face for the hydrogel cubes, approximately 1 cm^3 in size. An example of one of the hydrogel pieces on the imaging window is shown in Figure 6.2. To ensure good contact between the hydrogel and the imaging window, a slight pressure was applied. Before the measurement was taken, the hydrogel cubes were kept in a sealed bag to maintain their hydration level. A 0.1 ml of each sample was then uniformly applied to the top face of the different hydrogel cubes. After a 10-minute wait the THz

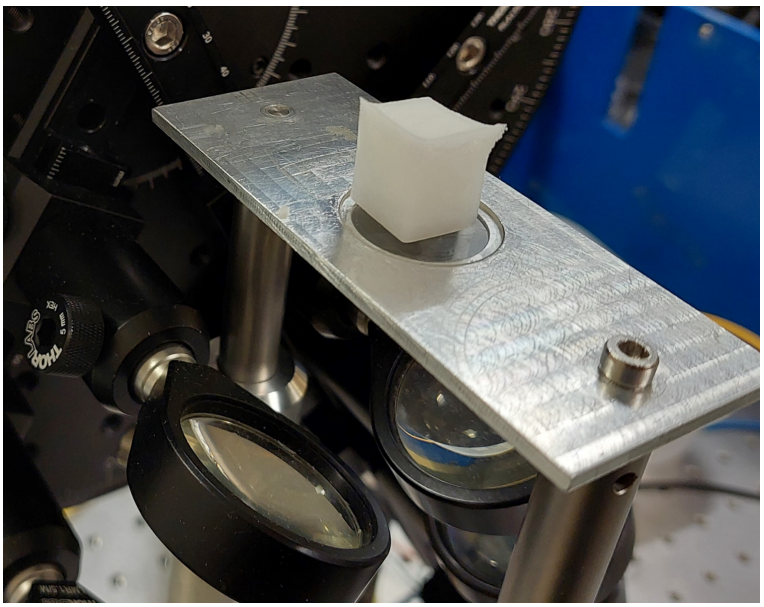

Figure 6.2: A picture of one of the hydrogel pieces being measured by the Menlo K15 system. The hydrogel cube is roughly 1 cm^3 in size.

measurements were taking again, in the same manner as previously. Furthermore, this procedure was carried out for a cube without applying any product, as to ascertain how the surface of the hydrogel naturally dries out over a 10 minute period.

6.2.4 Liquid Transmission Measurements

For the transmission measurements, the crude extract solution (0.84 g/L) was contained in a liquid sample cell, which was formed with two quartz windows separated by a 200 μm-thick Teflon spacer. The crude extract solution was measured before and after 2 hours of irradiation with a solar simulator with 50 pulses acquired each time, using the Menlo system in transmission geometry.

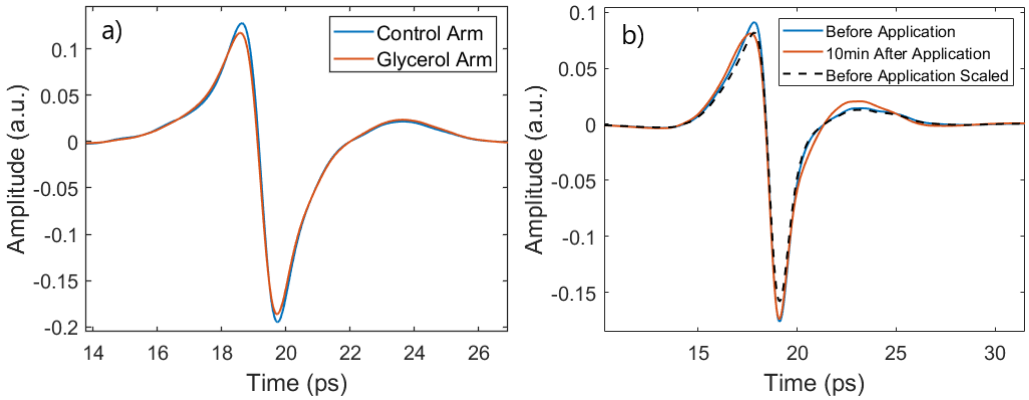

Figure 6.3: a) An example of the processed waveforms for one subject's volar forearms, 10 minutes after glycerol was applied to one arm. b) The processed waveform for the hydrogel immediately before the glycerol was applied, 10 minutes after application and the initial hydrogel measurement scaled to account for the drying effect after 10 minutes.

6.3 Results

6.3.1 Glycerol

To investigate the potential of this hydrogel as artificial skin for the THz region, the effect of glycerol on skin and hydrogel is contrasted. Glycerol is a key component in many skin products which is perfectly safe and tested to be used on skin. By following the procedure explained in the Section 6.2.2, five subjects had *in vivo* measurements of one volar forearm with glycerol applied and the other without any product applied. An example of the processed waveforms for one of the subjects is shown in Figure 6.3 a), where a clear reduction in the peak-to-peak is found when comparing the control and glycerol arms 10 minutes after the glycerol was applied. As explained throughout this thesis, the decrease of *in vivo* skin measurement peak-to-peak indicates an increase in hydration for that skin. To account for the natural variation of skin, and the difference of skin between different subjects, the average NRC for these results along with the initial measurements will be presented. The NRC is described in Section 3.7 and defined by Equation 3.2, with this case using t as 10 minutes. For the data collected from the 5 subjects the resulting NRC was

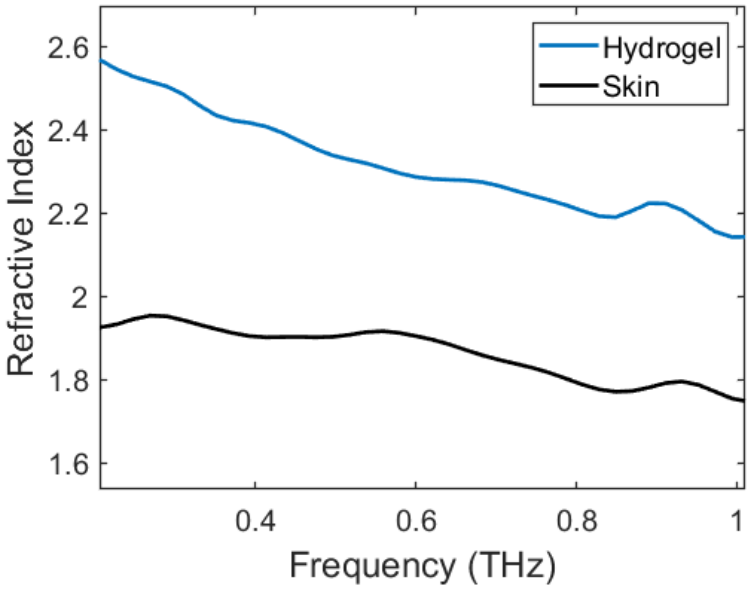

Figure 6.4: The refractive index of hydrogel and *in vivo* skin.

$-(6.4 \pm 0.2)\%$, with the error being the standard error in the mean.

To compare this skin result to, hydrogel measurements were carried out following the methodology explained in Section 6.2.3. Figure 6.3 b) shows the processed waveforms for a piece of hydrogel immediately before glycerol application and for 10 minutes after application. Furthermore, a scaled version of the initial measurement is included, to visually show how the hydrogel dries out when it is not in a sealed environment. By measuring how a blank piece of hydrogel dries out over a 10 minute period, we can scale the initial measurement based on this dehydration curve. In terms of the NRC result, the effect from the hydrogel drying out will automatically be accounted for. The resulting NRC was found to be $(6.5 \pm 0.1)\%$. The error was estimated from the standard deviation of multiple blank hydrogel measurements. This is an increase as opposed to the decrease seen in the skin measurements, which initially is not promising. By comparing the refractive index of skin and hydrogel, presented in Figure 6.4, and with the knowledge of the quartz imaging window having a stable refractive index of 2.12, it can be seen that the refractive index of skin is below that of quartz whilst the refractive index of hydrogel is above. The refractive

indices were calculated using the theory outline in Section 2.3.2. The addition of water increases the refractive index in both cases, thus results in a smaller reflection amplitude from skin as the refractive index draws closer to that of quartz and a larger one from hydrogel as it moves further from that of quartz. Fortunately, as the refractive index of quartz is in the middle of the refractive indices of skin and hydrogel the magnitude of the NRC can be comparable. Thus, when accounting for this phase difference, it has been shown that hydrogel could be used to mimic the THz response of skin for the case of glycerol.

6.3.2 Moisturiser

To further investigate the use of hydrogel as artificial skin, the same experiment as in the previous section is conducted but for the application of a commercial moisturiser in place of glycerol. An example of the processed waveforms from the data of one subject is shown in Figure 6.5 a), where a clear reduction in the peak-to-peak for skin which had moisturiser applied can be observed. The average NRC in this peak-to-peak for the 5 subjects measured was found to be $-(8.4 \pm 0.3)\%$, where the standard error in the mean is presented. The hydrogel processed waveform results for the application of moisturiser is shown in Figure 6.5 b). Here, an increase in peak-to-peak for the hydrogel with moisturiser applied as compared to the expected result without any moisturiser being applied can be clearly seen. The resulting NRC was calculated as $(8.7 \pm 0.1)\%$, with the error estimated from the standard deviation of multiple blank hydrogel measurements. As for the glycerol results, when accounting for the phase difference the magnitude of the NRC between *in vivo* skin and the hydrogel results closely agree, indicating the potential for such hydrogel to be used as artificial skin.

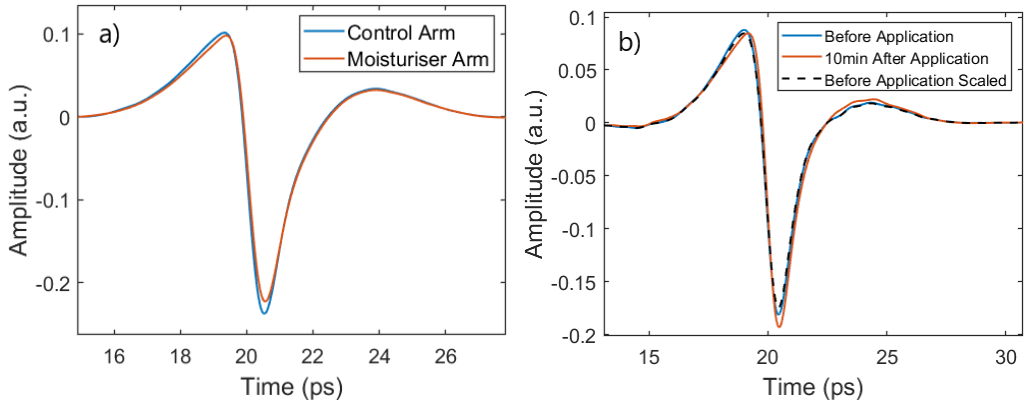

Figure 6.5: a) An example of the processed waveforms for one subject's volar forearms, 10 minutes after commercial moisturiser was applied to one arm. b) The processed waveform for the hydrogel immediately before the moisturiser was applied, 10 minutes after application and the initial hydrogel measurement scaled to account for the drying effect after 10 minutes.

6.3.3 Crude Extract

The two samples of crude extract introduced in Section 6.2.1 were applied to different hydrogel cubes and measured as outlined in Section 6.2.3. As this crude extract is newly developed, it has not passed the regulations for application to *in vivo* skin, as such only the application to hydrogel will be investigated. The NRC in the processed waveforms for the first sample (0.05 g/L) was (6.7±0.1)% and for the second sample (0.84 g/L) it was (12.4±0.1)%. By comparing this to the hydrogel moisturiser result of $(8.7 \pm 0.1)\%$ it can be seen that the lower concentration of crude extract has less of a hydrating effect on the hydrogel, however the higher concentration has a much larger hydrating effect. As the close relationship between the hydrogel results and *in vivo* skin results have been demonstrated in the previous two sections, it is indicated that this crude extract has a high potential for keeping skin hydrated.

Here we show the future potential for monitoring the stability of the crude extract once applied onto skin. Figure 6.6 a) shows the THz transmission spectroscopy results for the crude extract in glycerol (0.84 g/L) before and after irradiation. This irradiation was designed to mimic the power and spectrum of the Sun's light on the

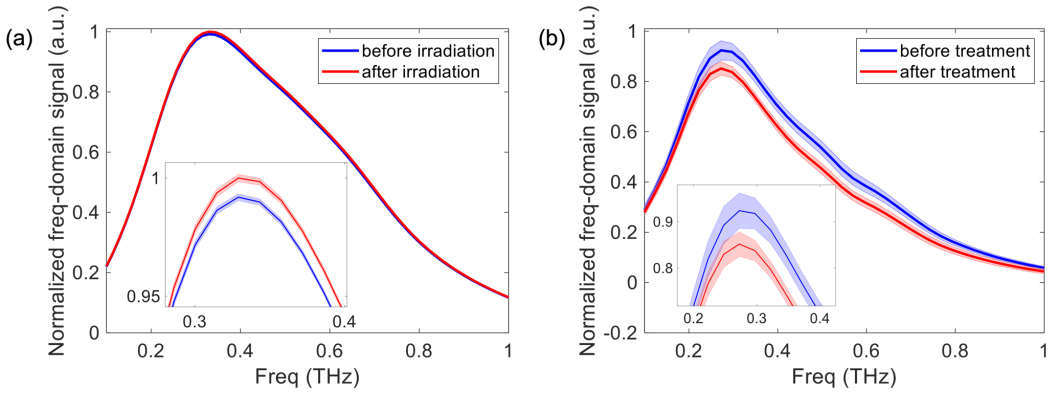

Figure 6.6: a) Mean normalised THz spectrum of crude extract in glycerol before and after 2 hours of irradiation with a solar simulator. b) Mean normalised THz spectrum of the volar forearm before and after applying glycerol to the skin. Insets of a) and b) are magnifications of the THz spectra at the peak. The error bars represent the standard deviation.

surface of the Earth. There is only a very small amplitude change of 0.82% between the measurements indicating that the extract is stable. Figure 6.6 b) shows the THz reflection spectroscopy results of the volar forearm before and after applying glycerol to the skin, averaged over 5 subjects. We see a clear difference in the THz spectrum of the skin due to the presence of glycerol. Therefore, THz reflection spectroscopy could be used to determine the stability of the extract when applied to the skin as part of a skin product and potentially evaluate other products within surface applications in the future.

6.4 Discussion

The potential of using hydrogel as artificial skin for skin product testing in the THz region was explored by contrasting measurements of glycerol and moisturiser on *in vivo* skin and hydrogel. The magnitude of the NRC in the processed waveforms for before and 10 minutes after the application of the skin products were found to closely match for the *in vivo* and hydrogel results, indicating the strength of this hydrogel as artificial skin. However, the sign of these NRCs were opposite,

with a decrease occurring in the skin measurements and an increase in the hydrogel measurements. This was due to the refractive index difference between the two, crucially with the refractive index of the quartz imaging window being between the two. For the frequency range used, the refractive index of quartz was close to being exactly midway between skin and hydrogel, contributing towards the magnitude of the NRC being the same between the two. The hydrogel could be improved by creating a version which has the same refractive index profile as skin. Furthermore, the hydrogel did dry out quickly when in an unsealed environment, as such a further improvement could be in ensuring a better hydration retention for the hydrogel. Measurements were taken for 24 hours after application of the skin products, however by this point the hydrogel had significantly dried out and became fairly hard, so good contact between the imaging window and hydrogel could not be made. Regardless, it was shown that THz measurements can effectively judge the hydrating effect of skin products in both *in vivo* skin and in hydrogel.

As the crude extract introduced in this chapter has been recently developed, it has not yet been sufficiently tested to be used on human subjects. This is precisely the kind of situation in which artificial skin can be very useful, as it allows for the study of how the product could interact with real skin without any risk to subjects. Again, the NRC of the processed waveforms for before and 10 minutes after the application of the crude extract to the hydrogel were calculated. The lower concentration of crude extract (0.05 g/L) had less of a hydrating effect than the commercial moisturiser on hydrogel did, however the higher concentration (0.84 g/L) had a significantly higher hydrating effect. The NRC results for the crude extract, glycerol and moisturiser are summarised in Table 6.1.

Many skin products, especially sunscreens, must have strong photostability. The crude extract was found to be very stable, as only a small frequency domain amplitude change of 0.82% was found after 2 hours of irradiation with a solar simulator. By comparing these frequency domain results to that of the application of

Sample	Skin NRC (%)	Hydrogel NRC (%)
Glycerol	-6.4	6.5
Moisturiser	-8.4	8.7
Crude Extract (0.05 g/L)	-	6.7
Crude Extract (0.84 g/L)	-	12.4

Table 6.1: A summary of the NRC results from the studies conducted for this chapter.

glycerol to skin, it was proposed that THz could be used to judge the stability of crude extract, or similar products, when applied to skin. Further work could include the use of hydrogel as artificial skin to predict the photostability of products on real skin, by applying the product to the hydrogel and taking THz measurements, then irradiating the hydrogel and finally measuring it again.

6.5 Summary

This chapter explored the use of THz light for the assessment of skin products on both *in vivo* skin and hydrogel, as well as the efficacy of hydrogel as artificial skin in the THz region. The products investigated were glycerol, a commercial moisturiser and a crude extract taken from *Palmaria palmata*. The NRC in the THz processed waveforms for the application of glycerol and moisturiser closely matched for results on *in vivo* skin and hydrogel, once the sign difference had been accounted for. This indicated that hydrogel could be used as artificial skin which accurately mimics real skin. A concentration of crude extract in glycerol (0.84 g/L) was found to have a significantly higher hydrating effect on hydrogel when compared to the commercial moisturiser. The NRC results for this chapter are summarised in Table 6.1. Furthermore, the photostability of the crude extract was shown to be very stable when using frequency domain THz results. It was proposed that THz could be used to assess the photostability of skin products when they had been applied to skin, or when applied to hydrogel to predict the response on real skin.

Chapter 7

Summary and Future Work

7.1 Summary of the Thesis

In this thesis, THz imaging and spectroscopy methods are combined with sparse deconvolution and FRI methods to study skin *in vivo*. This work also contains a study of different variables which affect *in vivo* skin measurements to create a robust protocol for studies on the skin, and an investigation into using hydrogel as artificial skin.

In Chapter 1 THz spectroscopy is introduced, including THz light in general, the equipment involved in THz-TDS and the generation and detection of THz. Furthermore, many applications of THz research are described with a heavy emphasis on biomedical research. The general wave theory used for this thesis is explained in Chapter 2, with wave propagation and the basic processing of THz transmission and reflection geometry measurements being covered. Additionally, the specific THz-TDS systems used to collect the data presented in this thesis are described.

Chapter 3 presents studies into many factors which affect *in vivo* THz skin measurements. Two significant factors, occlusion of the skin by the imaging window and the pressure between the two, have their mechanisms explained and their effect on the THz response of skin investigated. Many patient dependent factors were

also studied, with my key findings including no significant difference between a patient's left and right volar forearms and a significant difference found between male Caucasian and male Asian subjects. An *in vivo* skin measurement protocol is presented, which accounts for the factors presented to ensure accurate results during such studies. Finally, the NRC is introduced, which helps to account for patient dependent factors and the natural change of skin over time by, for example, using one of the patient's volar forearms as a control for the other.

A FRI method for the low sampling of THz measurements is described in Chapter 4, including my creation of a sampling kernel to mimic a THz pulse. FRI has not been applied to experimental THz measurements in published research before my work. This method is verified with both simulated and simple experimental results. The low sampling of skin measurements is shown to be accurate, by comparing to fully sampled results, and a study on an adhesive dressing applied to the skin is conducted. This chapter demonstrates that the FRI method presented produces accurate results for THz *in vivo* skin studies at very low sampling rates. Furthermore, in the case of the adhesive dressing study, it was shown to be able to discern hydration levels beneath the dressing which was linked to the presence of antiseptic cream.

Chapter 5 uses my reconstruction technique from a THz sparse deconvolution method to monitor the hydration of skin underneath TDD patches. To verify the method presented, a comparison of sparse reconstruction results with the patch applied and standard processing results for immediately after the same patch was removed is included. Key results of the studies conducted included that the film backing for the patches was much more occlusive than the woven backed patches, resulting in a higher hydration of the skin. Additionally, it was found that the majority of the hydrating effect occurred within the first 30 minutes of patch application and persisted for at least 24 hours with the patch remaining applied. This work demonstrates the potential of THz technology to aid with TDD patch research

and development.

Finally, Chapter 6 contained our studies investigating skin product testing using THz measurements on *in vivo* skin and hydrogel, which was being used as artificial skin. By comparing measurements of glycerol and moisturiser applied to hydrogel and *in vivo* skin the high potential of hydrogel for use as artificial skin is shown. A crude extract obtained from *Palmaria palmata* was studied by applying it to hydrogel, where it demonstrated a higher hydration effect when compared to a commercial moisturiser. Furthermore, the photostability of the crude extract was shown to be very stable when observing the frequency domain THz results for before and after irradiation with a solar simulator.

7.2 Future Work

The key advantage of the THz FRI method is the low sampling rate it enables, which in turn provides quicker measurement times. This provides the potential of *in vivo* imaging of an area of skin, which would be required for the diagnosis of diseases such as skin cancer. As the skin is effected by occlusion, very fast measurement times would be necessary for this factor to not significantly effect the data during the measurement. Therefore, this method could enable rapid THz image acquisition, especially if it were to be combined with other methods such as single-pixel imaging [100]. In this work, Stantchev *et al.* were able to acquire a 32x32 pixel image at a rate of six images per second. By combining this with the FRI method introduced in this thesis, even faster image acquisition rates could be obtained.

The effectiveness of the THz sparse reconstruction method at measuring the hydration of the skin beneath a layer was demonstrated in the TDD patch study conducted. There are many other cases where monitoring the hydration of skin through a layer would be highly valuable, such as in the study of moist and wet

healing methods. Much research has shown the great potential of these healing methods [117, 118], which usually require some form of layer to be applied to the skin to create the wet environment. By using the sparse method the hydration level of the skin during these treatments could better be monitored. As hydration levels of the damaged skin have been closely linked to wound healing processes [116], this method could also be employed to monitor how a wound is healing beneath a layer such as a bandage, without having to remove the bandage.

Both the FRI and sparse deconvolution methods presented in this thesis heavily rely on the quality of the reference used. This reference should be a single pulse which closely resembles one reflection of interested from the sample, such as the patch-skin reflection for the TDD patch study. Therefore, obtaining a better quality reference could significantly improve the results produced by these methods. To do this, a reflection measurement using a metal mirror to capture the whole pulse could be edited using a model in order to closely mimic a reflection from the sample. Another option to improve the reference would be to find a homogeneous artificial skin option with a refractive index closely matching skin for the THz region, and measuring the reference reflection from this.

Hydrogel was effectively used as artificial skin, however there was a mismatch between the refractive index of the hydrogel and that of real skin. Therefore, an improvement would be to create a version of this hydrogel with a refractive index closer to that of skin, thus no further interpretation of the results would be required. Furthermore, creating hydrogel samples with better hydration retention would allow for longer studies using this as artificial skin. This hydrogel could also be used to predict the photostability of products on real skin, such as the crude extract investigated in this thesis.

Bibliography

[1] D. H. Auston. Picosecond optoelectronic switching and gating in silicon. *Applied Physics Letters*, 26(3):101–103, 1975.

[2] S. S. Dhillon, M. S. Vitiello, E. H. Linfield, A. G. Davies, and M. C. Hoffmann *et al.* The 2017 terahertz science and technology roadmap. *Journal of Physics D: Applied Physics*, 50(4):043001, 2017.

[3] X. Yang, X. Zhao, K. Yang, Y. Liu, Y. Liu, W. Fu, and Y. Luo. Biomedical applications of terahertz spectroscopy and imaging. *Trends in Biotechnology*, 34(10):810–824, 2016.

[4] D. H. Auston and K. P. Cheung. Coherent time-domain far-infrared spectroscopy. *Journal of the Optical Society of America B*, 2(4):606–612, 1985.

[5] M. Exter, C. Fattinger, and D. Grischkowsky. Terahertz time-domain spectroscopy of water vapor. *Optics Letters*, 14(20):1128–1130, 1989.

[6] J. Neu and C. A. Schmuttenmaer. Tutorial: An introduction to terahertz time domain spectroscopy (thz-tds). *Journal of Applied Physics*, 124(23):231101, 2018.

[7] S. Huang, P. C. Ashworth, K. W. C. Kan, Y. Chen, V. P. Wallace, Y. Zhang, and E. Pickwell-MacPherson. Improved sample characterization in terahertz reflection imaging and spectroscopy. *Optics Express*, 17(5):3848–3854, 2009.

[8] X. C. Zhang and J. Xu. *Introduction to THz Wave Photonics*. Springer, 2010.

[9] W. R. Tribe, D. A. Newnham, P. F. Taday, and M. C. Kemp. Hidden object detection: security applications of terahertz technology. In *Terahertz and Gigahertz Electronics and Photonics III*, volume 5354, pages 168 – 176. International Society for Optics and Photonics, SPIE, 2004.

[10] D. Zimdars and J. S. White. Terahertz reflection imaging for package and personnel inspection. In *Terahertz for Military and Security Applications II*, volume 5411, pages 78 – 83. International Society for Optics and Photonics, SPIE, 2004.

[11] M. C. Kemp, P. F. Taday, B. E. Cole, J. A. Cluff, A. J. Fitzgerald, and W. R. Tribe. Security applications of terahertz technology. In *Terahertz for Military and Security Applications*, volume 5070, pages 44 – 52. International Society for Optics and Photonics, SPIE, 2003.

[12] V. Wallace, P. Taday, A. Fitzgerald, R. Woodward, J. Cluff, J. Pye, and D. Arnone. Terahertz pulsed imaging and spectroscopy for biomedical and pharmaceutical applications. *Faraday discussions*, 126:255–63; discussion 303, 2004.

[13] H.-B. Liu, Y. Chen, and X.-C. Zhang. Characterization of anhydrous and hydrated pharmaceutical materials with thz time-domain spectroscopy. *Journal of Pharmaceutical Sciences*, 96(4):927–934, 2007.

[14] R. K. May, M. J. Evans, S. Zhong, I. Warr, L. F. Gladden, Y. Shen, and J. A. Zeitler. Terahertz in-line sensor for direct coating thickness measurement of individual tablets during film coating in real-time. *Journal of Pharmaceutical Sciences*, 100(4):1535–1544, 2011.

[15] J. A. Zeitler, Y. Shen, C. Baker, P. F. Taday, M. Pepper, and T. Rades. Analysis of coating structures and interfaces in solid oral dosage forms by three

dimensional terahertz pulsed imaging. *Journal of Pharmaceutical Sciences*, 96(2):330–340, 2007.

[16] K. Su, Y.-C. Shen, and J. A. Zeitler. Terahertz sensor for non-contact thickness and quality measurement of automobile paints of varying complexity. *IEEE Transactions on Terahertz Science and Technology*, 4(4):432–439, 2014.

[17] P. Mousavi, F. Haran, D. Jez, F. Santosa, and J. S. Dodge. Simultaneous composition and thickness measurement of paper using terahertz time-domain spectroscopy. *Applied Optics*, 48(33):6541–6546, 2009.

[18] K. Dutzi, N. Regner, N. Vieweg, M. Kehrt, A. Steiger, H. Abele, C. Kaya, and T. Stegmaier. Thickness gauging of waterproof textiles using fast thz-tds. In *2022 47th International Conference on Infrared, Millimeter and Terahertz Waves (IRMMW-THz)*, 2022.

[19] J. Dong, A. Locquet, M. Melis, and D. S. Citrin. Global mapping of stratigraphy of an old-master painting using sparsity-based terahertz reflectometry. *Scientific Reports*, 7(1):15098, 2017.

[20] A. Gomez-Sepulveda, A. Hernández Serrano, R. Radpour, C. Koch Dandolo, C. Landeros, L. Ascencio-Rojas, A. Zarate, G. Hernandez, C. González Tirado, M. Insaurralde, and E. Castro-Camus. History of mexican easel paintings from an altarpiece revealed by non-invasive terahertz time-domain imaging. *Journal of Infrared, Millimeter, and Terahertz Waves*, 38(4):403–412, 2017.

[21] C. L. Koch-Dandolo, T. Filtenborg, K. Fukunaga, J. Skou-Hansen, and P. U. Jepsen. Reflection terahertz time-domain imaging for analysis of an 18th century neoclassical easel painting. *Applied Optics*, 54(16):5123–5129, 2015.

[22] J. Dong, J. B. Jackson, M. Melis, D. Giovanacci, G. C. Walker, A. Locquet, J. W. Bowen, and D. S. Citrin. Terahertz frequency-wavelet domain decon-

volution for stratigraphic and subsurface investigation of art painting. *Optics Express*, 24(23):26972–26985, 2016.

[23] K. Fukunaga, Y. Ogawa, S. Hayashi, and I. Hosako. Terahertz spectroscopy for art conservation. *IEICE Electronics Express*, 4(8):258–263, 2007.

[24] W. Xu, L. Xie, and Y. Ying. Mechanisms and applications of terahertz metamaterial sensing: a review. *Nanoscale*, 9(37):13864–13878, 2017.

[25] I. Amenabar, F. Lopez, and A. Mendikute. In introductory review to thz non-destructive testing of composite mater. *Journal of Infrared, Millimeter, and Terahertz Waves*, 34(2):152–169, 2013.

[26] I. Duling and D. Zimdars. Terahertz imaging: Revealing hidden defects. *Nature Photonics*, 3(11):630–632, 2009.

[27] C. Stoik, M. Bohn, and J. Blackshire. Nondestructive evaluation of aircraft composites using reflective terahertz time domain spectroscopy. *NDT and E International*, 43(2):106–115, 2010.

[28] I. Kallfass, J. Antes, T. Schneider, F. Kurz, D. Lopez-Diaz, S. Diebold, H. Massler, A. Leuther, and A. Tessmann. All active mmic-based wireless communication at 220 ghz. *IEEE Transactions on Terahertz Science and Technology*, 1(2):477–487, 2011.

[29] G. Ducournau, P. Szriftgiser, F. Pavanello, E. Peytavit, M. Zaknoune, D. Bacquet, A. Beck, T. Akalin, and J.-F. Lampin. Thz communications using photonics and electronic devices: the race to data-rate. *Journal of Infrared, Millimeter, and Terahertz Waves*, 36(2):198–220, 2014.

[30] D. F. Plusquellic, K. Siegrist, E. J. Heilweil, and O. Esenturk. Applications of terahertz spectroscopy in biosystems. *ChemPhysChem*, 8(17):2412–2431, 2007.

[31] L. Thrane, R. H. Jacobsen, P. Uhd Jepsen, and S. R. Keiding. Thz reflection spectroscopy of liquid water. *Chemical Physics Letters*, 240(4):330–333, 1995.

[32] M. Constantin, E. Poenaru, C. Poenaru, and T. Constantin. Skin hydration assessment through modern non-invasive bioengineering technologies. *Mædica*, 9:33–8, 03 2014.

[33] A. Rougier and C. Lotte. *In Vivo Relationship Between Percutaneous Absorption and Transepidermal Water Loss*, pages 115–128. Taylor and Francis, 2002.

[34] H. Lindley-Hatcher, A. I. Hernandez-Serrano, J. Wang, J. Cebrian, J. Hardwicke, and E. Pickwell-MacPherson. Evaluation of in vivo thz sensing for assessing human skin hydration. *Journal of Physics: Photonics*, 3(1):014001, 2020.

[35] C. M. Hough, D. N. Purschke, C. Huang, L. V. Titova, O. Kovalchuk, B. J. Warkentin, and F. A. Hegmann. Biological effects of intense thz pulses on human skin tissue models. In *2017 42nd International Conference on Infrared, Millimeter, and Terahertz Waves (IRMMW-THz)*, 2017.

[36] A. A. Angeluts, A. B. Gapeyev, M. N. Esaulkov, O. G. Kosareva, S. N. Matyunin, M. M. Nazarov, T. N. Pashovkin, P. M. Solyankin, O. P. Cherkasova, and A. P. Shkurinov. Study of terahertz-radiation-induced dna damage in human blood leukocytes. *Quantum Electronics*, 44(3):247, 2014.

[37] O. P. Cherkasova, D. S. Serdyukov, E. F. Nemova, A. S. Ratushnyak, A. S. Kucheryavenko, I. N. Dolganova, G. Xu, M. Skorobogatiy, I. V. Reshetov, P. S. Timashev, I. E. Spektor, K. I. Zaytsev, and V. V. Tuchin. Cellular effects of terahertz waves. *Journal of Biomedical Optics*, 26(9):090902, 2021.

[38] C. Xu, X. Wang, and M. Pramanik. *Imaging Technologies and Transdermal Delivery in Skin Disorders*. John Wiley and Sons, 2019.

[39] K. W. Ng, W. M. Lau, N. Dragicevic, and H. I. Maibach. *Skin Deep: The Basics of Human Skin Structure and Drug Penetration.* Springer Berlin Heidelberg, 2015.

[40] B. E. Cole, R. M. Woodward, D. A. Crawley, V. P. Wallace, D. D. Arnone, and M. Pepper. Terahertz imaging and spectroscopy of human skin in vivo. In *Commercial and Biomedical Applications of Ultrashort Pulse Lasers; Laser Plasma Generation and Diagnostics*, volume 4276. International Society for Optics and Photonics, SPIE, 2001.

[41] I. Echchgadda, J. Grundt, M. Tarango, B. Ibey, T. Tongue, M. Liang, H. Xin, and G. Wilmink. Using a portable terahertz spectrometer to measure the optical properties of in vivo human skin. *Journal of biomedical optics*, 18(12):120503, 2013.

[42] V. K. Tippavajhala, T. D. Magrini, D. C. Matsuo, M. GP Silva, P. P. Favero, L. R. De Paula, and A. A. Martin. In vivo determination of moisturizers efficacy on human skin hydration by confocal raman spectroscopy. *AAPS PharmSciTech*, 19:3177–3186, 2018.

[43] J. Wang, H. Lindley-Hatcher, X. Chen, and E. Pickwell-MacPherson. Thz sensing of human skin: A review of skin modeling approaches. *Sensors*, 21(11), 2021.

[44] B. C. Q. Truong, A. J. Fitzgerald, S. Fan, and V. P. Wallace. Concentration analysis of breast tissue phantoms with terahertz spectroscopy. *Biomedical Optics Express*, 9(3):1334–1349, 2018.

[45] N. Bajwa, J. Garritano, Y. K. Lee, P. Tewari, S. Sung, A. Maccabi, B. Nowroozi, M. Babakhanian, S. Sanghvi, R. Singh, W. Grundfest, and Z. Taylor. Reflective terahertz (THz) imaging: system calibration using hydration phantoms. In *Terahertz and Ultrashort Electromagnetic Pulses for*

Biomedical Applications, volume 8585, page 85850W. International Society for Optics and Photonics, SPIE, 2013.

[46] D. Jayasankar, A. I. Hernandez-Serrano, R. A. Hand, J. Stake, and E. MacPherson. Investigation of hydrogel skin phantoms using terahertz time-domain spectroscopy. In *2022 52nd European Microwave Conference (EuMC)*, pages 401–403, 2022.

[47] P. M. Corridon, R. Ascázubi, C. Krest, and I. Wilke. Time-domain terahertz spectroscopy of artificial skin. In *Advanced Biomedical and Clinical Diagnostic Systems IV*, volume 6080, page 608007. International Society for Optics and Photonics, SPIE, 2006.

[48] R. Zhang, K. Yang, Q. Abbasi, N. A. AbuAli, and A. Alomainy. Experimental characterization of artificial human skin with melanomas for accurate modelling and detection in healthcare application. In *2018 43rd International Conference on Infrared, Millimeter, and Terahertz Waves (IRMMW-THz)*, 2018.

[49] F. Wahaia, I. Kasalynas, R. Venckevicius, D. Seliuta, G. Valusis, A. Urbanowicz, G. Molis, F. Carneiro, C. D. Carvalho Silva, and P. L. Granja. Terahertz absorption and reflection imaging of carcinoma-affected colon tissues embedded in paraffin. *Journal of Molecular Structure*, 1107:214–219, 2016.

[50] Y. C. Sim, J. Y. Park, K.-M. Ahn, C. Park, and J.-H. Son. Terahertz imaging of excised oral cancer at frozen temperature. *Biomedical Optics Express*, 4(8):1413–1421, 2013.

[51] A. J. Fitzgerald, V. P. Wallace, M. Jimenez-Linan, L. Bobrow, R. J. Pye, A. D. Purushotham, and D. D. Arnone. Terahertz pulsed imaging of human breast tumors. *Radiology*, 239(2):533–540, 2006.

[52] R. M. Woodward, V. P. Wallace, R. J. Pye, B. E. Cole, D. D. Arnone, E. H. Linfield, and M. Pepper. Terahertz pulse imaging of ex vivo basal cell carcinoma. *Journal of Investigative Dermatology*, 120(1):72–78, 2003.

[53] Y. Sim, K.-M. Ahn, J. Y. Park, C.-S. Park, and J.-H. Son. Temperature-dependent terahertz imaging of excised oral malignant melanoma. *IEEE Transactions on Terahertz Science and Technology*, 3(4):368–373, 2013.

[54] K. I. Zaytsev, N. V. Chernomyrdin, K. G. Kudrin, A. A. Gavdush, P. A. Nosov, S. O. Yurchenko, and I. V. Reshetov. In vivo terahertz pulsed spectroscopy of dysplastic and non-dysplastic skin nevi. *Journal of Physics: Conference Series*, 735(1):012076, 2016.

[55] V. P. Wallace, A. J. Fitzgerald, S. Shankar, N. Flanagan, R. Pye, J. Cluff, and D. D. Arnone. Terahertz pulsed imaging of basal cell carcinoma ex vivo and in vivo. *British Journal of Dermatology*, 151(2):424–432, 2004.

[56] G. G. Hernandez-Cardoso, S. C. Rojas-Landeros, M. Alfaro-Gomez, A. I. Hernandez-Serrano, I. Salas-Gutierrez, E. Lemus-Bedolla, A. R. Castillo-Guzman, H. L. Lopez-Lemus, and E. Castro-Camus. Terahertz imaging for early screening of diabetic foot syndrome: A proof of concept. *Scientific Reports*, 7(1):42124, 2017.

[57] Z. D. Taylor, R. S. Singh, M. O. Culjat, J. Y. Suen, W. S. Grundfest, H. Lee, and E. R. Brown. Reflective terahertz imaging of porcine skin burns. *Optics letters*, 33(11):1258–60, 2008.

[58] J. Wang, Q. Sun, R. I. Stantchev, T.-W. Chiu, A. T. Ahuja, and E. Pickwell-MacPherson. In vivo terahertz imaging to evaluate scar treatment strategies: silicone gel sheeting. *Biomedical Optics Express*, 10(7):3584–3590, 2019.

[59] S. Fan, B. S. Y. Ung, E. P. J. Parrott, V. P. Wallace, and E. Pickwell-MacPherson. In vivo terahertz reflection imaging of human scars during and after the healing process. *Journal of Biophotonics*, 10(9):1143–1151, 2017.

[60] K. W. Kim, K.-S. Kim, H. Kim, L. Sang Hun, J.-H. Park, J.-H. Han, S.-H. Seok, J. Park, Y. Choi, Y. I. Kim, J. Han, and J.-H. Son. Terahertz dynamic imaging of skin drug absorption. *Optics express*, 20(9):9476–84, 2012.

[61] K. W. Kim, H. Kim, J. Park, J. K. Han, and J.-H. Son. Terahertz tomographic imaging of transdermal drug delivery. *IEEE Transactions on Terahertz Science and Technology*, 2(1):99–106, 2012.

[62] J. Wang, H. Hatcher, K. liu, and E. Pickwell-MacPherson. Evaluation of transdermal drug delivery usingterahertz pulsed imaging. *Biomedical Optics Express*, 11(8):4484–4490, 2020.

[63] D. I. Ramos-Soto, A. K. Singh, E. Saucedo-Casas, E. Castro-Camus, and M. Alfaro-Gomez. Visualization of moisturizer effects in stratum corneum in vitro using thz spectroscopic imaging. *Applied Optics*, 58(24):6581–6585, 2019.

[64] Z. D. Taylor, J. Garritano, S. Sung, N. Bajwa, D. B. Bennett, B. Nowroozi, P. Tewari, J. W. Sayre, J.-P. Hubschman, S. X. Deng, E. R. Brown, and W. S. Grundfest. Thz and mm-wave sensing of corneal tissue water content: In vivo sensing and imaging results. *IEEE Transactions on Terahertz Science and Technology*, 5(2):184–196, 2015.

[65] S. Sung, S. Selvin, N. Bajwa, S. Chantra, B. Nowroozi, J. Garritano, J. Goell, A. D. Li, S. X. Deng, E. R. Brown, W. S. Grundfest, and Z. D. Taylor. Thz imaging system for in vivo human cornea. *IEEE Transactions on Terahertz Science and Technology*, 8(1):27–37, 2018.

[66] U. Heugen, G. Schwaab, E. Bründermann, M. Heyden, X. Yu, D. M. Leitner, and M. Havenith. Solute-induced retardation of water dynamics probed

directly by terahertz spectroscopy. *Proceedings of the National Academy of Sciences*, 103(33):12301–12306, 2006.

[67] J. Sun, G. Niehues, H. Forbert, D. Decka, G. Schwaab, D. Marx, and M. Havenith. Understanding thz spectra of aqueous solutions: Glycine in light and heavy water. *Journal of the American Chemical Society*, 136(13):5031–5038, 2014.

[68] S. Huang, P. C. Ashworth, K. W. C. Kan, Y. Chen, V. P. Wallace, Y.-T. Zhang, and E. Pickwell-MacPherson. Improved sample characterization in terahertz reflection imaging and spectroscopy. *Optics Express*, 17(5):3848–3854, 2009.

[69] X. Chen, E. P. J. Parrott, B. S.-Y. Ung, and E. Pickwell-MacPherson. A robust baseline and reference modification and acquisition algorithm for accurate thz imaging. *IEEE Transactions on Terahertz Science and Technology*, 7(5):493–501, 2017.

[70] J. S. Orfanidis. *Introduction to Signal Processing.* Prentice-Hall, 1996.

[71] L. Angrisani, G. Cavallo, A. Liccardo, G. P. Papari, and A. Andreone. Thz measurement systems. In Luigi Cocco, editor, *New Trends and Developments in Metrology*, chapter 2. IntechOpen, Rijeka, 2016.

[72] X. Chen, E. P. J. Parrott, Z. Huang, H.-P. Chan, and E. Pickwell-MacPherson. Robust and accurate terahertz time-domain spectroscopic ellipsometry. *Photon. Res.*, 6(8):768–775, Aug 2018.

[73] W. Withayachumnankul, B. M. Fischer, H. Lin, and D. Abbott. Uncertainty in terahertz time-domain spectroscopy measurement. *J. Opt. Soc. Am. B*, 25(6):1059–1072, Jun 2008.

[74] Q. Sun, E. P. J. Parrott, Y. He, and E. Pickwell-MacPherson. In vivo thz imaging of human skin: Accounting for occlusion effects. *Journal of Biophotonics*, 11(2):e201700111, 2018.

[75] E. K. Chan, B. Sorg, D. Protsenko, M. O'Neil, M. Motamedi, and A. J. Welch. Effects of compression on soft tissue optical properties. *IEEE Journal of Selected Topics in Quantum Electronics*, 2(4):943–950, 1996.

[76] P. Clarys, R. Clijsen, and A. Barel. Influence of probe application pressure on in vitro and in vivo capacitance (corneometer cm 825) and conductance (skicon 200 ex) measurements. *Skin research and technology : ISBS*, 17(4):445–50, 2011.

[77] V. M. Rogiers. Eemco guidance for the assessment of transepidermal water loss in cosmetic sciences. *Skin Pharmacology and Physiology*, 14(2):117 – 128, 2001.

[78] A. V. Rawlings. Ethnic skin types: are there differences in skin structure and function? *International Journal of Cosmetic Science*, 28(2):79–93, 2006.

[79] X. Peralta, D. Lipscomb, G. Wilmink, and I. Echchgadda. Terahertz spectroscopy of human skin tissue models with different melanin content. *Biomedical Optics Express*, 10(6):2942, 2019.

[80] A. Firooz, B. Sadr, S. Babakoohi, M. Sarraf-Yazdy, F. Fanian, A. Kazerouni-Timsar, M. Nassiri-Kashani, M. M. Naghizadeh, and Y. Dowlati. Variation of biophysical parameters of the skin with age, gender, and body region. *The Scientific World Journal*, 2012(6):386936, 2012.

[81] K.-P. Wilhelm, A. B. Cua, and H. I. Maibach. Skin Aging: Effect on Transepidermal Water Loss, Stratum Corneum Hydration, Skin Surface pH, and Casual Sebum Content. *Archives of Dermatology*, 127(12):1806–1809, 1991.

[82] H. Dao and R. A. Kazin. Gender differences in skin: A review of the literature. *Gender Medicine*, 4(4):308–328, 2007.

[83] K. A. Engebretsen, J. D. Johansen, S. Kezic, A. Linneberg, and J. P. Thyssen. The effect of environmental humidity and temperature on skin barrier function and dermatitis. *Journal of the European Academy of Dermatology and Venereology*, 30(2):223–249, 2016.

[84] H. Qiu, X. Long, J. C. Ye, J. Hou, J. Senee, A. Laurent, R. Bazin, F. Flament, A. Adam, J. Coutet, and B. Piot. Influence of season on some skin properties: winter vs. summer, as experienced by 354 shanghaiese women of various ages. *International journal of cosmetic science*, 33(4):377—383, 2011.

[85] M. Matsui, E. Pelle, K. Dong, and N. Pernodet. Biological rhythms in the skin. *International Journal of Molecular Sciences*, 17(6):801, 2016.

[86] D. Voegeli. The effect of washing and drying practices on skin barrier function. *Journal of wound, ostomy, and continence nursing*, 35(1):84—90, 2008.

[87] M. Akdeniz, T. Tomova-Simitchieva, G. Dobos, U. Blume-Peytavi, and J. Kottner. Does dietary fluid intake affect skin hydration in healthy humans? a systematic literature review. *Skin Research and Technology*, 24(3):459–465, 2018.

[88] S. Lim, J. Shin, Y. Cho, and K.-P. Kim. Dietary patterns associated with sebum content, skin hydration and ph, and their sex-dependent differences in healthy korean adults. *Nutrients*, 11(3):619, 2019.

[89] M. Vetterli, P. Marziliano, and T. Blu. Sampling signals with finite rate of innovation. *IEEE Transactions on Signal Processing*, 50(6):1417–1428, 2002.

[90] R. Tur, Y. C. Eldar, and Z. Friedman. Innovation rate sampling of pulse streams with application to ultrasound imaging. *IEEE Transactions on Signal Processing*, 59(4):1827–1842, 2011.

[91] C. Han, I. F. Akyildiz, and W. H. Gerstacker. Timing acquisition and error analysis for pulse-based terahertz band wireless systems. *IEEE Transactions on Vehicular Technology*, 66(11):10102–10113, 2017.

[92] H. Pan, T. Blu, and M. Vetterli. Towards generalized fri sampling with an application to source resolution in radioastronomy. *IEEE Transactions on Signal Processing*, 65(4):821–835, 2017.

[93] C. S. Seelamantula and S. Mulleti. Super-resolution reconstruction in frequency-domain optical-coherence tomography using the finite-rate-of-innovation principle. *IEEE Transactions on Signal Processing*, 62(19):5020–5029, 2014.

[94] T. Blu, P.-L. Dragotti, M. Vetterli, P. Marziliano, and L. Coulot. Sparse sampling of signal innovations. *IEEE Signal Processing Magazine*, 25(2):31–40, 2008.

[95] B. Porat. *A Course in Digital Signal Processing*. John Wiley and Sons, 1997.

[96] S. M. Kay. *Modern spectral estimation : theory and application*. Prentice-Hall, 1988.

[97] J. H. Karl. 4 - couplets and elementary filters. In *Introduction to Digital Signal Processing*, pages 64–78. Academic Press, San Diego, 1989.

[98] V. F. Pisarenko. The Retrieval of Harmonics from a Covariance Function. *Geophysical Journal International*, 33(3):347–366, 1973.

[99] P. L. Dragotti, M. Vetterli, and T. Blu. Sampling moments and reconstructing signals of finite rate of innovation: Shannon meets strang–fix. *IEEE Transactions on Signal Processing*, 55(5):1741–1757, 2007.

[100] R. I. Stantchev, K. Li, and E. Pickwell-MacPherson. Rapid imaging of pulsed terahertz radiation with spatial light modulators and neural networks. *ACS Photonics*, 8(11):3150–3155, 2021.

[101] A. Gholami and M. D. Sacchi. A fast and automatic sparse deconvolution in the presence of outliers. *IEEE Transactions on Geoscience and Remote Sensing*, 50(10):4105–4116, 2012.

[102] W. Zhao, S. Zhao, L. Li, X. Huang, S. Xing, Y. Zhang, G. Qiu, Z. Han, Y. Shang, D.-E. Sun, C. Shan, W. Runlong, L. Gu, S. Zhang, R. Chen, J. Xiao, M. Yanquan, J. Wang, W. Ji, and L. Chen. Sparse deconvolution improves the resolution of live-cell super-resolution fluorescence microscopy. *Nature Biotechnology*, 40(4):606–617, 2022.

[103] J. Dong, X. Wu, A. Locquet, and D. S. Citrin. Terahertz superresolution stratigraphic characterization of multilayered structures using sparse deconvolution. *IEEE Transactions on Terahertz Science and Technology*, 7(3):260–267, 2017.

[104] J. Dong, P. Pomarède, L. Chehami, A. Locquet, F. Meraghni, N. F. Declercq, and D. S. Citrin. Visualization of subsurface damage in woven carbon fiber-reinforced composites using polarization-sensitive terahertz imaging. *NDT and E International*, 99:72–79, 2018.

[105] H.-B. Liu, H. Zhong, N. Karpowicz, Y. Chen, and X.-C. Zhang. Terahertz spectroscopy and imaging for defense and security applications. *Proceedings of the IEEE*, 95(8):1514–1527, 2007.

[106] K. S. Ryatt, M. Mobayrn, J. M. Stevenson, H. I. Maibach, and R. H. Guy. Methodology to measure the transient effect of occlusion on skin penetration

and stratum corneum hydration in vivo. *British Journal of Dermatology*, 119(3):307–312, 1988.

[107] P. Arora and B. Mukherjee. Design, development, physicochemical, in vitro and in vivo evaluation of transdermal patches containing diclofenac diethyl ammonium salt. *Journal of pharmaceutical sciences*, 91(9):2076–89, 2002.

[108] W. Poewe, O. Rascol, N. Quinn, E. Tolosa, W. Oertel, E. Martignoni, M. Rupp, and B. Boroojerdi. Efficacy of pramipexole and transdermal rotigotine in advanced parkinson's disease: A double-blind, double-dummy, randomised controlled trial. *Lancet neurology*, 6(6):513–20, 2007.

[109] O. A. A. Hanbali, H. M. S. Khan, M. Sarfraz, M. Arafat, S. Ijaz, and A. Hameed. Transdermal patches: Design and current approaches to painless drug delivery. *Acta Pharmaceutica*, 69(2):197–215, 2019.

[110] J. F. G. M. Hurkmans, H. E. Bodde, L. M. J. Van Driel, H. Van Doorne, and H. E. Junginger. Skin irritation caused by transdermal drug delivery systems during long-term (5 days) application. *British Journal of Dermatology*, 112(4):461–467, 1985.

[111] E. L. Tombs, V. Nikolaou, G. Nurumbetov, and D. M. Haddleton. Transdermal delivery of ibuprofen utilizing a novel solvent free pressure sensitive adhesive (psa) : Tepi technology. *Journal of Pharmaceutical Innovation*, 13(1):48–57, 2018.

[112] T. Blu, P.-L. Dragotti, M. Vetterli, P. Marziliano, and L. Coulot. Sparse sampling of signal innovations. *IEEE Signal Processing Magazine*, 25(2):31–40, 2008.

[113] B. K. Natarajan. Sparse approximate solutions to linear systems. *SIAM Journal on Computing*, 24(2):227–234, 1995.

[114] T. Blumensath and M. Davies. Iterative thresholding for sparse approximations. *Journal of Fourier Analysis and Applications*, 14:629–654, 2008.

[115] V. Carrer, C. Alonso, M. Pont, M. Zanuy, M. Córdoba, S. Espinosa, C. Barba, M. A. Oliver, M. Martí, and L. Coderch. Effect of propylene glycol on the skin penetration of drugs. *Archives of dermatological research*, 312(5):337—352, 2020.

[116] A. Terezaki, S. Kikionis, E. Ioannou, I. Sfiniadakis, L.-A. Tziveleka, A. Vitsos, V. Roussis, and M. Rallis. Ulvan/gelatin-based nanofibrous patches as a promising treatment for burn wounds. *Journal of Drug Delivery Science and Technology*, 74:103535, 2022.

[117] J. P. E. Junker, R. A. Kamel, E. J. Caterson, and E. Eriksson. Clinical impact upon wound healing and inflammation in moist, wet, and dry environments. *Advances in Wound Care*, 2(7):348–356, 2013.

[118] K. Nuutila and E. Eriksson. Moist wound healing with commonly available dressings. *Advances in Wound Care*, 10(12):685–698, 2021.

[119] N. Saewan and A. Jimtaisong. Natural products as photoprotection. *Journal of Cosmetic Dermatology*, 14(1):47–63, 2015.

[120] E. P. Balskus and C. T. Walsh. The genetic and molecular basis for sunscreen biosynthesis in cyanobacteria. *Science*, 329(5999):1653–1656, 2010.

[121] V. Geraldes and E. Pinto. Mycosporine-like amino acids (maas): Biology, chemistry and identification features. *Pharmaceuticals*, 14(1):63, 2021.

[122] C. A. Johnston. Promotion of sun-protective behaviors. *American Journal of Lifestyle Medicine*, 7(3):186–188, 2013.

[123] G. H. A. Teixeira and S. F. O'Keefe. Short communication: Mycosporine-like amino acids protect natamycin against photodegradation in milk ex-

posed to fluorescent or light-emitting diode light. *Journal of Dairy Science*, 102(6):4972–4977, 2019.

[124] Y. Nishida, Y. Kumagai, S. Michiba, H. Yasui, and H. Kishimura. Efficient extraction and antioxidant capacity of mycosporine-like amino acids from red alga dulse palmaria palmata in japan. *Marine Drugs*, 18(10):502, 2020.